STATE OF CALIFORNIA • DEPARTMENT OF TRANSPORTATION

TECHNICAL REPORT DOCUMENTATION PAGE

TR0003 (REV 10/98)

ADA Notice

For individuals with sensory disabilities, this document is available in alternate formats. For information call (916) 654-6410 or TDD (916) 654-3880 or write Records and Forms Management, 1120 N Street, MS-89, Sacramento, CA 95814.

1. REPORT NUMBER	2. GOVERNMENT ASSOCIATION NUMBER	3. RECIPIENT'S CATALOG NUMBER

4. TITLE AND SUBTITLE

Simulation of Liquefaction-induced Damage of the Port pf Long Beach Using the UBC3D-PLM Model

5. REPORT DATE

12/31/2017

6. PERFORMING ORGANIZATION CODE

7. AUTHOR

Luis G. Arboleda-Monsalve; Hung Nguyen

8. PERFORMING ORGANIZATION REPORT NO.

Project 15-02 / 65A0533 Task Order 012

9. PERFORMING ORGANIZATION NAME AND ADDRESS

University of Southern California
METRANS Transportation Center
Sol Price School of Public Policy
Ralph and Goldy Lewis Hall RGL 216
Los Angeles, CA 90089-0626

10. WORK UNIT NUMBER

11. CONTRACT OR GRANT NUMBER

65A0533

12. SPONSORING AGENCY AND ADDRESS

CA Department of Transporation
CALTRANS Division of Research, Innovation, and System Information
P.O. Box 942873
Sacramento, CA 942873

13. TYPE OF REPORT AND PERIOD COVERED

Final Report
08/15/2015 to 08/14/2016

14. SPONSORING AGENCY CODE

15. SUPPLEMENTARY NOTES

16. ABSTRACT

In the past decades, expansion projects of port facilities in California, USA, have been completed by placing hydraulic fills. These loose man-made fills and even their subjacent natural estuarine and marine deposits, have shown to be susceptible to liquefaction. The case of study presented in this research, the Port of Long Beach (POLB), Pier S, which is located within a few miles of the Newport-Inglewood and the Palos Verdes faults, offers a unique opportunity to use advanced constitutive soil models to study liquefaction. This research is presented to develop the following specific objectives: i) to calibrate constitutive model parameters to reproduce laboratory tests following different stress paths and shear strain levels; ii) to assess the use of an advanced constitutive soil model (UBC3D-PLM) to predict the soil behavior at the POLB, Pier S when a seismic event induces liquefaction; iii) to provide recommendations related to the permanent deformations of soils which could compromise the resiliency of the port. A semi-empirical evaluation of the liquefaction triggering and settlements were developed. Then, numerical analyses using the UBC3D-PLM soil model were used to determine the onset of liquefaction and estimate ground-induced settlements based on post-liquefaction excess pore pressure dissipation. This work presents the results of boundary value element simulations of cyclic undrained direct simple shear and monotonic triaxial compression. Numerical simulations are performed to study the free-field response and behavior of hypothetical structures when an Operating and Contingency Level Earthquakes occur. The assessment of liquefaction susceptibility based on semi-empirical methods showed that Unit B is the only liquefiable layer under both earthquake levels. Generally, large discrepancies were observed in the calculation of liquefaction-induced ground settlements using classical semi-empirical approaches.

17. KEY WORDS	18. DISTRIBUTION STATEMENT
Liquefaction, Constitutive Model, Settlement, Numerical Analyses.	This document is available to the public through CALTRANS and METRANS website: https://www.metrans.org/research/simulation-liquefaction-induced-damage-port-long-beach-using-ubc3d-plm-model

19. SECURITY CLASSIFICATION *(of this report)*	20. NUMBER OF PAGES	21. COST OF REPORT CHARGED
Unclassified	139	$30,003.86

SIMULATION OF LIQUEFACTION-INDUCED DAMAGE OF THE PORT OF LONG BEACH USING THE UBC3D-PLM MODEL

Final Report

METRANS PROJECT 15-02

December 2016

Principal Investigator
Luis G. Arboleda-Monsalve
Assistant Professor

Co-Principal Investigator
Hung Nguyen
Professor

Research Assistants
Jaime Andres Mercado
Andrew Sover
Andres F. Uribe
Deisy Preciado
Nestor Avila

Department of Civil and Construction Engineering Management
California State University, Long Beach
Long Beach, CA 90840

Disclaimer

The contents of this report reflect the views of the authors, who are responsible for the accuracy of the data and information presented herein. This document is disseminated under the sponsorship of the Department of Transportation, University Transportation Centers Program, the California Department of Transportation and the METRANS Transportation Center in the interest of information exchange. The U.S. Government, the California Department of Transportation, and California State University, Long Beach assume no liability for the contents or use thereof. The contents do not necessarily reflect the official views or policies of the State of California, CSULB, or the Department of Transportation. This report does not constitute a standard, specification, or regulation.

Abstract

In the past decades, expansion projects of port facilities in California, USA, have been completed by placing hydraulic fills. These loose man-made fills and even their subjacent natural estuarine and marine deposits, have shown to be susceptible to liquefaction. The case of study presented in this research, the Port of Long Beach (POLB), Pier S, which is located within a few miles of the Newport-Inglewood and the Palos Verdes faults, offers a unique opportunity to use advanced constitutive soil models to study liquefaction. This research is presented to develop the following specific objectives: i) to calibrate constitutive model parameters to reproduce laboratory tests following different stress paths and shear strain levels; ii) to assess the use of an advanced constitutive soil model (UBC3D-PLM) to predict the soil behavior at the POLB, Pier S when a seismic event induces liquefaction; iii) to provide recommendations related to the permanent deformations of soils which could compromise the resiliency of the port. A semi-empirical evaluation of the liquefaction triggering and settlements were developed. Then, numerical analyses using the UBC3D-PLM soil model were used to determine the onset of liquefaction and estimate ground-induced settlements based on post-liquefaction excess pore pressure dissipation. This work presents the results of boundary value element simulations of cyclic undrained direct simple shear and monotonic triaxial compression. Numerical simulations are performed to study the free-field response and behavior of hypothetical structures when an Operating and Contingency Level Earthquakes occur. The assessment of liquefaction susceptibility based on semi-empirical methods showed that Unit B is the only liquefiable layer under both earthquake levels. Generally, large discrepancies were observed in the calculation of liquefaction-induced ground settlements using classical semi-empirical approaches.

The numerical simulations showed that Unit B for all earthquake motions developed pore water pressure ratios larger than 85%, which caused significant reductions of the vertical effective stresses, hence, liquefaction occurred. Simulations of hypothetical structures showed that settlement of structures with shallow foundations on liquefiable soils were controlled by a combination of different failures mechanisms. However, it was observed that the model is capable to predict the onset of liquefaction and estimate liquefaction-induced settlements.

Keywords: Liquefaction, Constitutive Model, Settlement, Numerical Analyses.

Table of Contents

Page

List of figures

Page

List of tables

Page

Disclosure

Dr. Luis G. Arboleda (Principal Investigator), Dr. Hung Nguyen (Co-principal investigator) and student assistants Jaime Andres Mercado, Andrew Sover, Andres F. Uribe, Deisy Preciado, and Nestor Avila participated in this research titled: “SIMULATION OF LIQUEFACTION-INDUCED DAMAGE OF THE PORT OF LONG BEACH USING THE UBC3D-PLM MODEL.” This research was funded by a grant from the California Department of Transportation in the amount of $35,000. The research was conducted as part of the METRANS Tier 1 University Transportation Center.

Acknowledgments

Financial support was provided by METRANS and the California Dept. of Transportation (CALTRANS), Project No. 15-02. The information provided by Mr. Cheng Lai from the POLB is greatly appreciated.

1. INTRODUCTION

Earthquakes cause damage to civil infrastructure and negatively impact communities in the form of economic losses or fatalities. Earthquakes can generate landslides, floods, tsunamis or structural damages which at times are attributed to soil liquefaction. In the last decade, earthquakes around the world killed almost 100,000 people, affected 14 million people and produced losses estimated at more than $215 billion (Gu 2008). Over the past 50 years, significant research effort has been made to understand the nature, causes and consequences of earthquakes and their potential to damage infrastructure. Numerous studies have resulted in the improvement of the predicting capabilities of soil models to assess the seismic vulnerability of urban infrastructure.

Loose sands subjected to cyclic loading during an earthquake transfer the induced stresses from the soil skeleton to the pore water generating excess pore water pressure. If the soil deposit is saturated and subjected to rapid loading, this accumulation of water pressure is unable to dissipate and results in a reduction of the effective stresses and an associated loss of shear strength and stiffness. This phenomenon, known as “liquefaction”, increases the deformations of the soil deposit and might cause devastating effects in the existing infrastructure (Boulanger and Idriss 2012; Kramer 1996). Depending on the structure type, foundation, and characteristics of the earthquake magnitude, these effects can result in the collapse or partial collapse of a structure. Structural damages occur during and after an earthquake because the supporting soil softens or fails due to loss of shear strength induced by the large values of excess pore water pressure generated during the earthquake. One manifestation of the liquefaction phenomenon that serves as an indication that liquefaction was induced, is the presence of “sand boils”. These are produced by the groundwater flowing towards the surface carrying sand particles. **Fig. 1** shows sand boils caused in a free-field condition during the 1989 Loma Prieta Earthquake in Oakland, California, and the 1979 Imperial Valley Earthquake in Imperial County, California.

Fig. 1. Sand boils generated after the earthquake: a) 1989 Loma Prieta earthquake, and b) 1979 Imperial Valley earthquake (after NISEE 2016).

Structural damages as a product of liquefaction have been documented in numerous case histories including settlement of buildings and bridges, foundation failures, lateral spreading of foundations, damage and flotation of buried utilities, and failure of retaining walls. Since 1964, when the Good Friday earthquake with a magnitude of 9.2 occurred in Alaska and the Niigata earthquake with magnitude 7.5 occurred in Japan, cases of liquefaction-induced damages have been recorded in greater detail from various earthquakes such as the 1999 Kocaeli (Turkey) earthquake, where soil liquefied and caused bearing capacity failures. The loss of bearing capacity can cause building foundations to rotate or punch throughout the soil. **Fig. 2** shows the damage that the earthquakes caused at those sites, including overturning failures of buildings in Niigata and bearing capacity failures in Kocaeli.

Fig. 2. a) Overturning failures in residential complex in 1964 Niigata earthquake, and b) Liquefaction-induced settlement due to loss of bearing capacity in 1999 Kocaeli earthquake (after NISEE 2016).

One of the most destructive effects of liquefaction is the lateral spreading on foundations. This potential failure mechanism is characterized by the incremental displacements during the earthquake motion causing lateral movement of the liquefied soil. This type of liquefaction induces large settlements and permanent displacements of structures, especially near large bodies of water and tend to affect bridges in waterways, dams, buildings in coastal regions, railroad tracks, ports, unreinforced pavements, and poorly reinforced building foundations. **Fig. 3** shows some of those cases where liquefaction caused large displacements. **Fig. 3**a, shows the lateral spreading of the bridge foundations that caused the bridge falls off their supports during the 1964 Niigata earthquake and **Fig. 3**b shows the flow liquefaction-induced structural damage in waterfront buildings during the 1999 Kocaeli earthquake.

Fig. 3. a) Lateral spreading causing bridge spans to fall off from the supports during the 1964 Niigata earthquake, and b) Lateral spreading of waterfront properties during the 1999 Kocaeli earthquake (after NISEE 2016).

Liquefaction can also cause severe damage of buried structures, such as large settlements and distortions that causes large displacements with respect to their original location. This is also another type of bearing capacity failure induced by liquefaction in which buried structures are found near the surface because of the large upward seepage forces induced by the earthquake. This is particularly critical in urban environments if the failure occurs in buried gas lines, sewers, water pipes, and utilities. **Fig. 4** shows the failure of a sewage line that has floated up to the surface due to buoyant forces generated during the 2004 Chuetsu earthquake. These types of failures can cause fires due to breakage of gas pipes.

Fig. 4. Flotation of sewage line during the 2004 Chuetsu earthquake (after NISEE 2016).

Flow liquefaction in large masses of earth can occur if a liquefiable layer of soil is present in slopped ground such as dams. Retaining systems and earth dams are affected by the liquefaction phenomenon and major damage can occur. Flow failures have caused the collapse of earth dams and other slopes where liquefaction is driven by the static gravitational forces and can produce very large displacements. An example of a retaining system that collapsed was the San Fernando dam in 1971 as shown in **Fig. 5**, which resulted in the failure of the upper and lower San Fernando dam.

Fig. 5. Lower San Fernando Dam collapse due to San Fernando earthquake in 1971 (after NISEE 2016).

After the 1964 Niigata and 1971 San Fernando earthquakes, research on the behavior of the abovementioned structures when subjected to earthquake loadings is becoming essential to gain deep understanding of the liquefaction mechanisms that may cause damage to the existing infrastructure. Idriss and Boulanger (2004) discussed that the assessment of liquefaction susceptibility of soils needs to be evaluated from several redundant procedures and the success depends on the quality of the field data, laboratory tests, and index tests for soil characterization.

The decisions that can be made regarding ground improvement must not rely only on one method [e.g., only on Cone Penetration Tests (CPT) or Standard Penetration Test (SPT)] but in a variety of *in situ* testing methods. In this matter, only a few available design codes provide clearly defined standards on the earthquake resistance of soils. Just to cite one of them, the Eurocode 8 in Part 5, presents provisions on the design of foundations and retaining structures and presents specifications for soils susceptible to liquefaction. An evaluation of the liquefaction potential needs to be performed if the soils are located below the water table and support foundations with extended layers or thick lenses of loose sands with or without significant amount of silt or clay particles. The evaluation must include a minimum number of either *in situ* SPTs or CPTs accompanied with sieve analyses performed in the laboratory. In this research, and following that recommendation, the liquefaction susceptibility is evaluated with semi-empirical methods including both SPT and CPT, and the onset of liquefaction is evaluated with boundary value simulations and free-field numerical simulations.

The first step in the dynamic analysis of a structure is to perform a ground response analysis of the soil deposit taking into account its geological and geotechnical characteristics. The soil has a "filtering" effect in the seismic waves such that accelerations at the base of the rock can be amplified or reduced as the waves move upward through the different soil layers. When the frequency of the earthquake at the ground surface or near the foundation of overlying structures is similar to the natural frequencies of the overlying structures, they will oscillate with large amplitudes causing distortions, cracking and at times collapse of civil infrastructure. Herein, a site response analysis for the specific case of the Port of Long Beach (POLB) Pier S, located in the greater Los Angeles area is developed following these steps: i) determination of the geotechnical and groundwater characteristics of the soil deposit describing the static and cyclic behavior of soils using boundary value simulations; ii) determination of the seismic input motions based on previously reported site specific and probabilistic studies; iii) determination of the type of numerical and constitutive model to be used in free-field response analyses of the POLB subsurface conditions subjected to Operating Level (OLE) and Contingency Level (CLE) earthquakes; and iv) evaluation of free-field settlements due to post-earthquake excess pore water pressure dissipation and behavior of simplified hypothetical structures with similar frequencies of the dominant earthquake frequencies to analyze the detrimental consequences when liquefaction is induced. These steps are followed to conclude about the POLB resiliency to a seismic event. This study, which is intended to describe the liquefaction potential of the proposed subsurface conditions,

actively encourages the need of liquefaction mitigation efforts as the ones recently performed at the POLB, Pier S.

In this study the local soil stratigraphy, material properties, and groundwater table location were provided by the POLB authorities prior to the beginning of this study for the particular location of Pier S. The characteristics of the input motion regarding duration, peak accelerations, frequency content, magnitude, and distance to the source have been extensively studied at the location selected for this site-specific analysis. The subsurface conditions of the site studied herein were typical for a one-dimensional (1D) analysis because in general the bedrock, groundwater conditions, and soil layers can be generalized to be horizontal without introducing significant errors. Under 1D analyses, it is assumed that the seismic waves coincide with shear waves and propagate vertically from the bedrock [i.e., seismic waves are bent by successive refractions into a nearly vertical path according to Snell's law of refraction, (Plaxis 2015)].

The main goal of the proposed numerical analyses is to evaluate the liquefaction potential of this POLB site. For this evaluation, the particle size and shape, gradation and plasticity as well as the earthquake magnitude, duration and peak acceleration play an important role. Two different technics are used to determine the susceptibility to liquefaction of the proposed site. First, semi-empirical approaches are considered by calculating factors of safety against liquefaction computed as the ratio of cyclic shear stresses to cause liquefaction (i.e., Cyclic Resistant Ratio) and equivalent cyclic shear stresses induced by the earthquake input motion (i.e., Cyclic Stress Ratio). Then, numerical models are employed based on the dynamic propagation of waves through the continuum soil profile quantifying liquefaction in terms of pore water pressure ratios (r_u) as the earthquake occurs.

The case of study presented in this research, which is located within a few miles of the San Andreas Fault and is also near the Newport-Inglewood and the Palos Verdes faults, offers a unique opportunity to use advanced constitutive soil models to answer the following questions when evaluating the liquefaction potential of a site: i) are soils susceptible to liquefaction? ii) can liquefaction be induced by the earthquake motion under consideration? and iii) what are the potential consequences? (Kramer 1996).

This research is presented to develop the following specific objectives: i) to calibrate constitutive model parameters after a compilation of published subsurface investigation reports of the POLB

and to determine the suitability of these parameters to reproduce laboratory tests following different stress paths and shear strain levels; ii) to assess the use of advanced constitutive models like the UBC3D-PLM to predict the behavior of the POLB Pier S when a seismic event induces liquefaction; iii) to provide recommendations related to the resulting permanent deformations and residual strength of soils which could compromise the resiliency of the port. To achieve these goals, a typical cross section along Pier S is proposed in the analyses. The input earthquake motion will be determined from historical records of earthquakes in the vicinity of the project. The selection of the critical earthquake motion is not straightforward and therefore multiple earthquakes will be evaluated. This work presents an opportunity for advancing the understanding of the likelihood of liquefaction-induced damage on the POLB Pier S and contributes to understanding the role of engineering on the resiliency of projects of similar nature in urban environments.

To accomplish the proposed goals, this report is organized as follows. Chapter 2 presents a technical background on soil liquefaction and a review of the state-of-the-practice of the different triggering semi-empirical approaches used in liquefaction studies. This chapter also presents a review of the classical methods developed for the calculation of free-field liquefaction-induced settlements that are used in current geotechnical engineering practice. The limitations of those methods to assess liquefaction induced-settlements are outlined. In this chapter, a description of the constitutive model used in this research, the UBC3D-PLM model, is presented. Several case histories are described showing its successful application for the evaluation of liquefaction potential of different sites.

Chapter 3 presents the main characteristics of the site object of this research, the POLB Pier S. The subsurface conditions are presented based on the information obtained from SPTs, CPTs, and measurements of shear wave velocities. A summary of the geological conditions and the predominant faults present at the POLB area is presented as an indication of the seismicity of the southern California area where the POLB is located. Chapter 4 presents the semi-empirical evaluation of liquefaction at the POLB Pier S site using the field tests available in this project. Settlement calculations induced by liquefaction using other classical approaches are developed for the free-field conditions.

Chapter 5 presents the numerical liquefaction evaluation of POLB Pier S with two-dimensional analyses performed with the finite element program, PLAXIS 2D. First, a description of the simulation process and stages in PLAXIS 2D is presented. Then, the constitutive soil parameters

are defined and calibrated by simulating undrained direct simple shear tests under cycling loading to reproduce the cyclic strength curve of the liquefiable soil deposit. The results of monotonic drained triaxial compression tests are also presented to evaluate the model capabilities under static loading. The input seismic motions and the calibration of damping coefficients are presented in order to perform the numerical analyses. These analyses are performed for the case of free-field conditions and parametric studies are presented to evaluate the response of hypothetical structures present at the site. The main objective of these analyses is to assess the liquefaction-induced settlement and potential damage that may compromise the safety and ability of the port to recover after an earthquake (resiliency). Chapter 6 presents the conclusion and recommendations of this research.

2. TECHNICAL BACKGROUND ON SOIL LIQUEFACTION

Liquefaction-induced tilting and settlement of infrastructure, mostly on shallow foundations has been extensively documented in the 1964 Niigata (Japan), 1964 Alaska (USA), 1990 Dagupan city (Philippines), 1999 Chi-Chi (Taiwan), and 1999 Kocaeli (Turkey) earthquakes (Lu et al. 2011). More recently, liquefaction has been observed in the 2010 and 2011 Christchurch earthquakes (New Zealand) (Bray et. al. 2013). Numerical modeling can play an important role for the development of cost-effective solutions to mitigate possible disruption of function of the existent infrastructure.

Liquefaction is a phenomenon that could lead to detrimental consequences to the infrastructure depending upon the subsurface conditions, the magnitude of the earthquake motion, loading characteristics and type, size and importance of the structures present on the site. Idriss and Boulanger (2008) studied the consequences of liquefaction in soils, those include but are not limited to: i) the loss of shear strength of soils that could lead to slope stability failures, ii) lateral spreading phenomenon in relatively flat ground or gentle slopes, and iii) settlement due to reconsolidation of liquefied soils after the excess pore water pressures generated by the earthquake are dissipated. These three detrimental consequences are linked to the two main manifestations of liquefaction: flow liquefaction and cyclic mobility.

The current analytical and numerical tools are not able to accurately account for these factors on the determination of the deformations and ground settlements induced by liquefaction. Numerous assumptions need to be made in the analysis and only preliminary estimates can be computed especially for the calculation of residual strengths. In spite of the numerous efforts made in the past in this field, there is not an accurate method or model accepted as a general framework for the determination of liquefaction-induced deformations.

Liquefaction is typically divided into two main type of associated phenomena and effects: flow liquefaction and cyclic mobility. Flow liquefaction is mostly concerned about the stability of sloping ground which can experience very large displacements as a consequence of a seismic event. In this type of liquefaction, the static shear is the main driving factor and with the increase in the shear stresses generated from the seismic motion comes a reduction in the soil shear strength. On the other hand, the ground deformations arising from cyclic mobility occur due to a combination of static and cyclic loading. An example of the manifestation of cyclic mobility is lateral spreading which generally occurs in gently sloping ground. The deformation from cyclic mobility tend to be smaller than those generated by flow liquefaction, nonetheless, it might affect and damage the present infrastructure and can affect large areas. When the ground is completely flat, the type of liquefaction occurs under very small or zero static shear stress present in the soil mass. The majority of the ground movements for this case tend to occur during the earthquake but the permanent deformations of the ground are small and mostly occur due to settlements associated with the dissipation of excess pore water pressures after the earthquake stops (Kramer 1996). These excess pore water pressures, especially in the cyclic mobility case, are in the order of magnitude of the initial vertical effective stress (i.e., pore pressure ratio close to one) which causes liquefaction of the soil mass. Been and Jefferies (2016) discussed that even though cyclic mobility and flow liquefaction differ conceptually mainly in the failure mechanism, the generation of excess pore water pressure, soil softening, and loss of strength are similar and therefore the existing constitutive soil models hardly differ in their formulation to model one phenomenon or the other.

To explain the liquefaction potential of soils, the geologic history and depositional environment play a very important role. The geologic features related to the age of soil deposits and hydraulic characteristics of the site need to be carefully evaluated to determine the liquefaction potential of soils. The depositional environmental has been important in the past because low *in situ* void ratios and associated relative densities, typically found in loose deposits, have been an indicator that the soils were deposited from man-made fills, alluvial, fluvial, marine, deltaic or wind-blown environments and have shown to be prone to liquefaction. Conversely, older deposits from the geologic point of view have shown reduced liquefaction potential. In the site object of study in this research, there is a large presence of hydraulic fills and marine deposits. The compaction effort plays an important role in the liquefaction potential. Well-compacted fills are less prone to liquefaction than loosely compacted fills which are typical of hydraulic fills which are formed mostly by deposition of soil particles that settled into the water with large void ratios.

The likelihood of liquefaction of a dense soil is less than that of a loose soil. The critical state theory plays an important role to describe this behavior. The void ratio, the confining conditions, and their associated contractive or dilative behavior have a strong influence on the occurrence of liquefaction. Dense sands are less prone to liquefaction because their *in situ* void ratio (e) is located below the critical state void ratio (e_{cs}) and negative excess pore water pressures are generated as the soil dilates during shearing which tends to increase the effective stress, inhibiting the onset of liquefaction. On the other hand, loose soils tend to have contractive behavior during shearing that allows the generation of positive excess pore water pressures and thus decreasing the effective stresses. As is shown in **Fig. 6**, Casagrande (1936) found that the boundary between loose and dense states of the soil is through the Critical Void Ratio (*CVR*) line that sets the limit between soils that are susceptible to liquefaction depending upon the effective confining pressures.

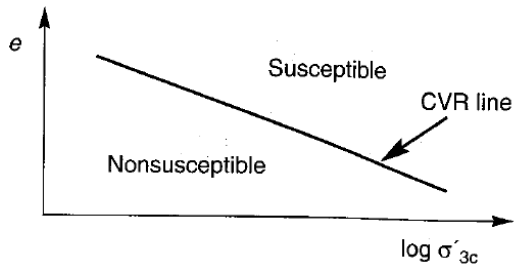

Fig. 6. *CVR* as a boundary of contractive and dilative states to assess liquefaction susceptibility (Kramer 1996).

In addition to the site geology reflected in its stress history, the particle size and gradation characteristics are key on the dynamic behavior of most soils. Well graded soils present lower changes in volume during loading and tend to be less prone than poorly graded ones. The particle shape also matters in the problem because rounded particle grains tend to easily adopt a denser configuration than soils with angular or subangular particles. This tendency makes soils with rounded particles more prone to liquefaction. If the soils are fine grained, the Chinese criteria (Wang 1979) establishes that the potential for liquefaction is a function of the particle size, liquid limit, water content, and liquidity index. According to such criterion, fine grained soils susceptible to liquefaction are those that have the following characteristics: i) fraction finer than 0.005 mm less than 15%; ii) liquid limit less than 35%; natural water content larger than 90% of the liquid limit; and liquidity index less than 0.75.

2.1 Semi-Empirical Approaches for Liquefaction Evaluation

There are different methods to evaluate the susceptibility to liquefaction in saturated sandy soils. Among those methods are the semi-empirical procedures for liquefaction potential proposed by Seed and Idriss (1971) and Idriss and Boulanger (2014). The evaluation consists on the calculation of the factor of safety against liquefaction as the ratio of the resistance of the soil to liquefaction triggering over the demand of cyclic shear stress induced by the earthquake. This factor of safety is calculated with the following expression:

$$FS = \frac{CRR}{CSR} MSF \tag{1}$$

where CRR and CSR represent the cyclic resistance and cyclic stress ratios and MSF represents a magnitude scaling factor for earthquake magnitudes different than 7.5. The magnitude of the factor of safety varies depending on the code and regulation of the site where the liquefaction potential is assessed. For example, the Eurocode 8 recommends a factor of safety against liquefaction larger than 1.25.

The CRR term in the numerator of Eq. (1), referred as the Cyclic Resistance Ratio, is generally determined based on *in situ* testing, being the Standard Penetration Test (SPT) and Cone Penetration Test (CPT) the most commonly used in current geotechnical engineering practice. The denominator in Eq. (1) depends on the characteristics of the seismic motion like the peak acceleration induced by the earthquake. The CSR of a soil deposit may be expressed as:

$$CSR = \frac{\tau_{cyc}}{\sigma'_{vo}} = 0.65 \frac{a_{max}}{g} \frac{\sigma_v}{\sigma'_{vo}} r_d \tag{2}$$

where τ_{cyc} is the average equivalent cyclic shear stress amplitude induced by the earthquake which is assumed to have an amplitude of 65% of the peak cyclic shear stress, a_{max} is the peak horizontal acceleration at the ground surface, g is the acceleration of gravity, σ_v is the total overburden pressure at depth under consideration, σ'_{vo} is the effective overburden pressure at depth under consideration, and r_d is a stress reduction factor that may be estimated with the following equations (After Seed and Idriss 1971):

$$
\begin{aligned}
r_d &= 1.0 - 0.00765z \;\; for\; z \le 9.15\; m \\
r_d &= 1.174 - 0.0267z \;\; for\; 9.15\; m \le z \le 23m \\
r_d &= 0.744 - 0.008z \;\; for\; 23\; m \le z \le 30m \\
r_d &= 0.5 \;\; for\; z > 30\; m
\end{aligned}
\tag{3}
$$

where z is the depth below the ground surface in meters. This coefficient can also be calculated from **Fig. 7** for different earthquake magnitudes.

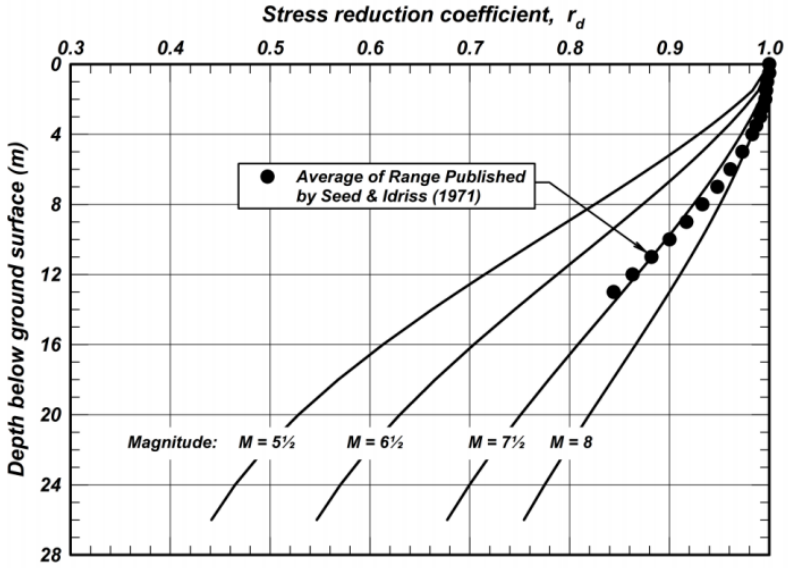

Fig. 7. Shear stress reduction factor relationship (Idriss and Boulanger 2010).

Youd et al. (Youd et al. 2001) summarized the preferred methods for estimating the peak horizontal acceleration, a_{max} for potentially liquefiable soils (in order of preference):

1) Empirical correlations of the a_{max} with earthquake magnitude, distance from the seismic energy source, and local site conditions for the case of sites on bedrock or stiff to moderately stiff soils. The authors recommend that the selection of attenuation relationships should be based on factors such as region of the country, type of faulting, and site condition.

2) For soft sites and other soil profiles that are not compatible with available attenuation relationships, the acceleration may be estimated from local site response analyses. Computer programs like SHAKE and DESRA among others, may be used for the calculations. A set of

plausible earthquake records should be used in the analysis, including as many as possible from earthquakes with similar magnitudes and source distances.

3) The least desirable method for estimating the peak ground acceleration is through amplification ratios such as those proposed by Idris (1990, 1991) and Seed et al. (1994).These methods suggest multiplying bedrock outcrop motions by factors to estimate surface motions. The authors warned that these methods should be used with caution because amplification ratios are influenced by strain level, earthquake magnitude, and frequency content.

Youd et al. (Youd et al. 2001) also discussed that because liquefaction usually develops at sites where ground motion amplification may occur and where sediments soften as excess pore water pressure develops, the recommended procedure to estimate a_{max} should be in the absence of pore water pressures or onset of liquefaction. In other words, including the site amplification effects but neglecting the influence of excess pore water pressure.

Seismologists calculate earthquake magnitudes using five different scales: 1) Local or Richter magnitude (M_L), 2) surface-wave magnitude (M_S), 3) short-period body-wave magnitude (m_b), 4) long-period body-wave magnitude (m_B), and 5) moment magnitude (M_w). The preferred and most commonly used magnitude for liquefaction studies is the moment magnitude which is the magnitude used in the present study.

The input parameters for the seismic demand (CRR) in the factor of safety against liquefaction have been traditionally presented for earthquakes magnitudes of 7.5. Therefore, for earthquake levels as the proposed in this study, a Magnitude Scaling Factor (MSF) needs to be introduced. Seed and Idriss (1982), proposed a MSF to estimate an equivalent number of cycles of shear stress developed during different magnitude earthquakes. The MSF is defined as a function of the moment magnitude, as follows:

$$MSF = \frac{10^{2.24}}{M^{2.56}} \tag{4}$$

The term MSF in Eq. (1) and (4) is used to scale the calculated CSR to the reference earthquake with a magnitude of 7.5. This factor must be applied to correct the CSR based upon the calculated

seismic hazard. This scaling factor was revised and recommended by Youd et al. (Youd et al. 2001) to be used in current geotechnical engineering practice.

Other factors were developed by Seed (1983) to study the influence of large overburden pressures and static shear stresses on the computation of the factor of safety against liquefaction. These correction factors typically denoted as $K\sigma$ and $K\alpha$, are mostly used in the liquefaction hazard analyses of large structures inducing high overburden pressures and for liquefaction studies involving sloping ground like in the case of embankments and dams, which have large initial static shear stress values. For liquefaction studies involving horizontal or gently sloping ground and without large overburden pressures, these factors are not necessary in the calculation of the liquefaction hazard.

2.1.1 Liquefaction Evaluation using Standard Penetration Tests (SPTs)

For the determination of liquefaction potential using the SPT method, a corrected blow count denoted as $(N_1)_{60}$ as explained by Kramer (1996), is used to calculate the resistance value from the SPT results as follows:

$$(N_1)_{60} = N_m C_N \frac{E_m}{0.60 E_{ff}} \tag{5}$$

where N_m is the measured penetration resistance, C_N is an overburden correction factor, E_m the actual free-fall hammer energy, and E_{ff} the theoretical free-fall hammer energy.

The overburden pressure correction factor may be calculated using the following expression proposed by Liao and Whitman (1986), where the vertical effective stresses need to be input in tons per square foot:

$$C_N = \sqrt{\frac{1}{\sigma'_{vo}}} \tag{6}$$

For the estimation of the $(N_1)_{60}$, it is assumed that E_m and E_{ff} are both equal to 0.6, which is the approximated historical SPT energy for North American practice (Naeim 2001). Correction factors

have also been proposed by various authors to account for different rod lengths, sampling methods, and borehole diameters when performing the SPTs.

Seed et al. (1985) studied the CRR for clean and silty sands for an earthquake magnitude of 7.5 necessary to determine the minimum cyclic stress ratio at which liquefaction may be caused using the corrected penetration resistance $(N_1)_{60}$ as the indicator. Based in this methodology, liquefaction is expected to occur when the CSR exceeds the CRR normalized for an earthquake magnitude of 7.5. The CRR for clean sands (i.e., sands with less than 5% content of fines) may also be estimated using a relationship proposed by Seed et al. (1985), as follows:

$$CRR_{7.5} = \frac{a + cx + ex^2 + gx^3}{1 + bx + dx^2 + fx^3 + hx^4} \tag{7}$$

where the coefficients *a* through *h* are shown in a flowchart (see **Fig. 9**) presented by Chang et al. (2011). The variable *x* represents the equivalent clean sand penetration resistance. For those cases in which the content of fines differs from 5%, Seed and Idriss (1971) developed an expression to correct the standard penetration resistance $(N_1)_{60}$ for silty sands and calculate an equivalent clean sand penetration resistance, $(N_1)_{60,FC}$, as follows:

$$(N_1)_{60,FC} = \alpha + \beta(N_1)_{60} \tag{8}$$

where α and β are a function of Fine Content (FC) which represents the content of fines of the soil obtained from a grain size distribution.

Fig. 8 shows the curve originally proposed by Seed et al. (1985) for the results of the cyclic resistance ratio versus the corrected clean sand SPT value (i.e., $(N_1)_{60}$). The figure is a compilation of several case histories showing the critical combinations of strength values measured with SPT tests and cyclic stress ratios necessary to induce liquefaction.

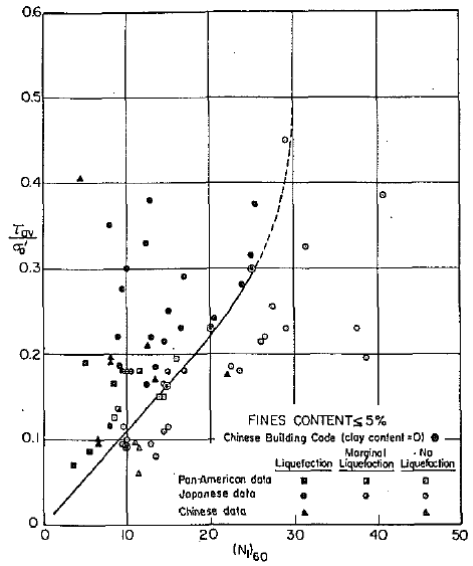

Fig. 8. Relationship between CSR and $(N_1)_{60}$ for clean sands for an earthquake magnitude of 7.5 (Seed et al. 1985).

Fig. 9 presents a flow chart for the evaluation of soil liquefaction with the method suggested by Seed and Idriss (1971). The different steps necessary to calculate the factor of safety against liquefaction are summarized as follows: i) calculation of the CSR as indicated on the left hand side of the chart, ii) computation of the corrected values $(N_1)_{60}$ from the measured SPT blow counts *N*, iii) computation of clean-sand equivalent value of $(N_1)_{60,FC}$ based on the fine content of the soil, iv) estimation of $CRR_{7.5}$ for the soil using the proposed expression, v) adjustment of the earthquake magnitude using the MSF, and vi) calculation of the factor of safety against liquefaction.

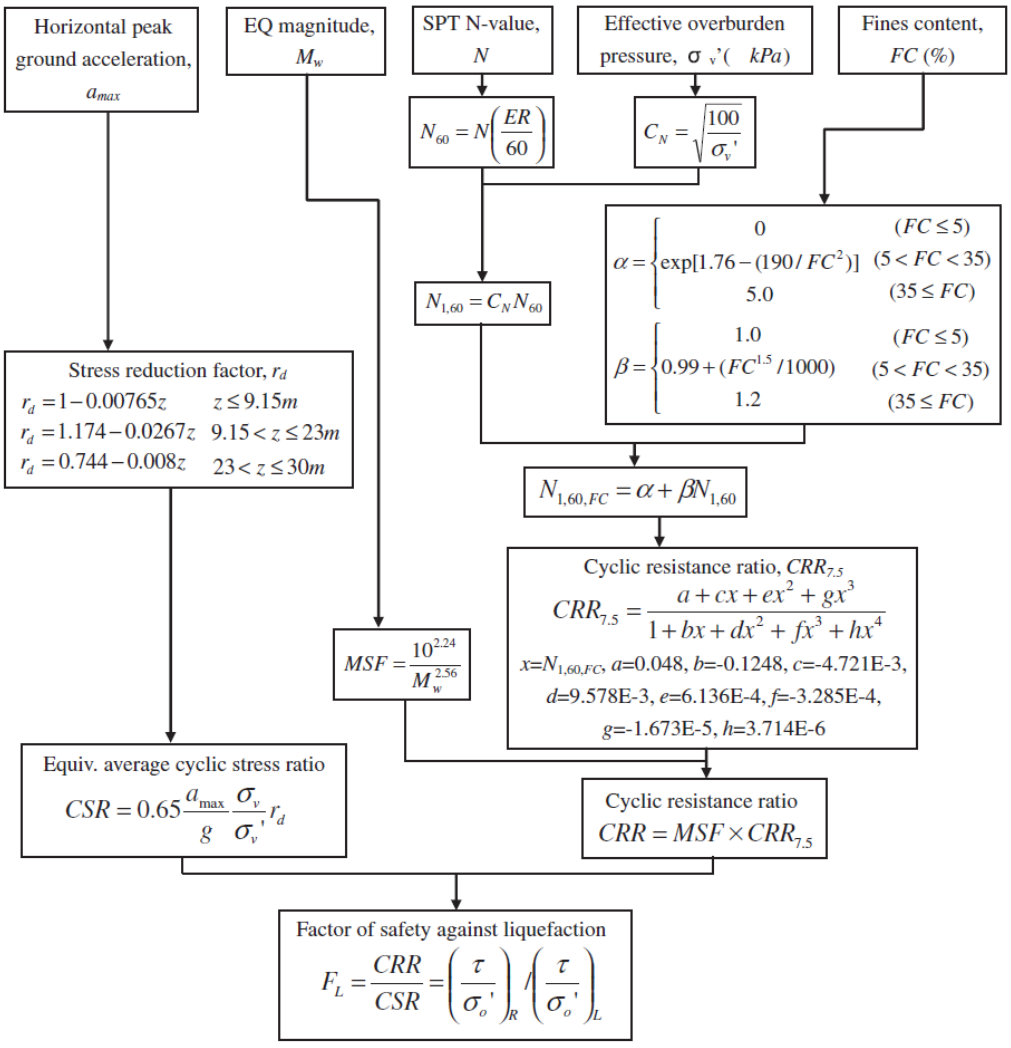

Fig. 9. Summary flowchart of Seed and Idriss (1971) SPT-based method with modifications in the workshops by NCEER and NSF (Youd et al. 2001). (Chang et al. 2011).

2.1.2 Liquefaction Evaluation using Cone Penetration Tests (CPTs)

The main advantage of the CPT is the continuous measurement of penetration resistance and friction in the soil. This is reflected in a detailed definition of the soil layers, which may be used to determine the liquefaction potential of soils along the soil profile. This significantly improves the analysis of liquefaction susceptibility compared with other methods based on SPT results.

Fig. 10 provides curves developed by Robertson and Wride (1998) to determine the cyclic resistance ratio for sands from the results of CPTs and normalized for an earthquake magnitude of

7.5. The figure is presented for sands with FC≤5% and median grain size (D_{50}) of 0.25 and 2.0 mm. The results were developed from CPT data of several case histories. The figure shows with closed symbols, those sites where liquefaction was reached. Conversely, the open symbols represent sites where liquefaction was not reached. The limiting curves are shown as boundaries where the majority of closed symbols are located above the curve. The two green dashed lines show the boundary curves for sands with fines contents of 15 % and 35 %, respectively.

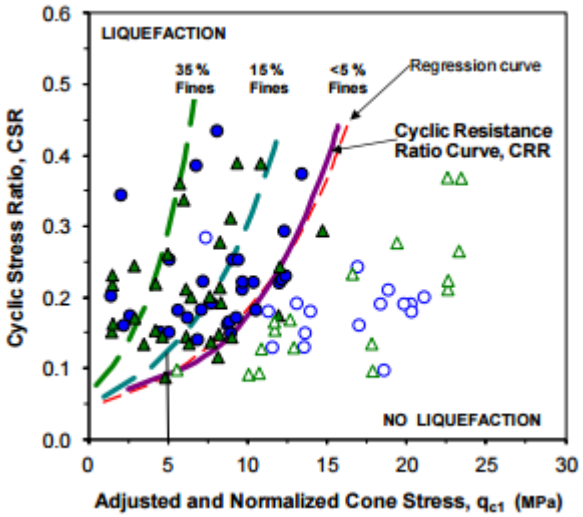

Fig. 10. Curve for the determination of CRR from overburden stress-corrected CPT tip resistance, q_{c1N} (after Robertson and Wride 1998).

To use the curve for soils with fine contents larger than 5%, the following correction of the penetration resistance, q_{c1N}, was developed by Roberson and Wride (1998):

$$(q_{c1N})_{cs} = K_c q_{c1N} \tag{9}$$

where $(q_{c1N})_{cs}$ is the equivalent clean sand value of q_{c1N} which represents the corrected CPT tip resistance calculated as follows:

$$q_{c1N} = \left(\frac{P_a}{\sigma'_v}\right)^n \left(\frac{q_c}{P_a}\right) \tag{10}$$

where P_a is the atmospheric pressure in the same units used for the vertical effective stress, σ'_v, n is an exponent that varies with soil type from 0.5 to 1.0, and q_c is the field penetration resistance measured at the tip of the cone. A value of *n* equal to 0.5 is appropriate for clean sands and 1.0 for

clayey soils. K_c is a correction factor for grain characteristics and is presented since CPT readings are affected by factors such as fine content, soil plasticity, mineralogy, soil sensitivity, age and stress history (Robertson 2015). K_c can be determined using the following expression:

$$\text{for } I_c \leq 1.64\,; \quad K_c = 1.0 \tag{11}$$

$$\text{for } I_c > 1.64\ ; \quad K_c = -0.403{I_c}^4 + 5.581{I_c}^3 - 21.63{I_c}^2 + 33.75I_c - 17.88 \tag{12}$$

where I_c can be estimated from **Fig. 11**. This chart is commonly used to estimate soil stratigraphy based on the soil behavior measured with the CPT tip and friction resistances. When the sleeve resistance of the CPT test is divided by the effective cone tip resistance, the normalized friction ratio is obtained. The CPT friction ratio usually increases with the increase of the content of fines and the soil plasticity, providing a better indication of the soil type when dealing with fine-grained soils or coarse-grained soils with large amount of fines.

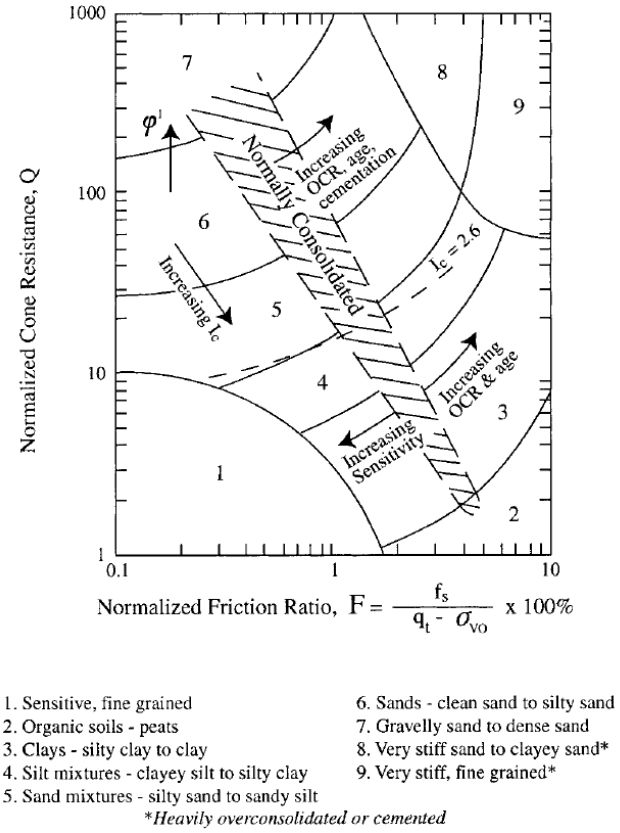

1. Sensitive, fine grained
2. Organic soils - peats
3. Clays - silty clay to clay
4. Silt mixtures - clayey silt to silty clay
5. Sand mixtures - silty sand to sandy silt
6. Sands - clean sand to silty sand
7. Gravelly sand to dense sand
8. Very stiff sand to clayey sand*
9. Very stiff, fine grained*

Heavily overconsolidated or cemented

Fig. 11. CPT-Based soil behavior-type chart (after Robertson and Wride 1998).

The boundaries between different soil types in **Fig. 11** can be approximated by concentric circles where their radius is the index I_c. The following equations can be used for the estimation of that index:

$$I_c = [(3.47 - logQ)^2 + (1.22 + logF)^2]^{0.5} \quad (13)$$

where

$$F = [f_s/(q_c - \sigma_v)] \times 100 \quad (14)$$

and

$$Q = \left[\frac{q_c - \sigma_v}{P_a}\right]\left(\frac{P_a}{\sigma'_v}\right)^n \quad (15)$$

In the above equations, q_c is the measured tip resistance, f_s is the measured cone sleeve resistance, and P_a is a reference stress of 100 kPa (or 1 atm). Robertson and Wride (1998) suggested that for calculating the soil behavior type index, I_c, it is necessary to initially separate different soil types (i.e., clays from sands and silts) and then calculating the dimensionless CPT tip resistance Q from Eq. (15) assuming an exponent n of 1.0.

The next step to calculate the factor of safety against liquefaction is to obtain the CRR normalized to an earthquake magnitude of 7.5 as previously shown in **Fig. 10**. The clean-sand base curve of $CRR_{7.5}$ is commonly approximated with the following equation:

$$\text{if } (q_{c1N})_{cs} < 50\ Mpa \qquad CRR_{7.5} = 0.833\left[\frac{(q_{c1N})_{cs}}{100}\right] + 0.05 \quad (16)$$

$$\text{if } 50 \leq (q_{c1N})_{cs} < 160\ Mpa \quad CRR_{7.5} = 93[(q_{c1N})_{cs}/100]^3 + 0.08 \quad (17)$$

2.1.3 Liquefaction Evaluation using Shear Wave Velocities (V_s)

The $CRR_{7.5}$ can also be estimated using the shear wave velocities, V_s, as proposed by Andrus and Stokoe (1997; 2000). The calculation of the liquefaction resistance using shear wave velocities is

advantageous because they represent a basic mechanical property of the soil and are directly related to small-strain behavior. Youd et al. (2001) summarized three concerns when the measured V_s are used for liquefaction-resistance evaluations: i) seismic wave velocities are measured at small strains whereas the generation of the pore water pressure and the onset of liquefaction typically induce medium to large values of strains in the soil mass, ii) seismic testing does not provide direct soil samples for classification of soils and identification of non-liquefiable soils like most clayey soils, and iii) very thin layers of soils may not be detected in the measurement of the V_s. Thus, other tests like SPT and CPT are also needed to detect liquefiable layers of weakly cemented soils that may have high V_s values. Actually, the combined application of both CPT and shear velocities to evaluate the potential for soil liquefaction is very useful and can be accomplished in a cost-effective way using seismic CPT probes (Robertson 2015).

To assess the liquefaction resistance, a correction of the penetration resistance to account for overburden pressures needs to be applied (Kayen et al. 1992; Robertson et al. 1992; Sykora 1987). This correction can be performed as follows:

$$V_{s1} = V_s \left(\frac{P_a}{\sigma'}\right)^{0.25} \tag{18}$$

where V_{s1} is the shear wave velocity corrected for overburden stress, P_a is the atmospheric pressure taken as 100 kPa, and σ' is the vertical effective stress in the same units as P_a. The application of the previous equation requires a V_s measured in both the directions of the ground motion.

Fig. 12 shows typical CRR versus V_s curves to determine the cyclic resistance ratio. Youd et al. (2001) proposed that the best curve for use in engineering practice is the curve determined by Andrus and Stokoe (2000) which was obtained from field performance data of more than 26 earthquakes for different sites with clean sands.

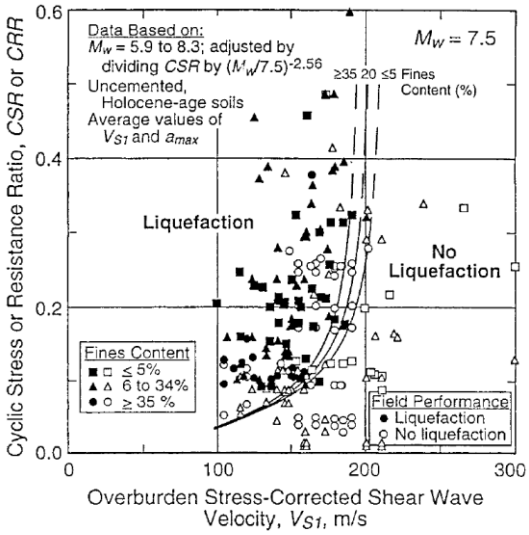

Fig. 12. Relationship between liquefaction resistance and overburden stress-corrected V_S (Youd et al. 2001).

2.2 Calculation of Liquefaction-induced Ground Surface Settlements using Classical Approaches

A major consequence of liquefaction is the volumetric strain that results from the dissipation of excess pore water pressures generated during the earthquake in saturated granular soils. In a free-field condition, lateral flow or spreading are not common failure conditions, thus, these strains are manifested as ground surface settlements. Liquefaction-induced settlements under any structure could result in collapse or partial collapse, especially when differential settlements are induced. Lee and Albaisa (1974) and Yoshimi et al. (1975) studied the volumetric strains and settlements in saturated sands due to dissipation of excess pore water pressures developed during laboratory cyclic loading. They showed that for a given relative density, the volumetric strains increase with the mean grain size of the sand. However, the effects of shear strains were not considered. Tokimatsu and Seed (1986) developed a method correlating the SPT N-value, the earthquake magnitude and induced cyclic stress ratio with induced volumetric strains in saturated sands subjected to an earthquake motion. Later, Ishihara and Yoshimine (1992) developed a similar method correlating the volumetric strain with the relative density and the factor of safety against liquefaction. Their results were in agreement with those proposed by Tokimatsu and Seed (1986).

These procedures are widely used in current state-of-the-practice to predict liquefaction-induced settlements, especially in free-field conditions. However, they were primarily developed for a single layer and not for stratified subsurface conditions. Martin et al. (1991) demonstrated that for stratified soil conditions, the SPT-based method of liquefaction evaluation proposed by Seed (1983) and Seed et al. (1985) could over predict or under predict excess pore water pressures generated in a soil layer. Thus, engineering judgment is essential in stratified soil systems to reasonably estimate settlement values.

Tokimatsu and Seed (1986) proposed the solution shown in **Fig. 13** which shows the variation of the volumetric strain with the corrected SPT N-value for any cyclic stress ratio normalized to a 7.5-magnitude earthquake. Note in **Fig. 13** that the resulting volumetric strains after liquefaction may be as high as 2 or 3% for loose to medium sands and even higher for very loose sands. Then, the settlement of the soil deposit can be integrated over the depth of the soil profile. This can be simplified as multiplying the volumetric strain by the thickness of each layer as follows:

$$S_{sat} = \left({}^{\varepsilon_c}/_{100}\right) d_z \tag{19}$$

where S_{sat} is the computed settlement of the saturated soil deposit, ε_c is the volumetric strain in percentage, and d_z is the thickness of the soil layer.

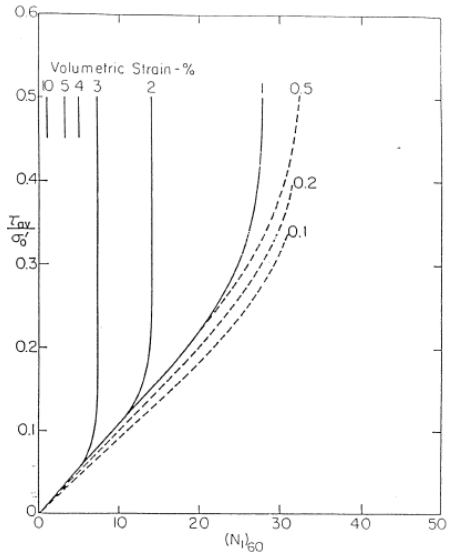

Fig. 13. Relationship between CSR, $(N_1)_{60}$ and volumetric strain for saturated clean sands and earthquake magnitude of 7.5 (after Tokimatsu and Seed 1986).

Ishihara and Yoshimine (1992) proposed the solution shown in **Fig. 14** which uses the factor of safety against liquefaction and either the corrected SPT blow count value or corrected CPT tip resistance to evaluate volumetric strains in the soil. The settlement of the soil can also be calculated using Eq. (19). If the curves in **Fig. 14** are used in conjunction with cyclic triaxial tests, the axial strain (ε_1) obtained from the triaxial tests should be converted to an equivalent shear strain (γ) in the simple shear test using the following equation:

$$\gamma_{max} = 1.5\varepsilon_{1max} \tag{20}$$

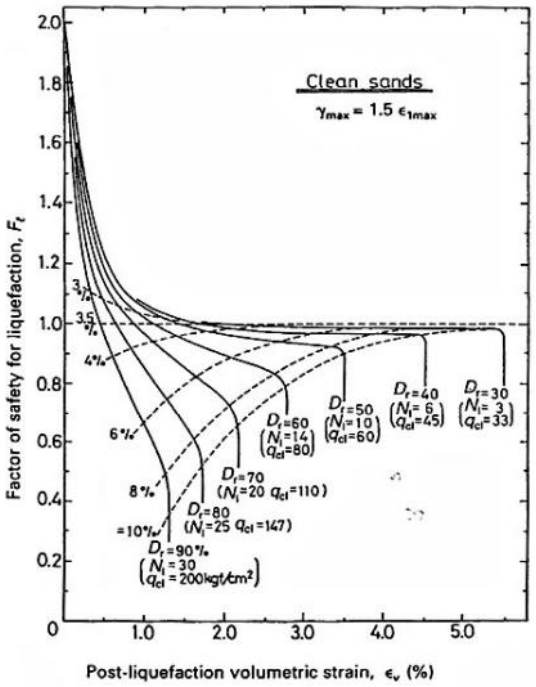

Fig. 14. Volumetric strain as a function of D_r, q_{c1}, SPT N-value and FS against liquefaction (after Ishihara and Yoshimine 1992).

The abovementioned methods are based on free-field conditions and are currently used in practice to assess liquefaction-induced settlements of buildings. In the case of buildings supported in shallow foundations, the separation of volumetric- and deviatoric-induced settlements into conceptual categories (as shown in **Fig. 15**) helps to understand the sequence and mechanisms of liquefaction-induced building movements. Dashti et al. (2013) identified some primary settlement mechanisms from centrifuge experiments. Those primary settlements are: i) volumetric type as a result of partial drainage during earthquake loading, sedimentation, and consolidation; ii) deviatoric

type as a result of partial bearing capacity loss under the static load of the structure; and iii) liquefaction-induced building ratcheting.

Fig. 16 shows the relationship between the width of the building and the average foundation settlement on liquefying sand based on data from the Niigata and Luzon earthquakes. Although the calculation of the seismic response of a shallow foundation on a saturated sand is complicated, Liu and Dobry (1997) developed this empirical chart to demonstrate the relationship between the building width and ground surface settlements normalized with respect to the thickness of the liquefiable layer.

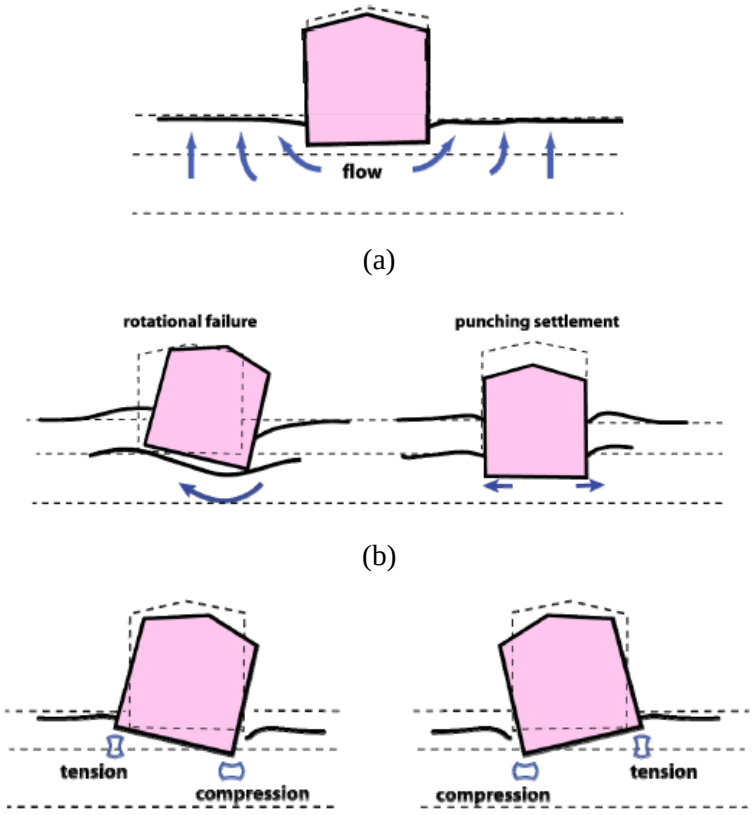

Fig. 15. Primary liquefaction-induced displacement mechanisms: (a) volumetric strains caused by water flow in response to transient gradients; (b) partial bearing capacity failure as a result of soil softening; (c) liquefaction-induced building ratcheting during earthquake loading (Dashti and Bray 2013).

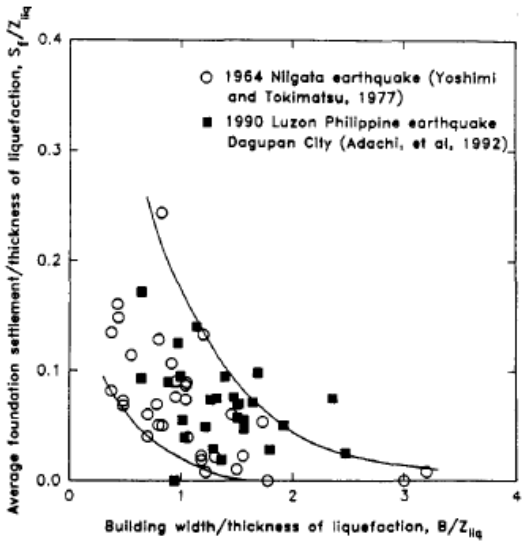

Fig. 16. Normalized foundation settlements versus normalized building width for the 1964 Niigata (Japan) and 1990 Luzon (Philippines) earthquakes (Liu and Dobry 1997).

For buildings supported on deep foundations in liquefiable sands, **Fig. 17** shows different collapse mechanisms observed during strong earthquakes. These collapse modes correspond to the buckling instability in the cases where the pile reaches very firm soils (e.g., rock foundation) and losses the lateral confinement producing internal hinges due to excessive bending moments (see **Fig. 17**a). On the other hand, when the piles are founded in compact sandy soils, the loss of the lateral load capacity produces large vertical deformations causing the collapse of the element (see **Fig. 17**b).

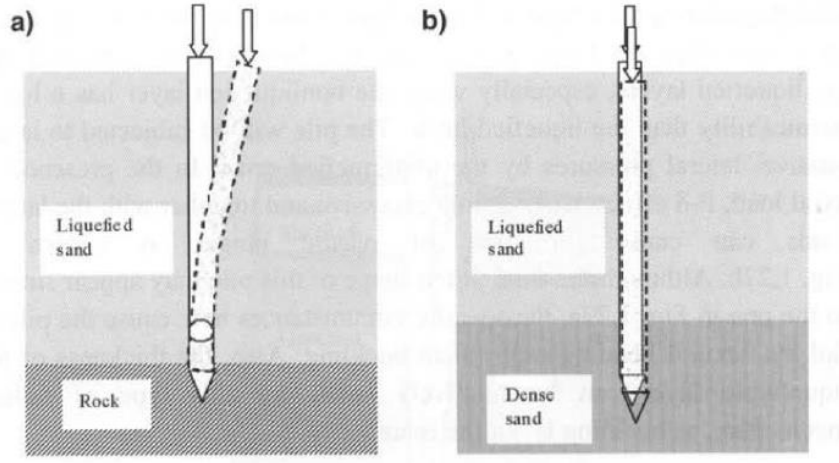

Fig. 17. Collapse modes for individual piles founded in: a) rock, b) compact sandy soils (Madabhushi et al. 2010).

2.3 Limitations in Liquefaction Assessment and Settlements Evaluation using current Semi-Empirical Methods

The procedures available for evaluating the potential for liquefaction triggering are based on field tests as the SPT, CPT and measurements of V_s. These methods are based on case histories when liquefaction was observed. Most current methods are based on free-field conditions, ignoring the changes in the static shear stress induced by the structure and the redistribution of excess pore water pressures during shaking. These limitations ignore the resulting changes in the amplitude and frequency content of the ground motion (Byrne et al. 2004; Dashti 2009; Lopez-Caballero and Modaressi Farahmand-Razavi 2008).

The current methods used to estimate the factor of safety against bearing capacity failure of a structure using simplified pseudostatic approaches based on total stresses, cannot capture the process that triggered failure. Methods as the ones proposed by Tokimatsu and Seed (1986) and Ishihara and Yoshimine (1992), assess liquefaction-induced building settlements trying to capture post-liquefaction reconsolidation settlements in the free-field but are not applicable to cases involving buildings supported on shallow or deep foundations. Hence, the evaluation of liquefaction-induced building settlement is still subject of study and more research is needed to understand its mechanisms.

2.4 UBC3D-PLM Constitutive Soil Model for Liquefaction Evaluation

For the dynamic analyses performed in this research, the UBC3D-PLM constitutive soil model was used. This model is a 3D generalized formulation based on a two-dimensional model originally called UBCSAND model introduced by Puebla et al. (1997) and Beaty and Byrne (1998). Tsegaye (2010) developed the first 3D formulation of the model coded as a user defined model in PLAXIS. Then, Galavi and Petalas (2013) enhanced the model by introducing a correction in the calculation of the plastic multiplier improving the model capabilities, particularly during monotonic loading. The formulation of the original UBCSAND model is based on the classical plasticity theory with a hyperbolic strain hardening rule based on the Duncan-Chang approach with slight modifications introduced by Galavi and Petalas (2013). The UBC3D-PLM model uses a Mohr-Coulomb yielding condition in a three-dimensional principal stress space and a modified non-associated plastic potential function (Tsegaye 2010) based on the Drucker-Prager´s criterion.

The UBC3D-PLM model is an elasto-plastic model capable to develop excess pore water pressures and capture the liquefaction phenomenon of soils, particularly the onset of liquefaction due to dynamic loading is reasonably captured by the model. As in any elasto-plasticity based model, the strains are decomposed in elastic and plastic. In the elastic regime, the behavior is non-linear and dependent on the elastic bulk and shear moduli (i.e., K and G, respectively) and is assumed isotropic (Petalas and Galavi 2013). These two moduli are stress-dependent and can be determined using the following relationships:

$$K = K_B^e P_A \left(\frac{p}{P_A}\right)^{me} \tag{21}$$

$$G = K_G^e P_A \left(\frac{p}{P_A}\right)^{ne} \tag{22}$$

where K_B^e and K_G^e represent the bulk and the shear moduli numbers at the atmospheric pressure, usually taken as P_A =100 kPa; p is the mean effective stress; and me and ne are parameters which define the rate of stress dependency of stiffness.

In the model, the plastic behavior is reached when the stress state reaches the yield surface. From thereon, irrecoverable deformations occur. The model includes a hardening rule derived from a Mohr-Coulomb yielding criterion. It governs the amount of plastic strains developed after the mobilization of shear stress.

In order to represent in the model, the complexity of the three-dimensional yield surfaces, six combinations of principal stresses have been introduced in the model to define the three-dimensional principal stress space, which is based on a Mohr-Coulomb failure criterion in terms of the maximum and minimum stress components. The function that describes the yield surface in the model is given by the following expression:

$$f_m = \frac{\sigma'_{max} - \sigma'_{min}}{2} - \left(\frac{\sigma'_{max} + \sigma'_{min}}{2} + c' cot\, \phi'_p\right) \sin \phi_{mob} \tag{23}$$

where σ'_{max} and σ'_{min} correspond to the maximum and minimum principal effective stresses, the term $c' \cot \phi'_p$ defines the point in which the mean effective stress intersects the yield surface and

ϕ_{mob} is the mobilized friction angle. **Fig. 18** shows the projection of the Mohr-Coulomb yielding criterion in the π-plane.

The mobilized friction angle can be calculated using the following equation:

$$\sin\phi_{mob} = \frac{\sigma'_1 - \sigma'_3}{\sigma'_1 + \sigma'_3} = \frac{t_{mob}}{s'} \tag{24}$$

where t_{mob} is the mobilized shear stress and s' is the mean effective stress. Further increase of the ratio shear to mean effective stresses results in larger plastic strains.

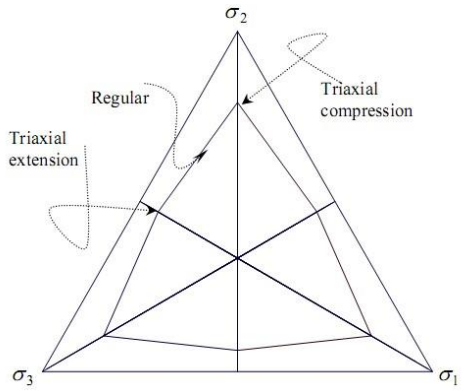

Fig. 18. Projection of the yield surface in the deviatoric plane (Petalas and Galavi 2013).

The hardening rule used in the original version of the UBCSAND model presented by Puebla et al. (1997) was reformulated by Tsegaye (2010) in the UBC3D-PLM model using the hyperbolic hardening rule proposed by Beaty and Byrne (1998) which is presented schematically in **Fig. 19**. The hardening rule for the UBC3D-PLM model is given as:

$$d\sin\phi_{mob} = 1.5K_G^p\left(\frac{p}{p_A}\right)^{np}\frac{p_A}{p}\left(\frac{\sin\phi_{mob}}{\sin\phi_{peak}}R_f\right)^2 d\lambda \tag{25}$$

where np is a model parameter to describe the stress dependency of the plastic shear modulus, $d\lambda$ is the plastic strain increment multiplier, ϕ_{peak} is the peak friction angle, and R_f is the failure ratio which is always taken less than 1 and K_G^p is the plastic shear modulus number as defined in Eq. (26).

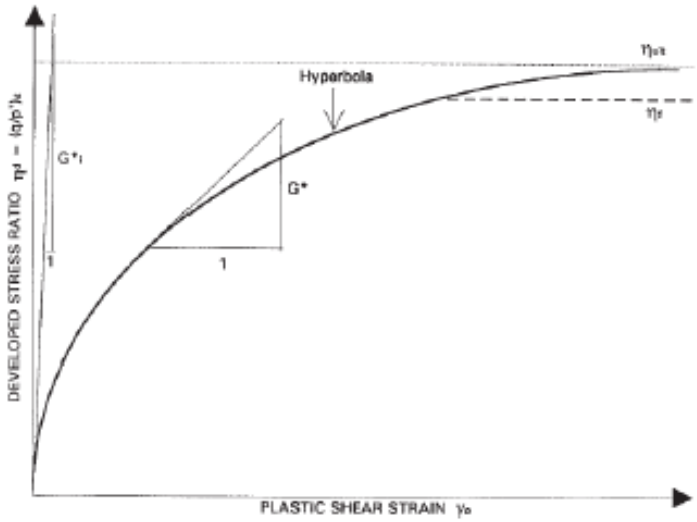

Fig. 19. Hyperbolic hardening rule of the original UBCSAND model and adopted in the UBC3D-PLM model (Petalas and Galavi 2013).

$$G^p = K_G^p P_A \left(\frac{p}{P_A}\right)^{np} \tag{26}$$

In Eq. (26), G^p represents the plastic shear modulus. The plastic potential function of the model, which describes the direction of the development of plastic strains, is based on a Drucker-Prager non-associated flow rule and is defined with the following expression (Tsegaye 2010):

$$g = q - a(p' + c' \cot \phi_p) \tag{27}$$

where p', q and the coefficient a are given as:

$$a = \frac{\sqrt{3} \sin \psi_{mob}}{\cos \theta + \frac{\sin \theta \sin \psi}{\sqrt{3}}} \tag{28}$$

$$q = \sigma_1 - \sigma_3 \tag{29}$$

$$p' = \frac{\sigma'_1 + \sigma'_2 + \sigma'_3}{3} \tag{30}$$

where ψ is the dilatancy angle and θ is the Lode angle equal to 30° because the Drucker-Prager surface is fixed in the compression point (Petalas and Galavi 2013) and $\sigma_1, \sigma_2, \sigma_3$ are principal stresses.

The flow rule of the UBC3D-PLM model is similar to the flow rule originally used in UBCSAND model by Puebla (1997) which describes that plastic shear strains do not produce plastic volumetric strains based on the Rowe's stress dilatancy relation as shown in **Fig. 20**.

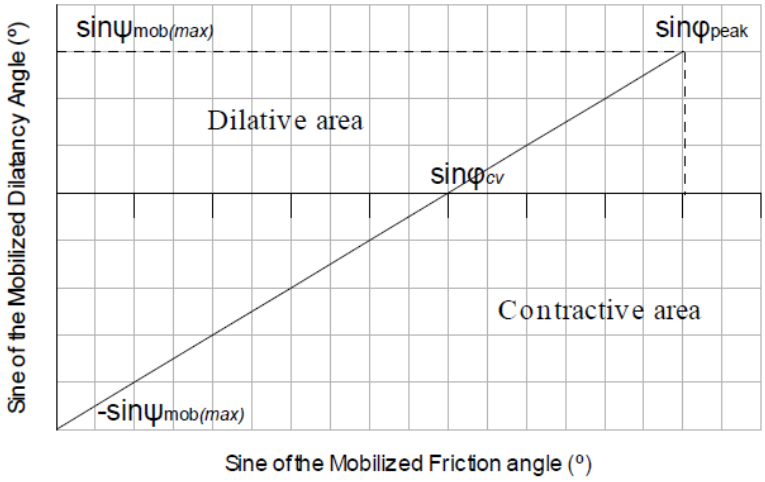

Fig. 20. Representation of the modified Rowe's flow rule used in UBC3D-PLM model (Petalas and Galavi 2013).

The relationship between plastic shear strains and plastic volumetric strains is given as follows:

$$d\epsilon_v^p = \sin\psi_m \, d\gamma^p \tag{31}$$

where

$$\sin\psi_m = \sin\phi_m - \sin\phi_{cv} \tag{32}$$

Equations (31) and (32) describe the increment of plastic volumetric strains, $d\epsilon_v^p$, with the increment of plastic shear strains, $d\gamma^p$, affected by the mobilized dilatancy angle ψ_m.

The model captures the transition to the liquefaction state of the soil by including a secondary yield surface that generates less plastic strains than those generated with the primary yield surface. It is

possible mainly because the primary yield surface uses an anisotropic hardening rule, whereas the secondary yield surface uses a kinematic hardening rule (Galavi et al. 2013). For the secondary loading, the plastic shear modulus increases with each loading cycle to capture the effect of soil densification, which is shown in the following expression:

$$K_G^p = K_{G,primary}^p * \left(4 + \frac{n_{rev}}{2}\right) * hard * fac_{hard} \tag{33}$$

where n_{rev} is the number of the half cycles generated from the beginning of the test, *hard* is a factor which is used to apply a densification rule for loose soils subjected to cyclic loading, fac_{hard} is a multiplier factor varying between 0 and 1 which is used to adjust the densification rule, and $K_{G,primary}^p$ is the initial value of K_G^p entered for the primary yield surface.

To capture the post-liquefaction behavior of loose granular soils and the stiffness degradation of soils, the UBC3D-PLM model incorporates a post-liquefaction rule to account for the decrease of the plastic shear modulus as a function of the plastic shear strains. This equation is expressed as follows:

$$K_G^p = K_{G,primary}^p * e^{\min(110\varepsilon_{dil}, fac_{post})} \tag{34}$$

where ε_{dil} describes the accumulation of the plastic deviatoric strains generated during dilation of the soil and the factor denoted as fac_{post} represents an exponential multiplier that controls the plastic behavior of the soil at the post-liquefaction state. Previous studies have shown that the larger the fac_{post} factor, the smaller the plastic strains generated at the end of the earthquake (Galavi et al. 2013). **Fig. 21** shows horizontal displacements of a quay-wall located in Kobe (Japan) (Galavi et al. 2013) as the Hyogoken-Nambu earthquake 1995 occurred. In the figure, fac_{post} factor was varied parametrically to show the relative importance of this factor on the resulting plastic strains and associated displacements at the foundation level.

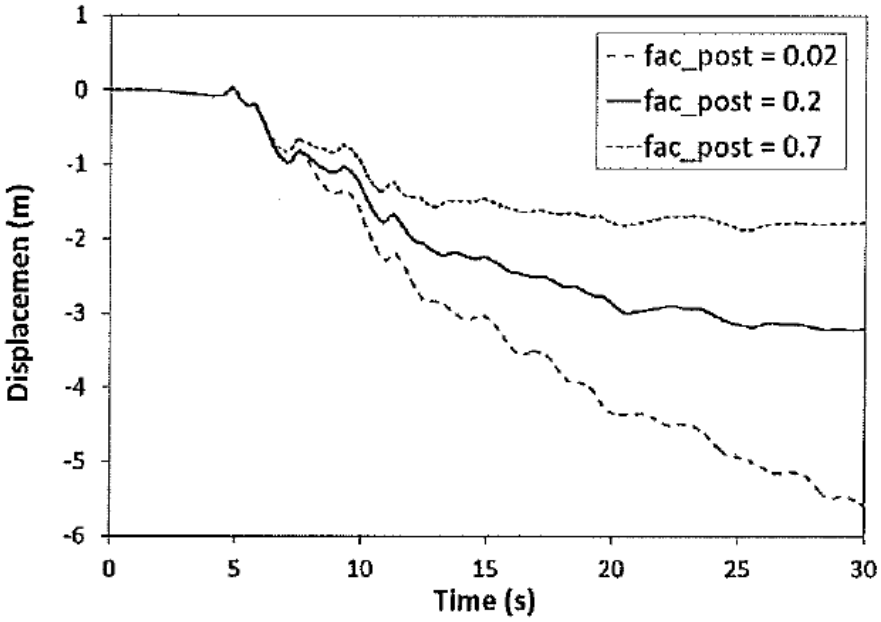

Fig. 21. Effect of fac_{post} parameter on the computed horizontal displacement in a quay wall in Kobe (Japan) during the Hyogoken-Nambu Earthquake in 1995 (Galavi et al. 2013).

The UBC3D-PLM requires the input of 16 constitutive soil parameters calibrated based on experimental results from laboratory tests. **Table 1** presents a description of the input parameters for the constitutive model. The recommended method to define the input parameter is to perform laboratory tests that follow a similar stress path that the soil will follow in the field. For earthquake engineering applications, especially when dealing with liquefiable soils, undrained cyclic Direct Simple Shear (DSS) tests are the best and most common way to obtain constitutive soil parameters. Ideally, the soil parameters are calibrated by fitting the model response to the soil response as obtained from undrained cyclic DSS tests. The parameters are typically calibrated from stress-strain, stress paths, and cyclic strength curves of the material under laboratory confining pressures similar to those currently present in the field. The input value for $(N_1)_{60}$ is obtained from standard penetration field tests.

Table 1. Input parameters for the UBC3D-PLM model (after Petalas and Galavi 2013)

Parameter	Description
ϕ_{cv}	Friction angle at constant volume
ϕ_p	Peak friction angle
c	Cohesion intercept of Mohr-Coulomb envelope
K_B^e	Elastic bulk moduli at the reference pressure (Pa = 100 kPa)
K_G^e	Elastic shear moduli at the reference pressure (Pa = 100 kPa)
K_G^p	Drained plastic shear modulus
me	Elastic bulk moduli exponent
ne	Elastic shear moduli exponent
np	Plastic shear moduli exponent
R_f	Failure ratio
σ_t	Tension Cut-off
fac_{hard}	Densification factor
$(N_1)_{60}$	Corrected SPT value
fac_{post}	Factor for minimum value of the shear moduli
Pa	Reference pressure equal to the atmospheric pressure in kPa

2.5 Case Histories in the use of the UBC Model to Evaluate Liquefaction Potential

Other case histories on the Niigata 1964 (Japan) and Dagupan City 1990 (Philippines) earthquakes have provided in the past insight about the seismic performance of structures founded on liquefiable sands (Dashti and Bray 2013). For this reason, several centrifuge test were performed by Dashti et al. (2010a; b) with the main goal to identify the mechanisms of liquefaction-induced building settlements and to assess the influence of different factors on the building's response when founded on shallow foundations. In that study, the results of the centrifuge testing were later compared with the results of numerical simulations based on fully coupled analyses using the UBCSAND constitutive soil model coded in the computer program FLAC-2D. The numerical simulations were oriented to capture the soil response and the liquefaction-induced building settlement considering that most of the procedures available up to that point were based only on free-field conditions and typically neglect the detrimental effects of liquefaction on structures.

Another field of application of numerical and constitutive modeling applied in geotechnical earthquake engineering is the response of embankments and earth-fill dams subjected to earthquake loading. After the San Fernando 1971 earthquake, which resulted in the failure of the upper and lower San Fernando dam, research on the behavior of these type of structures when subjected to earthquake loading became essential to gain deep understanding of the liquefaction mechanisms that may cause damage to the existing infrastructure. Several researchers, as Seed et al. (1973, 1976, 1988) Castro et al. (1989), Vasquez-Herrera and Dobry (1988), Olsen and Stark (2001), among others, have discussed the most critical aspects associated with flow failures and liquefaction-induced damage of foundations in dams, with significant advances in the field of dam design and specifications.

Petalas and Galavi (2013) proposed the UBC3D-PLM model as an implementation and extension of the UBCSAND model but in the finite element program PLAXIS 2D, and validated the constitutive model with the results of centrifuge tests. The results of the predicted evolution of excess pore water pressures are shown in **Fig. 22** for different depths in a cohesionless soil deposit. As shown in the figure, and as previously stated by Dashti (2012) for the UBCSAND, the model is capable to predict the onset of liquefaction with more accuracy at low confining stresses. For larger stresses, the model tends to over predict the evolution of excess pore water pressures and larger discrepancies are observed in relation to experimental measurements. This is mainly attributed to the stress densification rule used by the model.

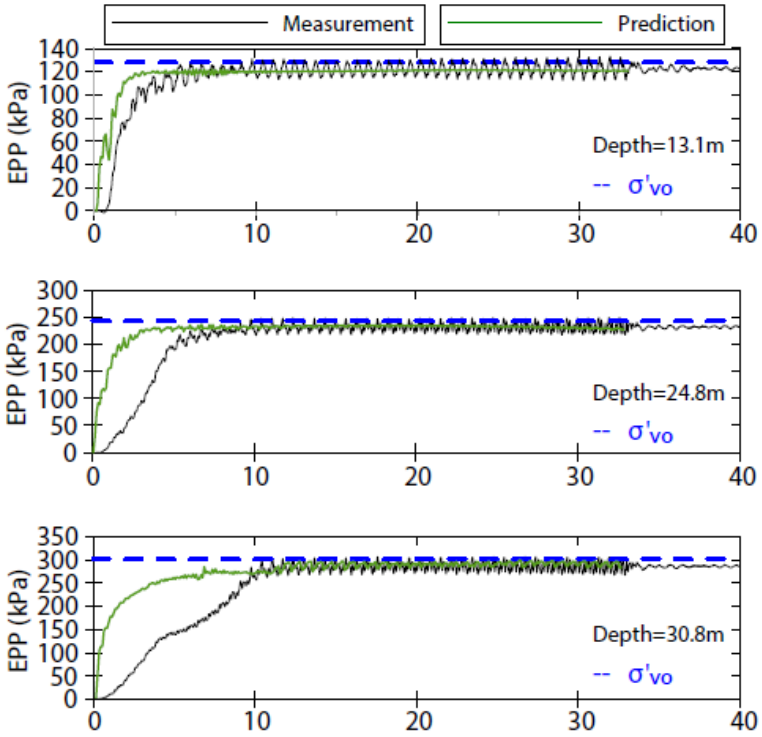

Fig. 22. Comparison of the predicted development of excess pore water pressures computed with the UBC3D-PLM and measured with centrifuge tests (Petalas and Galavi 2013).

Also, Galavi et al. (2013) presented a comparison of the UBC3D-PLM model, the original UBCSAND model, and experimental results of loose Syncrude sands under monotonic triaxial compression (TXC) and monotonic direct simple shear (DSS) tests. The results are presented in **Fig. 23**. The simulation results using both constitutive soil models reasonably match the experimental results. The slight differences between computed values using both models are due to the newly added features by Petalas and Galavi (2013) to the UBC3D-PLM model.

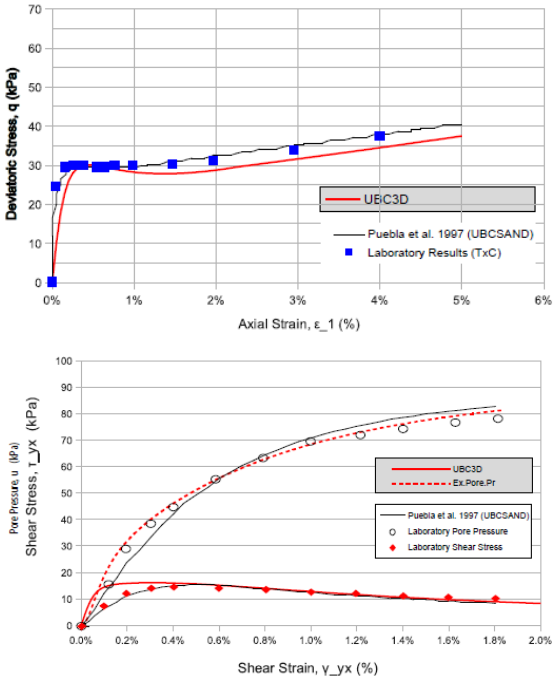

Fig. 23. Comparisons of numerical simulations of loose Syncrude sands subjected to monotonic loading using the UBC3D-PLM and UBCSAND models (Petalas and Galavi 2013).

More recently, Makra (2013) used the UBC3D-PLM constitutive soil model as implemented in PLAXIS 2D to evaluate the ability of the model to predict the onset of liquefaction and post-liquefaction induced deformations applied to the San Fernando dam in California. After calibrating constitutive soil parameters from undrained cyclic triaxial tests and results of centrifuge tests, and after performing numerical simulations of the San Fernando dam, the author concluded that the post-liquefaction behavior cannot be accurately computed with the model. However, numerous features of soil behavior and mainly the onset of liquefaction can be reasonably captured as it is quantified as a reduction in the effective stresses in the soil mass in relation to large values of pore water pressures developed as the earthquake occurs.

The development of the UBC3D-PLM constitutive soil model implemented in PLAXIS 2D is based on the UBCSAND model as originally implemented in FLAC. Several researchers have developed comparisons between the results obtained with both models as coded in both programs. Tasiapoulou et al. (2015) presented the behavior of a multi-block gravity quay-wall comparing the results of both numerical models coded in PLAXIS 2D and FLAC. **Fig. 24** shows the results of the dynamic analyses using both approaches that resulted in similar computed horizontal and vertical deformations.

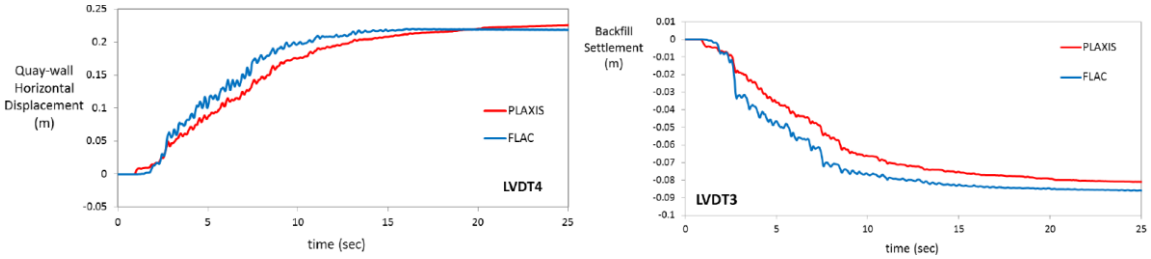

Fig. 24. Horizontal and vertical deformations of the quay-wall using both PLAXIS 2D and FLAC (after Tasiopoulou et al. 2015).

3. SEISMICITY OF THE PORT OF LONG BEACH

3.1 Site Description of Port of Long Beach

The Port of Long Beach (POLB), which is the second busiest seaport in the United States, is located near the San Pedro Bay in the city of Los Angeles (CA), as shown in **Fig. 25**. The port is an important transportation center moving a great variety of goods including but not limited to clothing, furniture, machinery, and petroleum. This research focuses in the Pier S, which is a 290 ha area of the POLB located on the eastern half of the bay. Future expansion projects of the port are proposed in the location of Pier S. The proposed 65 ha expansion would result in the world's greenest shipping terminal. This construction includes the development of a wharf and terminal infrastructure at Pier S including some buildings and miner structures. Pier S projects future improvements to the port's back channel to upgrade navigational safety.

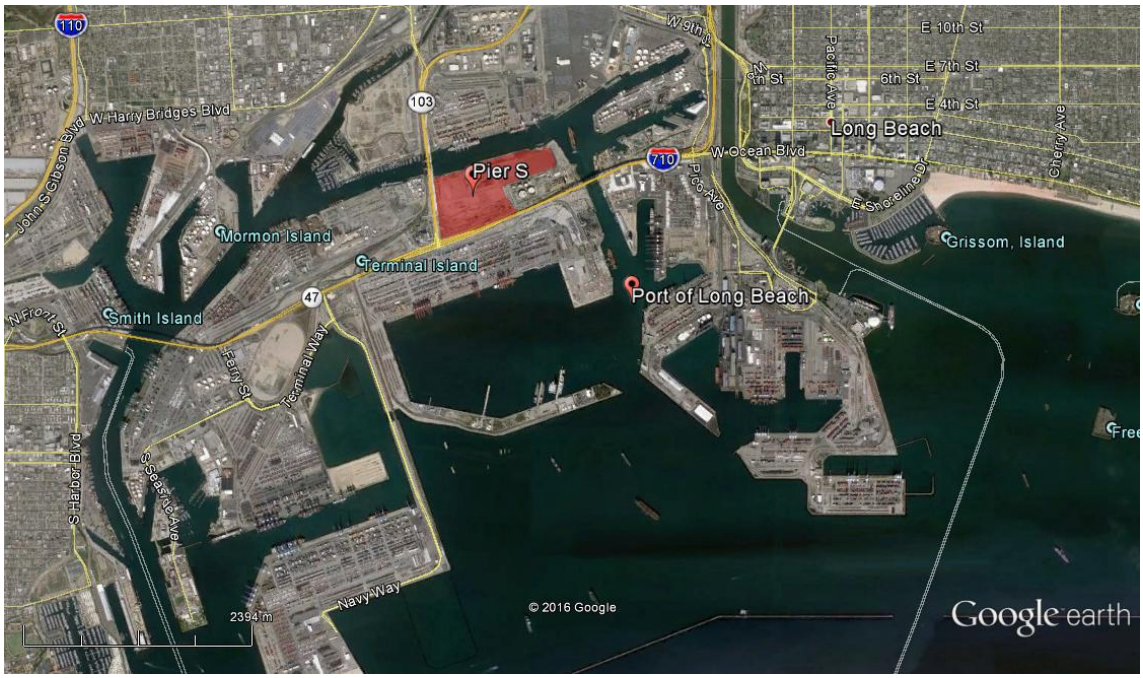

Fig. 25. Site location map (after Google Earth 2016).

3.2 Geologic conditions and predominant faults at the POLB

The Los Angeles basin floor is characterized by unconsolidated sediments from the Holocene age with the exception of some local formations from the Pleistocene age present in the small hills and mesas. Similar characteristics are typical of the POLB subsurface and immediate offshore areas. The Pleistocene materials consists of both non-marine and marine deposits which are commonly referred to as Lakewood and San Pedro formations which provide firm-ground conditions at the POLB.

As shown in **Fig. 26**, the POLB is located in the coastal area of Los Angeles in a low-lying plain at the south of the Santa Monica Mountains, the Repetto and Puente Hill formations. The figure also shows the regional set of faults in the vicinity of the port. The amount of regional faults present in the area serve as an indication of the potential seismic activity in the port area. Most of the surface geological faults such as the Santa Monica, Hollywood, and Whittier faults that occur along the basin margins and the Los Angeles region are triggered by the subsurface thrust and reverse faults as shown in **Fig. 26** with dotted lines. Historically, large magnitude earthquakes associated with these geologic structures, like the Whittier 1987 earthquake, have been originated at depths between 10 and 15 km (Earth Mechanics Inc. 2006).

The regional geologic structure across the greater Los Angeles area is characterized by the north-northeasterly compression with a displacement rates between 5 and 9 mm per year. **Fig. 27** presents some of the geological structures near the area of POLB that contribute to the seismicity of the port. This geological structure is related to the tectonic activity in the Long Beach region during quaternary times and seems to have occurred along the strike-slip faults of Palos Verdes and Newport-Inglewood Structural Zone (NISZ). These two faults represent the main source of seismic activity at the location of the POLB. As a result of the deformation along the Newport-Inglewood fault, the THUMS-Huntington Beach (THB) fault, and the Palos Verdes fault, several folds are apparent in the POLB area like the Wilmington and Signal Hill anticlines and the intervening Gardena and Harbor-Wilmington synclines. Several north-south trending cross-cutting faults are also present like the Powerline, Harbor Entrance, and Daisy Avenue faults which are currently inactive. **Fig. 27** also presents two characteristic geological cross sections (A-A’ and B-B’) which are shown to describe the site stratigraphy and geologic structure present in the POLB area.

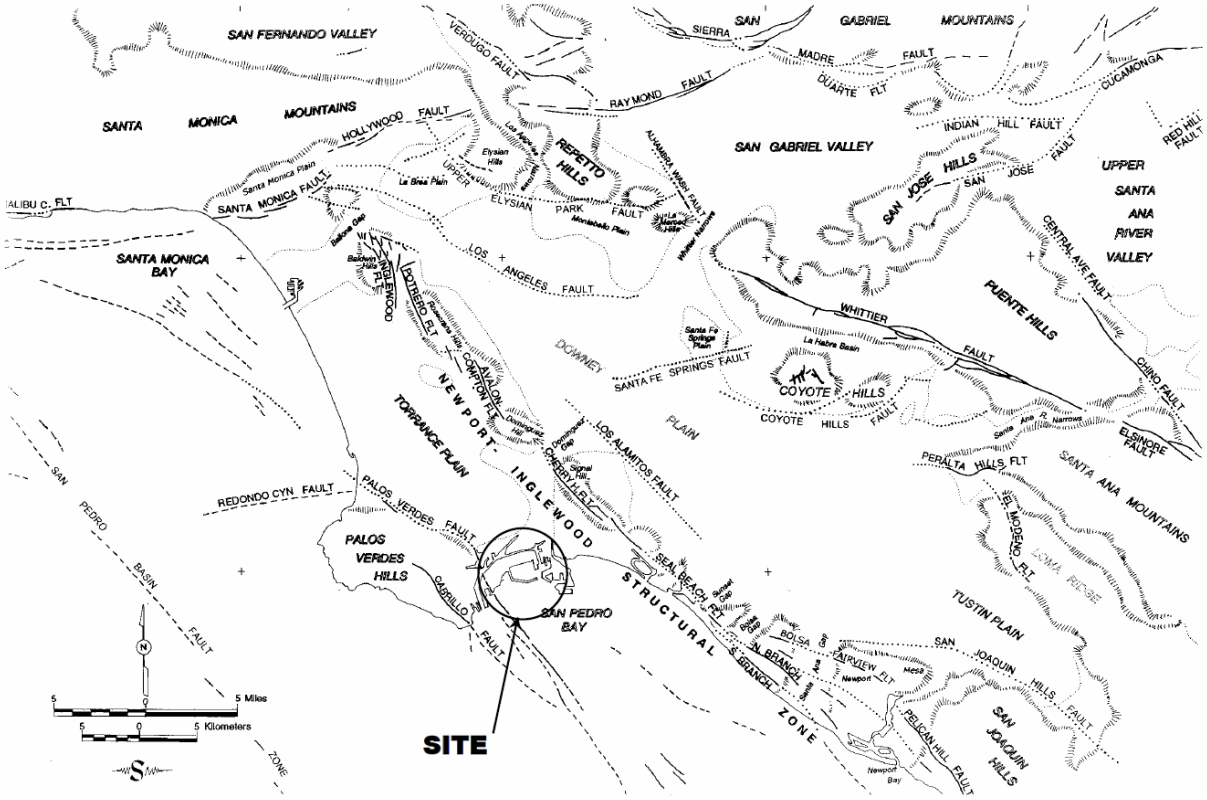

Fig. 26. Regional fault and physiography map of the Los Angeles greater area (Earth Mechanics Inc. 2006).

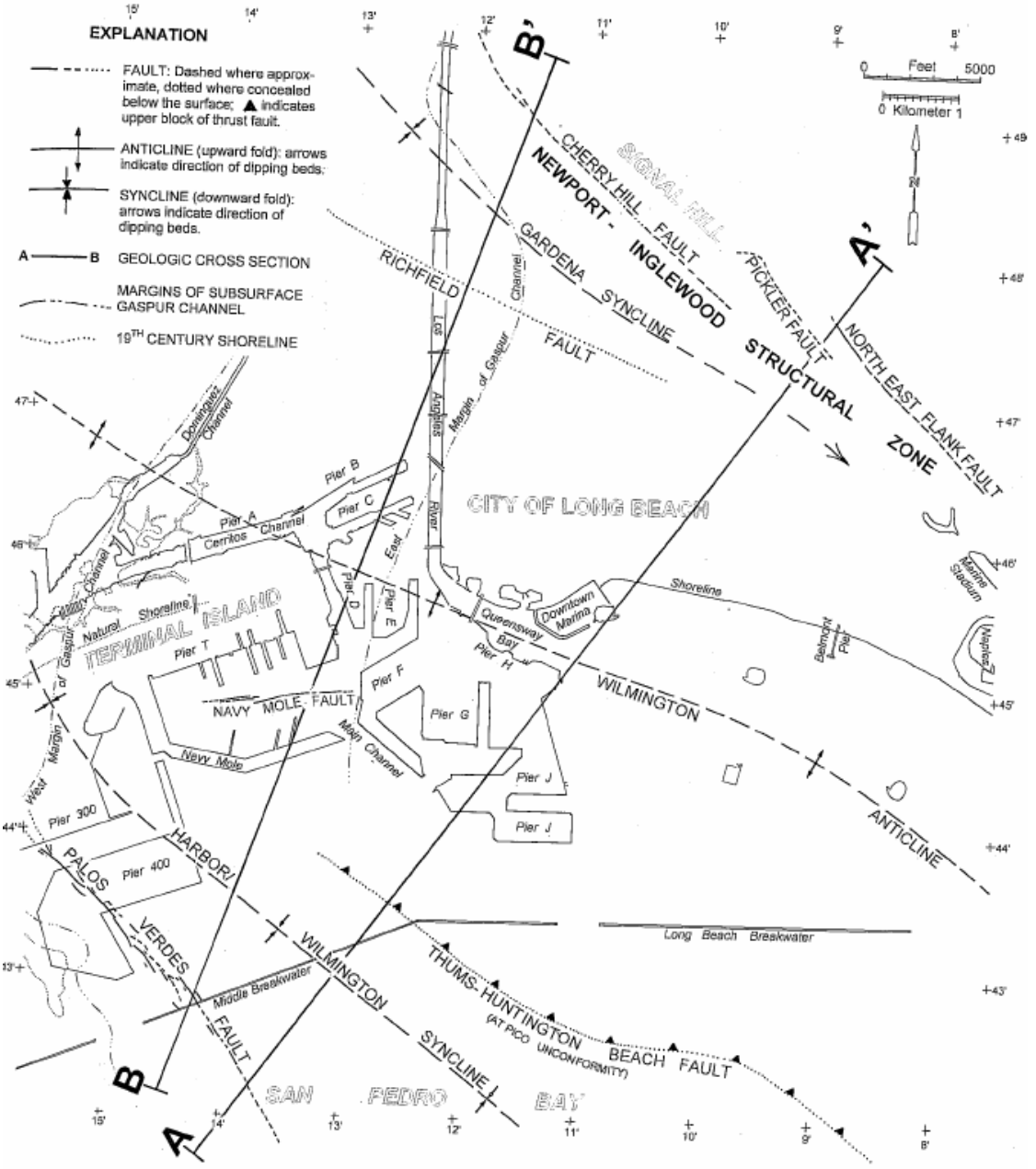

Fig. 27. Geologic structure map of POLB area (Earth Mechanics Inc. 2006).

The sections presented in **Fig. 28** and **Fig. 29**, show the fills and miscellaneous superficial sediments overlying older sediment deposits from the Pleistocene-age Lakewood Formation which in turn overlies the early Pleistocene San Pedro formation. The underlying strata comprise folded and faulted Pliocene and Miocene age formations, and the major angular Pico unconformity, between the Quaternary and upper Pliocene sediments from the lower Pliocene-Miocene deposits and the Catalina Schist basement (Earth Mechanics Inc. 2006). The Pico unconformity indicates

that the major folding of the Wilmington Anticline occurred before the Quaternary time. The San Pedro Formation overlies marine sediments and sedimentary rocks like the Pico, Repetto and Monterey Puente formations. At the same time, these sediments overlie Mesozoic-age crystalline basement rocks which are primarily schist metamorphic rocks. Several major folds and faults are shown in the figures. The major folds represent the Wilmington and Signal Hill anticlines and the intervening Gardena and Harbor-Wilmington synclines, that are the result of the deformation along the NISZ, THB and Palos Verdes faults. Inactive numerous minor north-south trending cross-cutting faults are also present in the region of the POLB as shown in **Fig. 28** and **Fig. 29**. These include but are not limited to the Powerline, Harbor Entrance and Daisy Avenue faults.

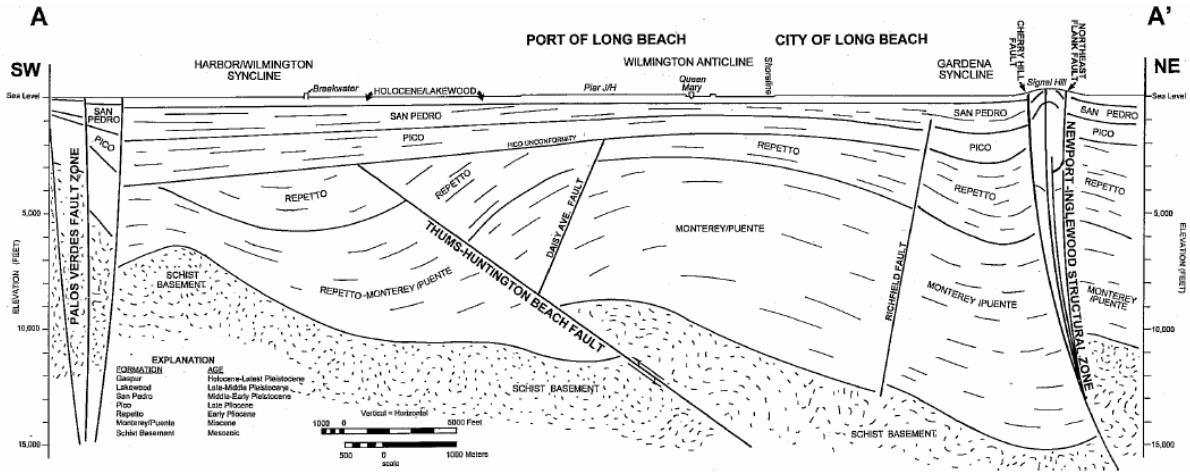

Fig. 28. Geological cross section A-A' of POLB area (Earth Mechanics Inc. 2006).

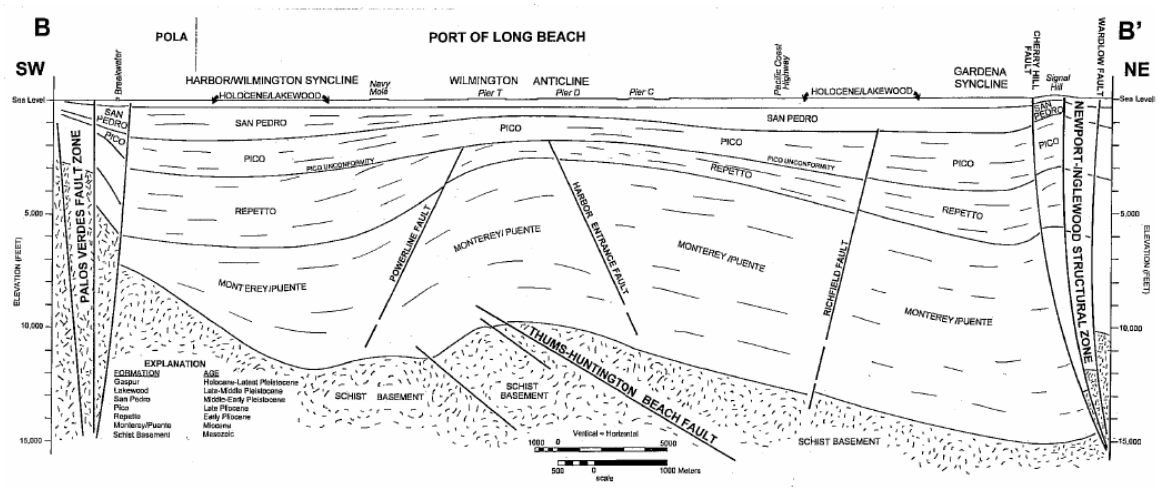

Fig. 29. Geological cross section B-B' of POLB area (Earth Mechanics Inc. 2006).

A summary of the active faults within the area of Los Angeles that contribute to the high probability of occurrence of seismic activity in the POLB area is described in the following sections as presented in the Port Wide Ground Motion report by Earth Mechanics Inc. (2006) and the Fault Evaluation Report FER-173 by Bryant (1985).

3.2.1 Palos Verdes Fault

The Palos Verdes fault as shown previously in **Fig. 26** extends through the Port of Los Angeles from the east side of the Palos Verdes Peninsula southeasterly to the Lasuen Knoll area offshore and northwesterly into the Santa Monica Bay, with a total length of 100 km approximately. Under the north part of the San Pedro shelf, the fault zone includes several strands, with the main strand dipping west. To the southeast the main fault strand exhibits normal separation and mostly dips east. To the southeast near Lasuen Knoll, the fault zone locally dips at a low angle, but elsewhere near this knoll, the fault dips steeply. Fisher et al. (2004) explain the observed structural variations as the result of changes in strike and fault geometry along a master right-lateral strike-slip fault at depth. Onshore, the Palos Verdes fault has a northwesterly trend along the northeast margin of the peninsula forming a restraining bend in the region just north of the Port of Los Angeles. The fault appears to dip southwesterly under the Palos Verdes Hills at a relatively steep angle. Woodring et al. (1946) and Zielbauer et al. (1962) show the Palos Verdes fault to be generally coincident with the topographic break along the northern and northeast margin of the Palos Verdes Hills but there are many interpretations that suggest locations upslope within the Palos Verdes Hills.

Nardin and Henyey (1978), Clark et al. (1987), and Fisher et al. (2004) found little evidence of faults displacing strata any younger than Pliocene, and thus Quaternary activity on the northern Palos Verdes fault is uncertain. The Palos Verdes fault is predominantly a strike-slip fault but has a small vertical component of about 10% to 15%. The slip rate of the Palos Verdes fault is based primarily on the geophysical and geological studies in the outer harbor of the Port of Los Angeles performed by McNeilan et al. (1996). In that study, it was estimated that the horizontal slip rate varied between 2.0 and 3.5 mm per year with a range of about 2.3 to 3.0 mm per year for the middle- to late- Holocene time period.

There are virtually no direct data to constrain the recurrence interval for large earthquakes on the Palos Verdes fault. Using the empirical data of Wells and Coppersmith (1994) this fault is capable to generate a magnitude 6.8 to 7.4 earthquake. It appears that recurrence intervals for such

earthquakes on the Palos Verdes fault would range from a few hundred to a few thousand years. The fault rupture scenarios evaluated by McNeilan et al. (1996) ranged from 180 to 630 years for a magnitude 6.8 event, 400 to 440 years for a magnitude 7.1 event, 1,000-1,100 years for a magnitude 7.2 event, and 830 to 1,820 years for a magnitude 7.4 event. Previous seismic hazard analyses for the Port of Los Angeles and the Vincent Thomas bridge (Earth Mechanics Inc. 1993, 1995, 2001) used recurrence intervals in the middle of the range (i.e., 800-900 years).

3.2.2 Newport-Inglewood Structural Zone

The Newport-Inglewood Structural Zone (NISZ), as shown previously in **Fig. 26**, consists of a northwest-southeast trending series of faults and folds forming an alignment of hills in the western Los Angeles Basin extending from the Baldwin Hills on the north to Newport Mesa on the south. The fault seems to have originated in about late Miocene time but based on relative stratigraphic thickness of bedding across the zone, the greatest activity seems to have been post-Pliocene indicating the fault is rather young.

The NISZ includes several individual faults and other branch faults (as shown in **Fig. 26**, **Fig. 27**, **Fig. 28** and **Fig. 29**) that have good surface expression as actual fault scarps. These faults are relatively linear and narrow along the central part of the zone in the Long Beach-Seal Beach area. To the north of Dominguez Hill, the faults are shorter, less continuous, and exhibit a left-stepping arrangement with several folds between fault branches. In the south near Costa Mesa and Newport Beach, the NISZ extends to about 5 or 6 km where it includes several subparallel faults such as the Bolsa, Fairview, and Pelican Hill faults. The NISZ extends offshore to about the Dana Point area. To the south, the fault is believed to connect via the Offshore Zone of Deformation near San Onofre to the Rose Canyon fault in the San Diego region forming a major structural trend commonly referred to as the Santa Monica-Baja Zone of Deformation (SMB).

The NISZ has been hypothesized to be capable of generating a magnitude 7.0 earthquake. This may be relatively small as long as the SMB zone but the magnitude is based on the concept that the zone consists of shorter discontinuous faults that behave independently. This fault was the source of the 1993 Long Beach earthquake of magnitude 6.3, but as with the Palos Verdes fault, the history of earthquakes on the NISZ is incomplete so it is difficult to predict a maximum earthquake. The recurrence interval for the maximum earthquake on the NISZ has the order of a thousand years or more (Freeman et al. 1992; Grant et al. 1997; Schell 1991; Shlemon et al. 1995). These studies,

using cone penetrometers mostly in the Huntington Beach area, suggested average recurrence intervals of about 2,000 to 3,500 years per event.

The rate of fault slip was inferred to be very slow and as suggested by Grant et al. (1997), a minimum rate of 0.34 to 0.55 mm per year is plausible but might be higher. Shlemon et al. (1995) estimated a rate of 1.5 to 2.5 mm per year. However, most of the deformation within the NISZ seems to have occurred within Quaternary time so the rate during more recent times may differ from the long-term rate.

3.2.3 Other Faults Present in the Greater Los Angeles Area

Other important faults present in the greater Los Angeles area, but not necessarily nearby or passing directly through the POLB, include the Cabrillo fault, the Sierra Madre fault, Santa Monica/Hollywood fault, San Pedro fault, Elysian Park fold and Thrust Belt, and the Puente Hills Formation. These faults are briefly described in this section because they can also generate significant seismic activity to the POLB area. There are some minor faults on the offshore San Pedro shelf that were detected by various geophysical surveys for local pipelines. These features are too small and discontinuous to represent a seismic hazard and therefore are not significant for seismic design. An example of this type of feature is the Navy Mole Fault as shown previously on **Fig. 27**.

The Cabrillo fault forms a prominent northeast facing scarp in the San Pedro-Point Fermin area. The fault dips about 50° to 70° easterly and trends northwesterly inland for about 7 km (Dibblee 1999; Woodring et al. 1946). Southerly from Cabrillo Beach, the fault extends offshore for a distance of about 11 km where it seems to merge with the Palos Verdes fault (Fischer et al. 1987; Vedder et al. 1986). The maximum magnitude and slip rate cannot be estimated due to absence of data. The fault is considered to be predominantly a strike-slip fault due to its association with the Palos Verdes fault but may also have a normal component of displacement. The fault could produce earthquakes with a magnitude of 6.25 to 6.5. Fischer et al. (1987) estimated a vertical slip rate of 0.4 to 0.7 mm/yr. Ward and Valensise (1994) suggested that the Cabrillo fault is a minor feature and has a slip rate of 0.1 mm/yr, which seems to be a better approximation.

The Sierra Madre fault is one of the major faults in the Los Angeles region and lies along the southern margin of the San Gabriel Mountains forming geomorphic features in the Los Angeles

area. The fault is primarily a thrust fault that has pushed the ancient igneous and metamorphic rocks of the San Gabriel Mountains up and over young Quaternary-age alluvial deposits. The Sierra Madre fault is capable of producing earthquakes in the 7.0 to 7.5 magnitude range (Dolan et al. 1995). About 20 km of the westernmost part of the Sierra Madre fault ruptured the ground surface during the 1971 San Fernando earthquake that had a magnitude (Mw) of 6.7. Geological studies of the 1971 rupture (Bonilla 1973) suggested that a previous rupture had occurred on this fault within the prior few hundred years. Recent paleoseismological studies (Rubin et al. 1998) suggested an average slip rate of only 0.6 mm/yr and the California Geological Survey used a slip rate of 2.0 mm/yr ±1.0 mm.

One of the main fault systems in the Los Angeles basin is along the southern edge of the Santa Monica Mountains separating Mesozoic plutonic rocks from Tertiary and Quaternary sedimentary rocks. The fault system consists of the Santa Monica and Hollywood faults and smaller segments such as the Malibu Coast and Potrero faults as previously shown in **Fig. 26**. Continuation of the fault to the west of Santa Monica is uncertain. Earthquake focal mechanisms and local geologic relationships suggested reverse faulting with a subordinate left-lateral component. The Santa Monica and Hollywood faults have been considered to comprise the major thrust fault that is responsible for uplift of the Santa Monica Mountains. However, other researchers have hypothesized that these faults are predominantly strike-slip features and that the mountains are underlain by a separate blind thrust fault. The California Geological Survey (2003) assumes a slip rate up to about 1.0 mm/yr ± 0.5 mm. The great length of the fault system suggests that it is capable of generating a large earthquake of a magnitude of 7.5 but the discontinuous nature of faulting suggests that faults may behave independently and perhaps a smaller maximum earthquake is more appropriate.

The San Pedro fault trends southeasterly from near the base of the Malibu-Santa Monica shelf to about Avalon Knoll east of Catalina Island, a distance of about 70 to 80 km. The fault is shown as a complicated association of folds. Southeast of the Palos Verdes Peninsula, this fault coincides with the western limit of a dense distribution of small magnitude Mw 3 to 5 earthquakes. The slip rate is unknown but the similarity of geomorphology, structures and length to the NISZ suggest that they are similar features and therefore could have similar slip rates of about 1 mm/yr and similar maximum earthquakes. Fault-length/earthquake-magnitude relationships (Wells and Coppersmith 1994) indicate a maximum earthquake of about M 7.0 to 7.2 but the feature is highly segmented indicating smaller magnitudes like M 6.5 to 7.0 are a best estimation.

The Elysian Park Fold and Thrust Belt (EPFT) was studied by Shaw and Suppe (1996) who suggested a slip rate of 1.7±0.4 mm/yr. This source is capable to generate earthquake magnitudes ranging from 6.6 to 7.3 depending on the size of the individual segments and whether the rupture occurs independently or together. Oskin et al. (2000) modeled the Upper Elysian Park thrust as extending from the Hollywood fault to the Alhambra Wash fault with a slip rate of 0.8 to 2.2 mm/yr and magnitude 6.2 to 6.7 earthquakes with recurrence interval in the range of 500 to 1300 years. The California Geological Survey suggested that the Upper Elysian Park thrust presents a slip rate of about 1.3±0.4 mm/yr.

The Puente Hills Thrust fault system (PHT) is the name currently given to a series of northerly dipping subsurface thrust faults (blind thrusts) extending about 40 to 45 km along the eastern margin of the Los Angeles Basin. Those faults form an arrangement from the northern Los Angeles Basin to the southern part of the Puente Hills as shown in **Fig. 26**. Shaw and Shearer (1999) found that the Puente Hills fault system was capable of generating earthquake magnitudes of about 6.5 to 7.0 and had a slip rate between 0.5 to 2.0 mm/yr. It is believed that the Whittier Narrows earthquake had occurred on this system. A prominent active fault of about the same age with abundant surface manifestations such as surface faulting and uplifted hills and mesas as well as abundant historical earthquake activity. The most recent seismic hazard model by the California Geological Survey (2003) used a slip rate of 0.7 ± 0.4 mm/yr.

The THUMS-Huntington Beach (THB) fault was described by Wright (1991) and Truex (1974) as a southeast-trending fault extending offshore from the Palos Verdes fault in the Los Angeles Harbor area along the southwest flank of the Wilmington Anticline, past the Huntington Beach oil field to the Newport Beach area where it converges with the Newport-Inglewood Structural Zone. Edwards et al. (2001, 2002, 2003) indicated that the THB fault has been active in Quaternary time (i.e., the past 400,000 to 600,000 years) and that the fault is capable of generating large-magnitude earthquakes with recurrence intervals on the order of a thousand to several thousand years (Ponti 2004).

The Compton-Los Alamitos (CLA) trends with several kilometers wide and dips downward at low angles to the northeast and extends from the Central Basin detachment to the Torrance-Wilmington trend where it becomes a horizontal detachment fault. Folded Pliocene and Quaternary strata indicate slip rates of 1.4 mm/yr. Shaw and Suppe (1996) estimated earthquake magnitudes of 6.3

to 6.8 earthquakes on individual ramp segments and magnitude 6.9 to 7.3 earthquakes whether segments rupture together. Wells and Coppersmith (1994) estimated earthquake recurrence intervals ranging from 380 years for single segments to 1,300 years for multiple segment ruptures.

The Los Alamitos fault is a northwest-southeast trending subsurface fault along the northeast side of the NISZ as previously shown in **Fig. 26**. This fault is not exposed at the surface. The fault extends upward from the basement rocks to an elevation of about -90 m and is subparallel to the NISZ from at least Seal Beach to Rosecrans. The Los Angeles County Seismic Safety Element (1990) related that this fault is potentially active and is capable to generate a maximum earthquake magnitude of 6.0. The northeastern limit of these events is almost linear and earthquake focal mechanisms indicate both normal and right-lateral strike-slip motions. Although there is no documented surface faulting or even late-Quaternary displacement, the fault ought to be considered as a potential source of small to moderate magnitude earthquakes, similar to other buried faults in the Los Angeles Basin. Earthquake magnitudes of 6.0 to 6.5 are appropriate for the maximum earthquake based on the fault's length according to the empirical fault-length/earthquake-magnitude relationships of Wells and Coppersmith (1994). A slip rate of 0.5 mm/yr had been assumed for this fault.

3.3 Regional Seismicity of the POLB area

The southern California area has been historically seismically active as shown in the seismicity map presented in **Fig. 30** for a radius of 300 km around the POLB. At least 189 earthquakes were registered from year 1800 until present. Each circle represents an earthquake event with magnitude Mw greater than 5.0. This figure shows the focal mechanisms for the earthquakes, however the seismic activity does not clearly correlate or coincide with the location of the surface faults. Ward (1994) suggested that as much as 40% of the tectonic activity in southern California is not released on known faults.

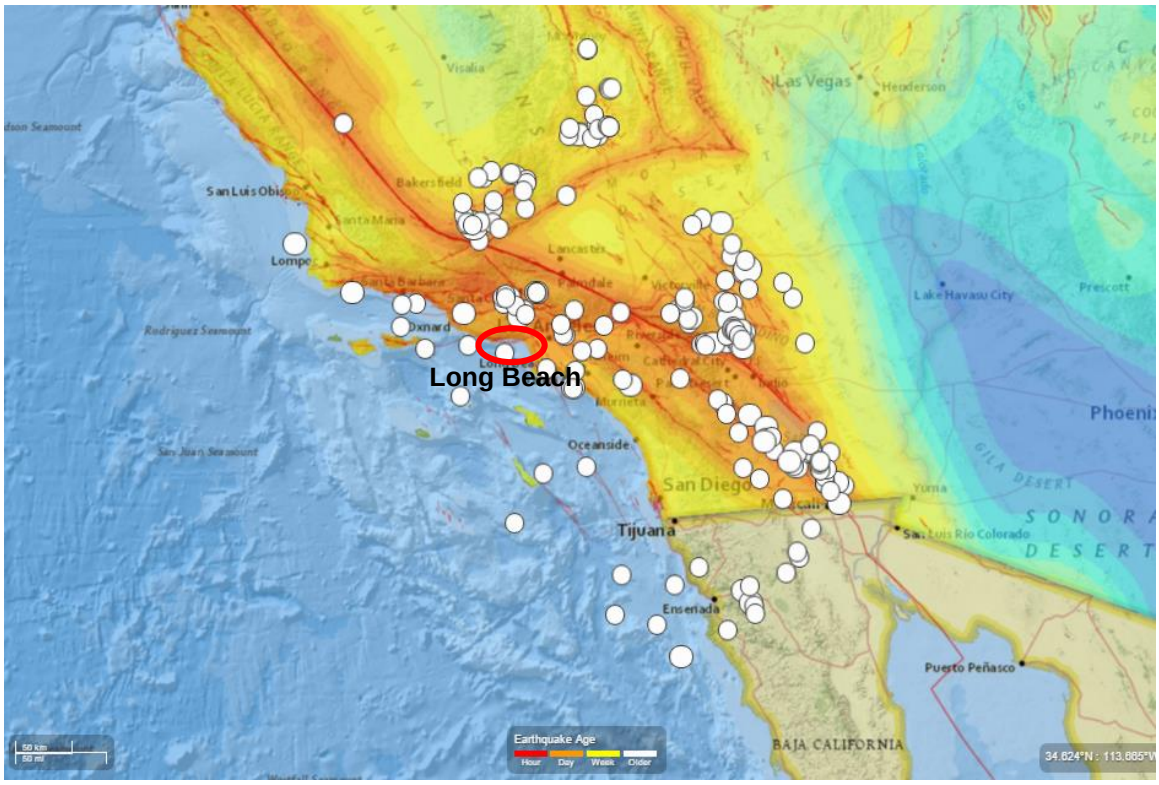

Fig. 30. Historic records of seismic activity starting from year 1800 for the POLB area within a radius of 300 km (after USGS 2016).

The largest historical earthquake within the Los Angeles basin area was the 1933 Long Beach earthquake with a magnitude Mw 6.4. Other seismic events outside of the basin area were the 1971 San Fernando earthquake with a magnitude (Mw) of 6.7, the 1987 Whittier earthquake with an Mw of 5.9 and the Northridge earthquake with an Mw of 6.7. One of the largest earthquakes within a radius of 300 km occurred in 1952 in the Grapevine area located 122 km from Los Angeles. A moment magnitude of 7.5 was registered.

Hauksson (1987, 1990) analyzed the historical seismicity of Los Angeles basin identifying that: i) the majority of the strike-slip events were caused along the NISZ, ii) the reverse mechanisms occurred mostly to the north of Palos Verdes Hills, and iii) the normal fault mechanisms occurred in the offshore area and along the NISZ. Most of the earthquakes that occur in the geologic structures of the Los Angeles Basin are characterized by the tectonic environment grouped in three regimes: a contractional tectonic regime, a mixture of contractional and transcurrent structures, and a transcurrent regime like strike-slip faults. However, most earthquakes in the area occur within the same basic compressional tectonic regime and serve as the base of numerous seismic hazard

analyses. This is because earthquakes are likely to occur on the subsurface faults in the area of Los Angeles.

The main sources of seismic activity at the POLB are shown in **Table 2**. The Palos Verdes and the Newport-Inglewood are the most important geologic faults that would potentially cause earthquakes in the POLB area. The table summarizes the seismic source parameters for the local faults and their behavior in terms of the slip rate, depth, style of faulting (i.e., strike-slip or reverse), and mean characteristic earthquakes associated with each source.

Table 2. Summary of seismic source parameters for local faults of POLB (After Earth Mechanics Inc. 2006).

Fault (Map Abbreviation)	Depth to Top of Fault (km)	Depth to Bottom of Fault (km)	Dip (deg)	Slip Rate (mm/yr)	Mean Characteristic Earthquake, Mw	Style of Faulting
Palos Verdes (PV-PVH, PV-SO)	0	11 to 18	90	2.0 to 4.0	6.65 to 7.2	Strike-Slip
Newport-Inglewood (NI)	0	13 to 16	90	0.5 to 1.5	6.7 to 7.2	Strike-Slip
Cabrillo (CAB)	0	15 to 18	70	0.1	6.25 to 6.5	Strike-Slip
San Pedro Basin (SPB)	0	15	90	0.5 to 1.0	7.1 to 7.2	Strike-Slip
Los Alamitos (LAL)	0	15	70	0.25 to 0.5	6.5	Strike-Slip
Compton Thrust (CT)	0	10	16	0.5 to 1.0	7.1 to 7.2	Reverse

Based on the report by Earth Mechanics Inc. (2006), the earthquake level hazards for the POLB are classified in two: The Operating-Level Earthquake (OLE) and Contingency-Level Earthquake (CLE) with 72 and 475-year return periods, respectively. These earthquake events were identified as having a 50% and 10% probability of exceedance in 50 years, respectively. Such probability was determined from a location within Pier T, adjacent to Pier S, which is the subject of study of this research. A comparison of the seismic hazard at other sites lead to larger ground motions than at other locations in the port area, particularly for the CLE seismic events, as opposed to the OLE event which remained basically unchanged regardless of the location along the port.

The POLB wide ground motion report recommends a peak ground acceleration (PGA) for geotechnical evaluations for the OLE of 0.21g with a dominant source corresponding to an

earthquake magnitude of 6.5 at a distance of 20 km. The PGA for the CLE earthquake is 0.5g with the dominant source of magnitude 7.0 at a distance of 4 km. The mean hazard for different seismic sources at the POLB is shown in **Fig. 31**. It is evident that the Palos Verdes fault represents the largest seismic hazard at the POLB. The study concludes that the Palos Verdes and the Newport Inglewood faults, represent the dominant seismic hazards at various locations of the POLB, particularly for the CLE case. Some other distant faults can be ignored. Also, the POLB soil conditions differ from other ports like the Port of Oakland or Port of Los Angeles, in the fact that extremely large site amplification effects do not seem plausible for the alluvial deposit geologic environment at the POLB. Site response analyses for the ground conditions present at the POLB, should lead to site amplification effects no higher than about 35%.

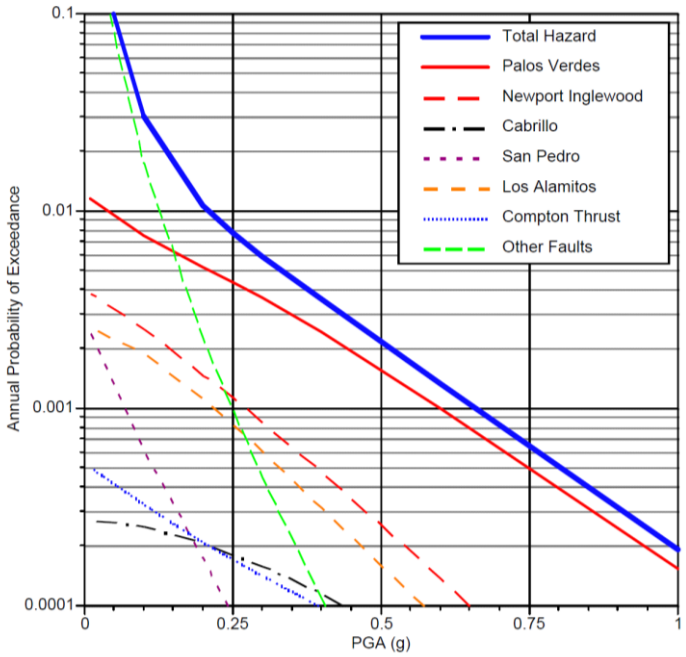

Fig. 31. Peak ground acceleration hazard for different sources (Earth Mechanics Inc. 2006).

Also, the POLB wide ground motion report recommends seven sets of firm-ground time histories for the OLE condition with a magnitude ranging from 6 to 7 generated from a near to moderate distance events. **Table 3** provides the recommended station of measurement based on the distance required to simulate short and medium predominant periods for the OLE condition. Similar information is presented in **Table 4** but for the CLE condition in which magnitudes vary between 6.5 and 7.5 and the station distances between 0 and 10 km for earthquakes with short predominant periods.

Table 3. Representative earthquakes for the OLE condition (After Earth Mechanics Inc. 2006).

Set	Earthquake	Magnitude	Station	Distance (km)
1	1989 Loma Prieta	6.9	Saratoga - Aloha Ave.	13
2	1987 Superstition Hill	6.3	Wildlife Liquefaction Array	24.7
3	1987 Whittier	6.0	Northridge-Saticoy St	39.8
4	1979 Imperial Valley	6.5	EC CO Center FF	7.6
5	1979 Imperial Valley	6.5	Calexico Fire Station	10.6
6	1992 Erzikan	6.9	Erzikan	2
7	1994 Northridge	6.7	Century City, LACC	25.7

Table 4. Representative earthquakes for the CLE condition (After Earth Mechanics Inc. 2006).

Set	Earthquake	Magnitude	Station	Distance (km)
1	1999 Hector mine	7.1	Hector	12
2	1989 Loma Prieta	6.9	Gilroy 03	13
3	1979 Imperial Valley	6.5	Brawley	10
4	1999 Duzce	7.1	Lamont 1059	4
5	1992 Erzikan	6.7	Erzikan	4
6	1940 Imperial Valley	7.0	El Centro	6
7	1995 Kobe	6.9	Kobe University	1

Fig. 32 shows the suggested horizontal and vertical firm-ground uniform hazard spectra with 5% damping for the OLE and CLE level earthquakes, which correspond to a 72-yr and a 475-yr return periods, respectively.

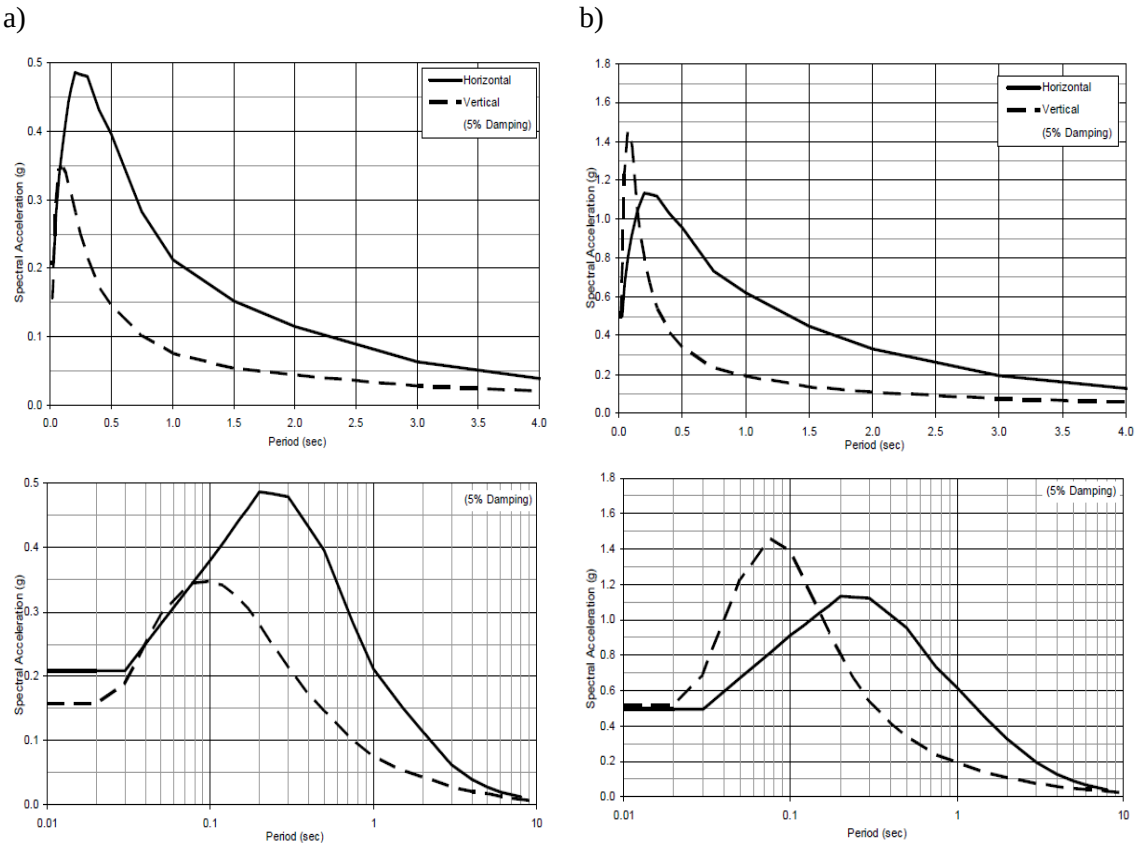

Fig. 32. Recommended firm-ground spectra for: a) OLE and b) CLE conditions with 5% damping (Earth Mechanics Inc. 2006).

3.4 Subsurface conditions at the POLB, Pier S

The POLB has been constructed on top of natural coastal and man-made land masses creating wide variations of ground conditions along the port area. Historically, some of the dredged materials have been used for the construction of man-made land masses currently present at the port. **Fig. 33** presents a plan view of the port area which is divided into four areas denoted as Zones I, II, III, and IV as suggested in the port-wide ground motion study at the POLB. Information regarding subsurface field testing has been provided by the port for Pier S, located within Zone IV. The results of field testing corresponding to Standard Penetration Tests (SPT), Cone Penetration Tests (CPT) and shear wave velocity soundings were provided. **Fig. 34** shows shear wave velocities inferred from other sources of ground investigation like the ROSRINE database (ROSRINE 2001) where geophysical testing was performed using Seismic Analysis of Surface Wave (SASW) methods. The results are presented up to a depth of 30 m, which is defined as firm-ground conditions for Zone IV.

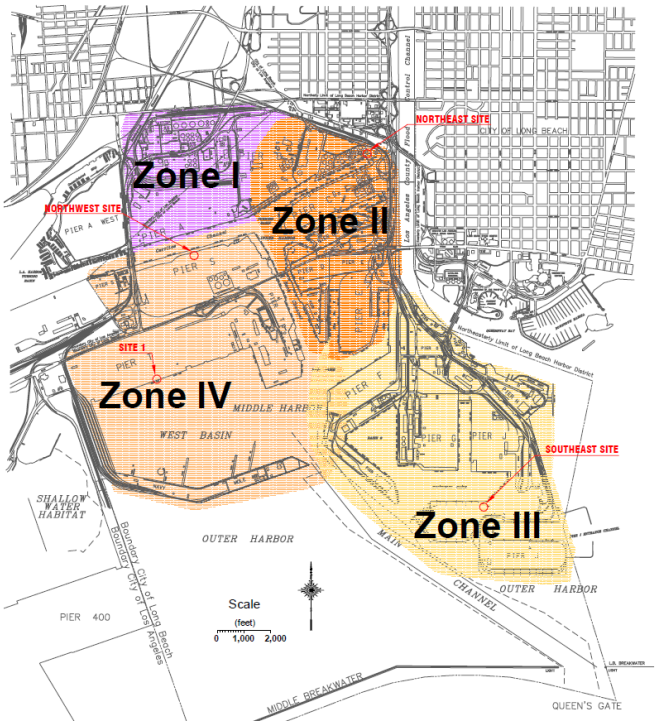

Fig. 33. Plan view of the POLB area divided in four characteristic subsurface conditions (Zones defined by Earth Mechanics Inc. 2006).

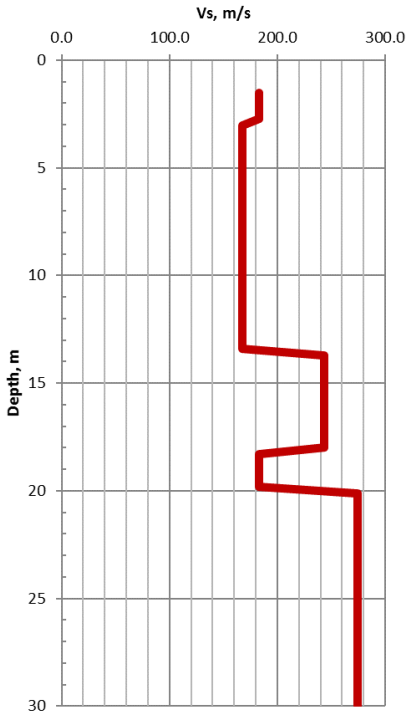

Fig. 34. Results of shear wave velocities for Pier S located within Zone IV (After Earth Mechanics Inc. 2006).

The predominant frequency of the subsurface conditions at Pier S can be calculated with the following equation:

$$f = \frac{V_{S\,30}}{4H} \tag{35}$$

where $V_{S\,30}$ corresponds to the average shear wave velocity measured through the first 30 m below the ground surface and H (= 30 m) is the thickness of the soil layer. For Pier S, using a $V_{S\,30}$ equal to 208 m/s, the predominant frequency is equal to 1.73 Hz (or a period of 0.58 s).

Fig. 35 shows the location of Pier S in the Port of Long Beach. The subsurface conditions of the site were investigated using CPT and SPT soundings. Three SPT and ten CPT soundings labeled B101, B102, and B103 and C-101 through C-110, respectively, were performed at the approximate locations shown in the figure. The three SPT borings were drilled by the rotary wash method with a borehole diameter of 150 mm and extended up to 40 m below ground level. Six of the CPT soundings (C-101 through C-106A) were performed to depths ranging from 37.2 to 38.4 meters below the existing ground surface and the remaining four CPT's (C-107 through C-110) were performed to a depth of 15.2 meters. All the CPT's were advanced taking measurements of the cone tip and side friction resistance.

Fig. 35. Approximate location of CPT and SPT soundings (After Geotechnical Professionals Inc. 2003).

Fig. 36 presents the results of the field exploration program and shows the summarized soil profile for Pier S. The SPT blow counts were corrected for energy ratio, borehole diameter, sampling method, rod length, and overburden pressure to obtain the $(N_1)_{60}$ values. The definition of the soil profile for the POLB, Pier S was based on the records presented in **Fig. 36**, supplemental geotechnical laboratory tests, and the geological information of the area. **Fig. 37** summarizes the results of index laboratory tests including primary classification based on the USCS, content of fines, water content, relative density, and total and dry densities.

The subsurface soil conditions in Unit A consists mostly of man-made compacted fills composed of silty to clayey sands borrowed from off-site sources. The SPT and CPT data are scattered probably due to the presence of some weak and uncompacted soils. It was suggested by Earth Mechanics Inc. (2006) that older fills are generally weaker than the engineered fills. Even though there is not documentation about the extent of the man-made fills, based on the field test results an approximate thickness of 7.5 m from the ground surface is estimated. The CPT tip resistance in this layer ranges from 2 to 40 MPa and SPT N-values range from 4 to 50 blows/feet. The results indicate variations of relative densities between 20 and 90% and the existence of some weak thin layers within well compacted fills. The natural water content of Unit A is between 10 and 30%, increasing through depth, and its total unit weight varies between 19 and 21 kN/m^3, supporting the hypothesis that this man-made fills are not well compacted. Based on the results of laboratory testing, an effective friction angle, $\emptyset' = 34°$ was selected for this man-made fill. Based on Kulhawy and Mayne (1990), this value appears to be acceptable for medium to dense granular soils.

Unit A overlies an upper layer of marine-estuarine sediments (Unit B). This layer is primarily composed of high compressible and cohesionless soils like silty fine sands with thin layers of silty soils. Unit B has a thickness of about 10.5 m extending from the bottom of the man-made fills to elevation -15 m Mean Lower Low Water (MLLW). The CPT tip resistance in this layer ranges from 1 to 10 MPa, while SPT N-values vary between 1 and 12 blows/feet. Both test results show random peak values due to the presence of some coarse granular materials typically found on natural sedimentary deposits. Based on CPT and SPT results, an average relative density of 40% was estimated indicating Unit B is a loose stratum. Natural water contents range from 30 to 50% and total unit weights between 17 and 19 kN/m^3. For this layer an effective friction angle of 34°

was chosen based on the results of laboratory tests. Based on Kulhawy and Mayne (1990), this value is within limits of other loose granular deposits ($28° \leq \emptyset' \leq 35°$). The large water content values found on this layer indicate the soils are not fully consolidated under the present stress conditions.

The transition between Unit A and B is marked by changes in their relative density. The upper deposits are more prone to liquefaction than the deeper soils. This is because of the large relative density of deeper deposits which reduces their liquefaction potential. It is evident the increase in resistance of soils with depth as coarse sandy soils are present in the subsurface conditions. These coarse granular non-plastic materials tend to have large permeability, which prevents liquefaction. Unit C is a dense lower marine/estuarine deposit extending from elevations -15 to -24.5 m MLLW. It is composed of dense silty sands with thin layers of very stiff to hard silts. This layer has a medium to dense compactness as seen from CPT tip resistances and SPT N-values which are scattered likely due to the presence of some gravels. The total unit weight varies from 18 to 19 kN/m^3 while natural water contents range between 18 to 30% decreasing with depth and showing the presence of lightly overconsolidated cohesive soils. This layer has an effective friction angle of 30°.

Unit D is the Gaspur Formation extending from -24.5 to -34 m MLLW. It is composed of very dense medium to coarse grained sands with interbedded fine gravels. The high compactness of this layer is evidenced by SPT N-values that increase with depth ranging from 20 to 50 blows/feet and CPT tip resistances from 10 to 40 MPa. Relative densities larger than 80% are estimated and a peak effective friction angle of 38° is selected based on reference values reported by Kulhawy and Mayne (1990) for dense granular deposits.

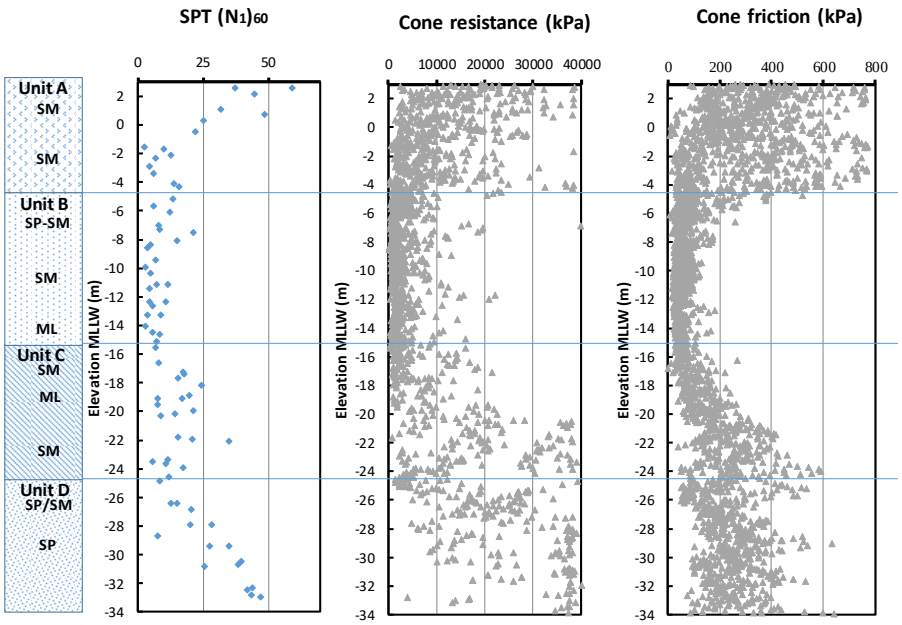

Fig. 36. Summary of the field testing program for Pier S located within Zone IV (After Geotechnical Professionals Inc. 2003).

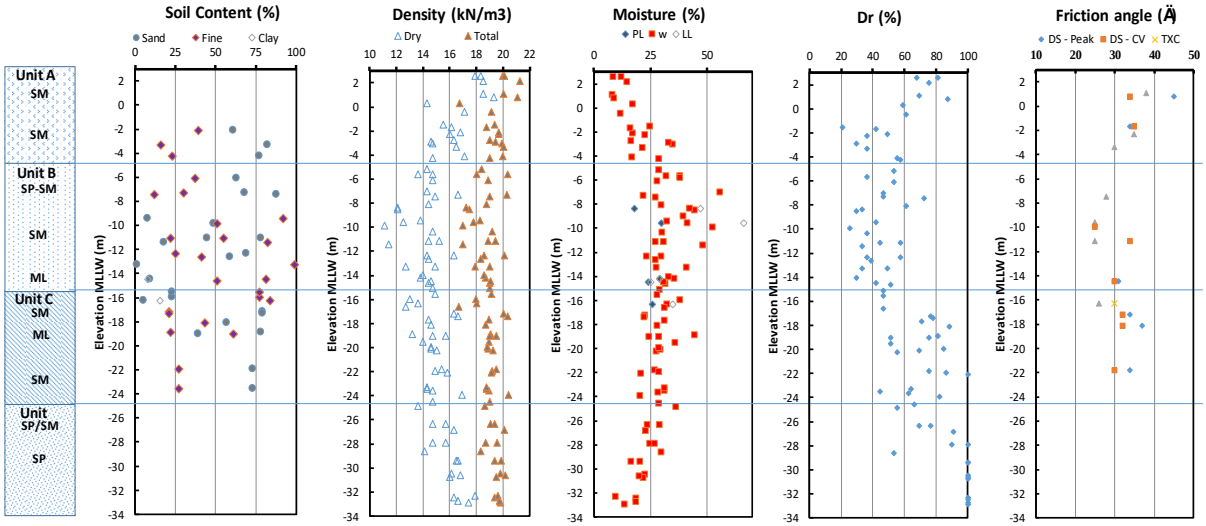

Fig. 37. Summary of the geotechnical laboratory testing program for Pier S located within Zone IV (After Geotechnical Professionals Inc. 2003).

Fig. 38 shows the computed summarized values of soil resistance based on the subsurface investigation testing program and used in this research for the evaluation of the liquefaction susceptibility of the site. The average groundwater elevation was estimated from the field tests as

1.8 m MLLW. The groundwater condition at the site varies as a result of tidal fluctuations, therefore the reported water level cannot be interpreted as a permanent condition. The computed average values from SPTs and CPTs show similar trends in the behavior of the different soil layers. These values were statistically obtained as prorated average values after removing measured points larger than 9 times the standard deviation and lower than 28 times the standard deviation calculated for the most part with values up to 12,000 kPa for the CPT tip resistance and up to 26 for the SPT blowcount, which were selected as reference values characteristic of sandy soils.

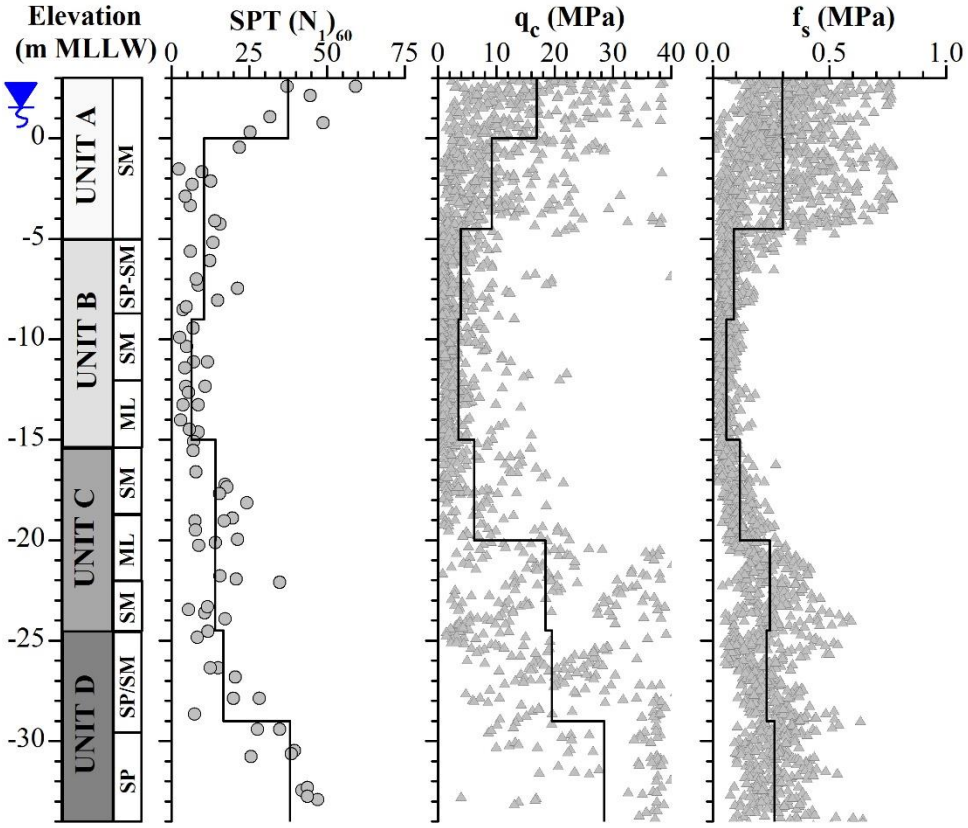

Fig. 38. Computed variations of soil resistance using the results of SPTs and CPTs.

4. SEMI-EMPIRICAL EVALUATION OF THE PORT OF LONG BEACH

4.1 Liquefaction of Port of Long Beach

Based on the geotechnical investigation developed on Pier S of the Port of Long Beach, POLB (2003), the site under study was filled in the 1920's with dredged material in an uncontrolled manner not following any soil specification. These hydraulic fills typically consisted of fine to medium grained sands that are loose and susceptible to liquefaction during an earthquake. In 2000 and 2001, an engineered fill, with a minimum relative compaction of 85%, was placed to raise the surface grade in backland areas. These man-made fills, called Unit A herein, are located on top of marine/estuarine sediments (Unit B) that were also found to be loose sand deposits.

The geotechnical engineering report provided by the port for the development of this project classifies Unit B and some thin layers of Unit C (lower estuarine or marine deposits) as potentially liquefiable material. Their evaluations, based on the simplified procedures presented by NCEER (1997), indicated that most cohesionless soils resist liquefaction under the Operating Level Earthquake (OLE) conditions. However, a few thin soil layers and specifically Unit B would be susceptible to liquefaction under larger magnitude earthquakes characteristic of the Contingency Level Earthquake (CLE) condition. Underlying Unit C very dense granular deposits geologically known as the Gaspur Formation are found. This formation predominantly consists of medium to coarse grained sands with some fine gravels that have high liquefaction resistance.

The California Department of Conservation (1999) developed seismic hazard zones of the city of Long Beach as shown in **Fig. 39**. The figure shows in green the areas of historic occurrence of liquefaction or higher potential for liquefaction-induced permanent deformations. It is shown that for the most part the POLB area is susceptible to liquefaction.

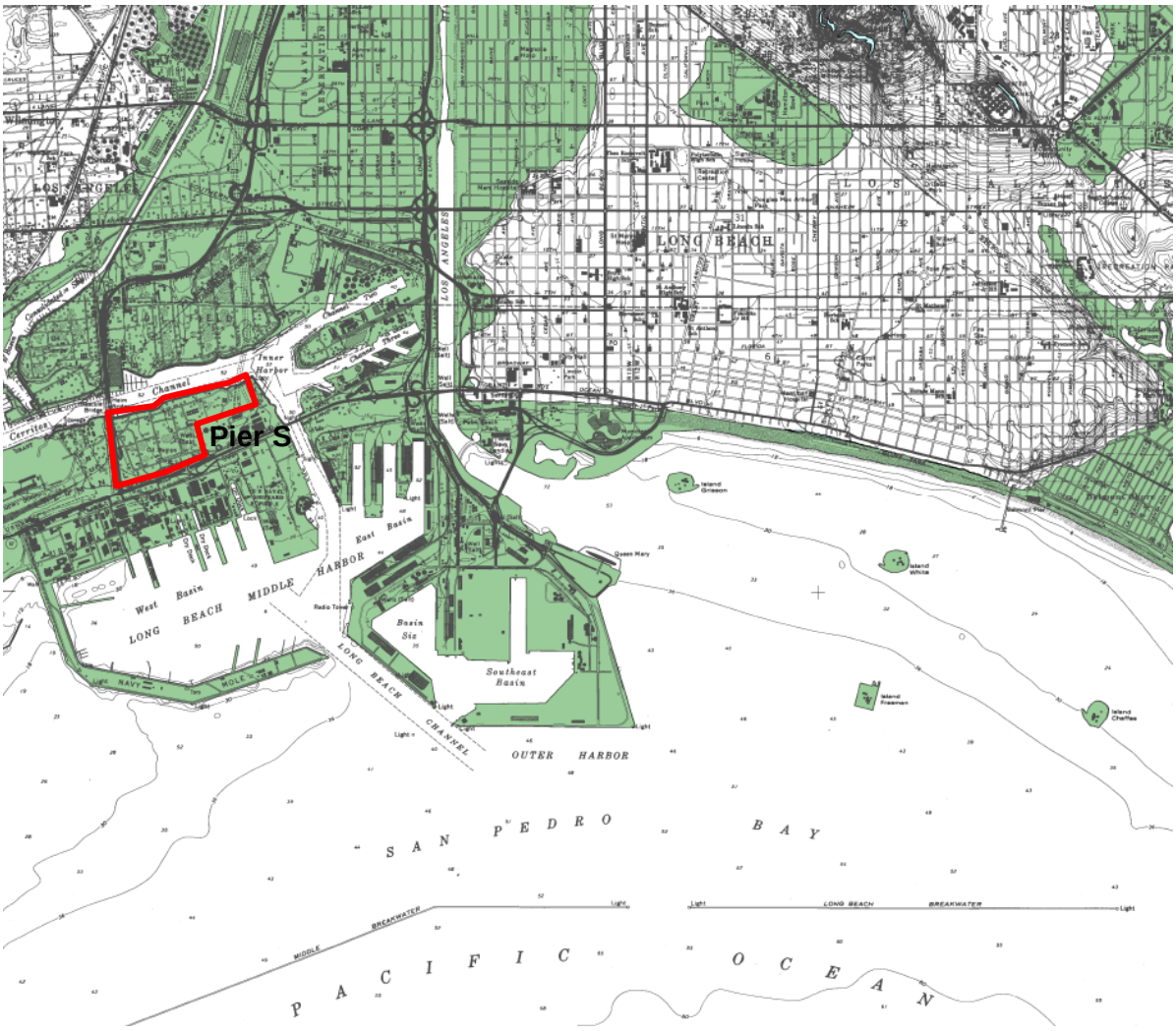

Fig. 39. Liquefaction hazard zones in green (California Department of Conservation 1999).

4.2 Evaluation of the Liquefaction Susceptibility using Standard Penetration Tests (SPTs)

Using the results of the SPT blow counts shown in **Fig. 36** and their computed average presented in **Fig. 38**, the evaluation of the liquefaction susceptibility was made using the semi-empirical method explained in Section 2.1.1. The SPT blow counts were corrected for energy ratio, borehole diameter, sampling method, rod length, and overburden pressure. The $(N_1)_{60}$ values had been corrected to equivalent clean sand values, $(N_1)_{60,cs}$. **Table 5** and **Table 6** show the parameters to calculate the factor of safety against liquefaction. From the calculation, it is concluded that Unit B is a liquefiable soil for both OLE and CLE conditions. The FS against liquefaction for Unit A for both earthquake levels is not shown because the $(N_1)_{60,cs}$ average value is larger than 30 and thus,

liquefaction does not occur (Youd et al. 2001). The Cyclic Stress Ratio (CSR) values were calculated using Eqs. (2) and (3) for earthquake magnitudes of 6.5 and 7.0 corresponding to the OLE and CLE earthquake levels with peak ground acceleration (PGA) of 0.21 and 0.5 g, respectively. In addition, calculations of the Cyclic Resistance Ratio normalized for a magnitude 7.5 earthquake ($CRR_{7.5}$) and a Magnitude Scaling Factor (MSF) were performed to determine appropriate values of CRR for the proposed earthquake levels.

Table 5. Computed factors of safety for the OLE condition with the SPT method.

Unit	C_N	E_m/E_{ff}	N_{60}	$(N_1)_{60}$	r_d	$(CSR)_{field}$	MSF	FC (%)	α	β	$(N_1)_{60\,cs}$	$CRR_{7.5}$	CRR	FS_L
A	1.31	0.60	39	51.23	0.98	0.18	1.44	26.00	4.39	1.12	61.90	-	-	-
B	1.02	0.60	8	8.16	0.94	0.21	1.44	20.00	3.61	1.08	12.42	0.13	0.19	0.92
C	0.60	0.60	30	17.98	0.56	0.14	1.44	46.00	5.00	1.20	26.57	0.31	0.45	3.10
D	0.48	0.60	45	21.52	0.50	0.13	1.44	27.00	4.48	1.13	28.81	0.37	0.53	4.05

Table 6. Computed factors of safety for CLE condition with the SPT method.

Unit	C_N	E_m/E_{ff}	N_{60}	$(N_1)_{60}$	r_d	$(CSR)_{field}$	MSF	FC (%)	α	β	$(N_1)_{60\,cs}$	$CRR_{7.5}$	CRR	FS_L
A	1.31	0.60	39	51.23	0.98	0.42	1.19	26.00	4.39	1.12	61.90	-	-	-
B	1.02	0.60	8	8.16	0.94	0.50	1.19	20.00	3.61	1.08	12.42	0.13	0.16	0.32
C	0.60	0.60	30	17.98	0.56	0.34	1.19	46.00	5.00	1.20	26.57	0.31	0.37	1.08
D	0.48	0.60	45	21.52	0.50	0.31	1.19	27.00	4.48	1.13	28.81	0.37	0.44	1.41

Fig. 40 shows the factor of safety against liquefaction based on SPT field data for the OLE and CLE earthquake conditions. In the figure, values less than one indicate the presence of liquefiable soils. This figure shows that Unit B is susceptible to liquefaction whereas Unit A, C, and D have factors of safety larger than 1.0 for the OLE condition. Although the bottom of the Unit A has a FS less than one, this layer is not considered liquefiable. For the CLE condition, Unit B and the upper portion of Unit C are susceptible to liquefaction and the factor of safety against liquefaction is lower than the one evaluated for the OLE condition due to its higher PGA value and earthquake magnitude.

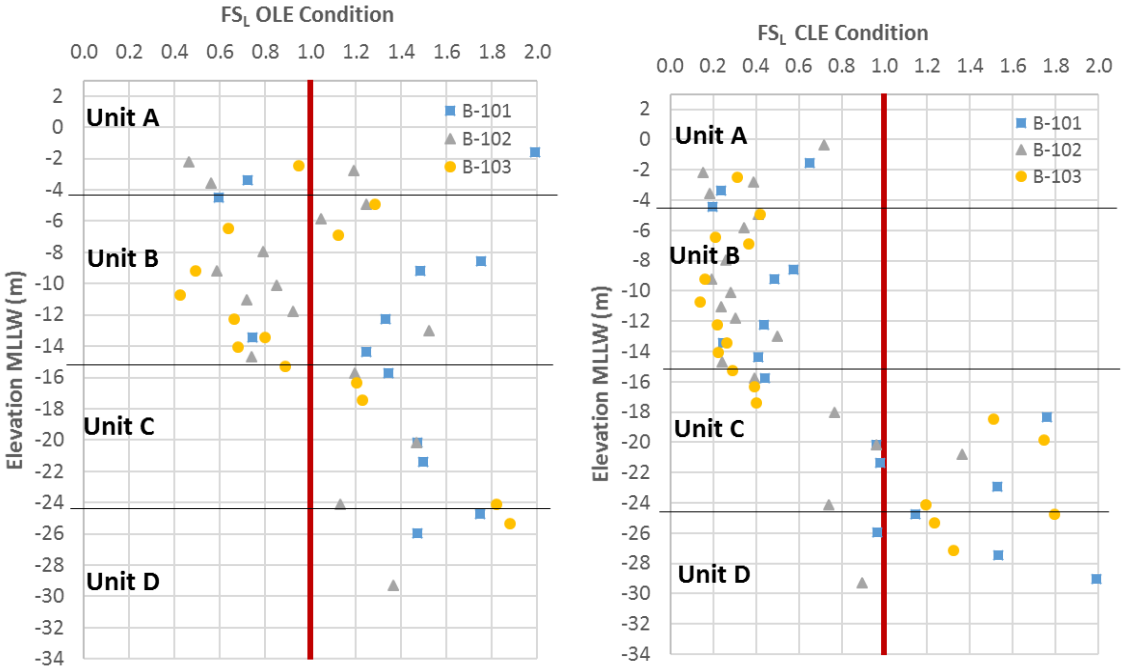

Fig. 40. Factor of safety to evaluate liquefaction susceptibility using SPT semi-empirical method for the OLE and CLE conditions.

Fig. 41 shows the CRR versus $(N_1)_{60}$ curve proposed by Seed et al. (1985) with different points representing the calculated CSR with the corresponding $(N_1)_{60}$ values for each layer in the POLB, Pier S. The figure shows that almost the entire Unit A lies below the CRR curve for the OLE earthquake magnitude, indicating that liquefaction is not reached. Although some points of Unit C are located above the CRR curve, it is considered that this unit is not a liquefiable layer because it is located at a larger depth with respect to the ground surface which implies large confinement due to large overburden pressures (i.e., at 19 m). Conversely, almost the entire Unit B is located above the CRR curve proposed by Seed et al. (1985), which implies a large susceptibility to initiate liquefaction under a seismic event corresponding to the OLE condition. The analysis of the liquefaction potential based on SPT semi-empirical approaches showed that deep soil deposits in the POLB Pier S are not susceptible to liquefaction during the earthquake levels presented here. Hence, only Unit B shown with closed symbols in **Fig. 41** is considered as the only potentially liquefiable soil for the two earthquake levels studied in this research.

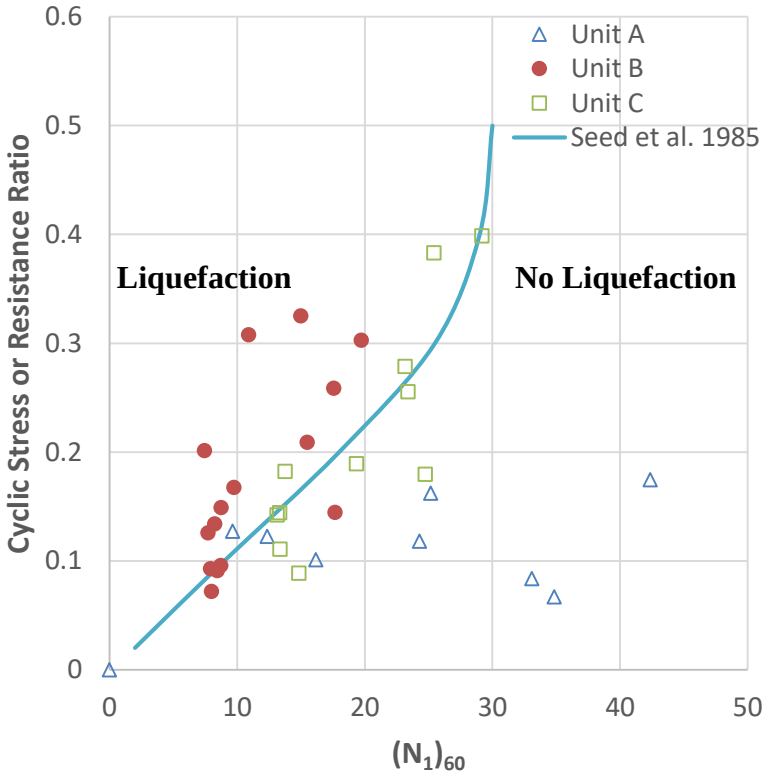

Fig. 41. SPT clean-sand base curve with data points plotted normalized to a magnitude 7.5.

4.3 Evaluation of the Liquefaction Susceptibility using Cone Penetration Tests (CPTs)

Using the CPT results shown in **Fig. 36** and the computed average values presented in **Fig. 38**, the evaluation of the liquefaction susceptibility was made using the semi-empirical method explained in Section 2.1.2. **Table 7** and **Table 8** list the calculated FS against liquefaction due to earthquake magnitudes 6.5 and 7.0. Factors of safety less than one were computed for Unit B, which shows again the large liquefaction potential of this soil layer under CLE and OLE conditions.

Table 7. Computed factors of safety for the OLE condition with the CPT method.

Unit	F (%)	Q	C_N	$(q_c)_1$ (MPa)	Ic	Kc	$(q_c)_{1cs}$ (MPa)	r_d	$(CSR)_{field}$	MSF	$CRR_{7.5}$	FS_L
A	3.29	149.55	1.64	15.05	2.17	1.59	23.93	0.96	0.132	1.44	1.084	11.8
B	0.92	36.97	1.13	3.86	2.24	1.77	6.83	0.89	0.159	1.44	0.099	0.89
C	1.34	110.41	0.61	11.31	1.96	1.25	14.17	0.66	0.132	1.44	0.276	3.02
D	0.93	140.33	0.50	14.34	1.78	1.09	15.66	0.52	0.105	1.44	0.340	4.66

Table 8. Computed factors of safety for the CLE condition with the CPT method.

Unit	F (%)	Q	C_N	$(q_c)_1$ (MPa)	Ic	Kc	$(q_c)_{1cs}$ (MPa)	r_d	$(CSR)_{field}$	MSF	$CRR_{7.5}$	FS_L
A	3.29	149.55	1.64	15.05	2.17	1.59	23.93	0.96	0.348	1.19	1.084	3.7
B	0.92	36.97	1.13	3.86	2.24	1.77	6.83	0.89	0.417	1.19	0.099	0.28
C	1.34	110.41	0.61	11.31	1.96	1.25	14.17	0.66	0.346	1.19	0.276	0.95
D	0.93	140.33	0.50	14.34	1.78	1.09	15.66	0.52	0.277	1.19	0.340	1.46

Fig. 42 shows the factor of safety against liquefaction for the OLE and CLE earthquake conditions. This figure suggests that for the OLE condition, Unit B and the upper portion of Unit C are susceptible to liquefaction, whereas Unit A and D have factors of safety larger than 1.0. For the CLE condition, Unit B, the lower portion of Unit A and the upper portion of Unit C are susceptible to liquefaction.

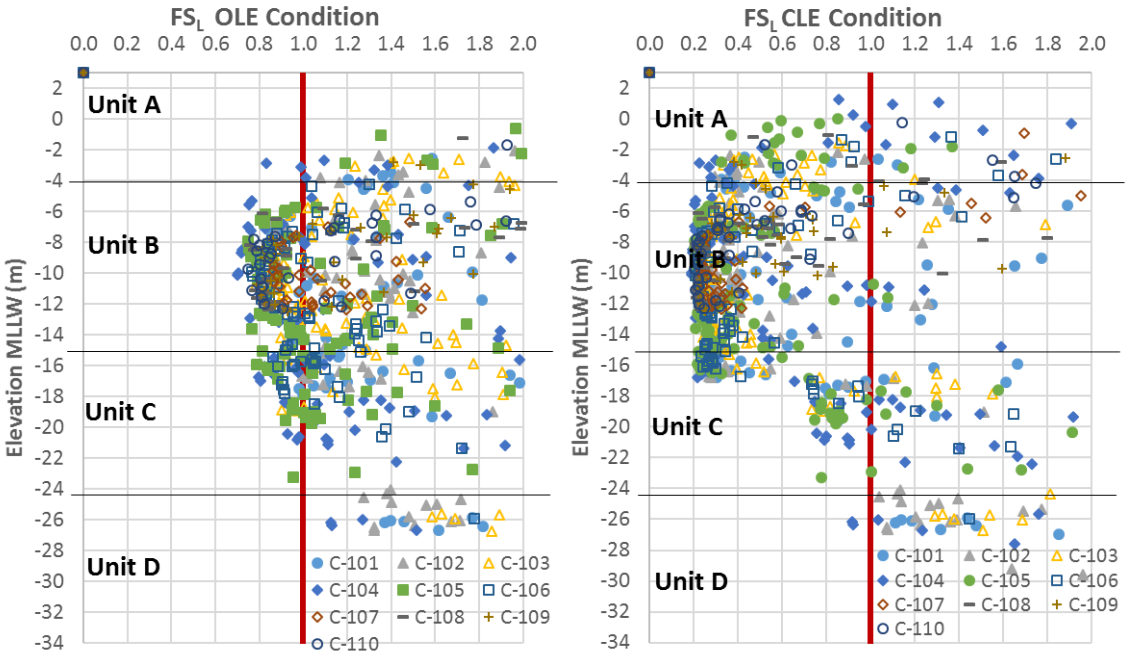

Fig. 42. Factor of safety to evaluate liquefaction susceptibility using CPT semi-empirical method for the OLE and CLE condition.

Fig. 43 shows summarized average data points of the Cyclic Resistance Ratio for the CPTs. In this figure, liquefaction occurs when the equivalent clean sand value (q_{c1N}) is less than 20. Only the average value computed for layer B plots slightly above the curve proposed by Robertson and Wride (1998). This result demonstrates the liquefaction potential of the soils present in this unit.

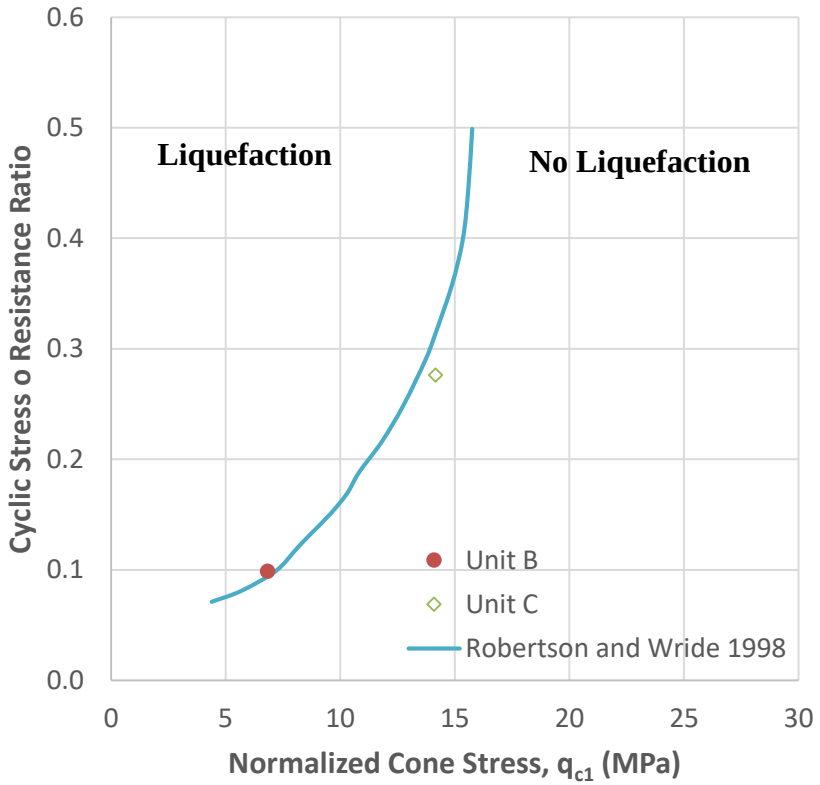

Fig. 43. Cyclic Resistance Ratio, CRR versus tip resistance, q_{c1N} with averaged data points.

The FS against liquefaction for Unit B based on CPT results is consistent to the FS calculated with the SPTs. This confirms that only Unit B (represented with closed symbols in the figure) is considered a potentially liquefiable soil under the two earthquake levels (OLE and CLE). Some points in the vicinity of Unit B (i.e., lower portion of Unit A and upper portion of Unit C) might suggest that those soils are liquefiable under the CLE condition.

4.4 Evaluation of the Liquefaction Susceptibility using Shear Wave Velocity (V_s)

The average shear wave velocity profile presented in **Fig. 34** was used to assess the liquefaction of soils following Section 2.1.3. **Table 9** and **Table 10** shows the calculated factor of safety against liquefaction which results in agreement with other triggering methods regarding the liquefaction potential of Unit B under the OLE and CLE conditions. The shear wave velocity values (V_s) were corrected for overburden pressure (V_{s1}). The V_{s1} for Unit A is larger than the maximum recommended value of 215 m/s as shown in **Fig. 12**, and therefore the factor of safety against liquefaction is not presented because liquefaction is not reached.

Table 9. Computed factors of safety for the OLE condition with V_s method.

Unit	V_s (m/s)	γ (kN/m^3)	V_{s1}	V_{s1}*	r_d	$(CSR)_{field}$	MSF	$CRR_{7.5}$	FS_L
A	180	19.5	221	215	0.96	0.132	1.44	-	-
B	160	18.1	169	215	0.89	0.159	1.44	0.110	0.99
C	250	19.1	204	215	0.66	0.132	1.44	0.336	3.67
D	280	19.7	210	215	0.52	0.105	1.44	0.683	9.36

Table 10. Computed factors of safety for the CLE condition with V_s method.

Unit	V_s (m/s)	γ (kN/m^3)	V_{s1}	V_{s1}*	r_d	$(CSR)_{field}$	MSF	$CRR_{7.5}$	FS_L
A	180	19.5	221	215	0.96	0.348	1.19	-	-
B	160	18.1	169	215	0.89	0.417	1.19	0.110	0.31
C	250	19.1	204	215	0.66	0.346	1.19	0.336	1.16
D	280	19.7	210	215	0.52	0.277	1.19	0.683	2.95

The results obtained with this method also show the same tendency about the liquefaction potential of Unit B under the OLE and CLE levels. Factors of safety larger than 1.0 were computed for Units A, C, and D. After the assessment of liquefaction susceptibility using semi-empirical procedures based on SPTs, CPTs, and measurements of V_s, it is concluded that Unit B is the only layer susceptible to liquefaction in the POLB, Pier S.

4.5 Settlement Evaluation due to Liquefaction in the POLB

In order to provide recommendations regarding the resulting permanent ground deformations, which could compromise the regular operation and resiliency of the port needed after an earthquake event, settlements were calculated based on classical semi-empirical methods which were briefly described in section 2.2. These methods were derived from previous case histories mostly for free-field conditions and are based on the computation of the volumetric strains resulting from the earthquake that integrated over the depth can be used to compute ground settlement.

Using the semi-empirical methods proposed by Tokimatsu and Seed (1986) and Ishihara and Yoshimine (1992), settlements were evaluated for the free-field condition using the software LiquefyPro for both OLE and CLE levels. **Fig. 44** shows the relative density, layer thicknesses, and factors of safety against liquefaction summarized for each Unit which are required input values to

compute settlements with both approaches. These values are averages computed with the results of SPTs and CPTs, as shown in **Fig. 38**.

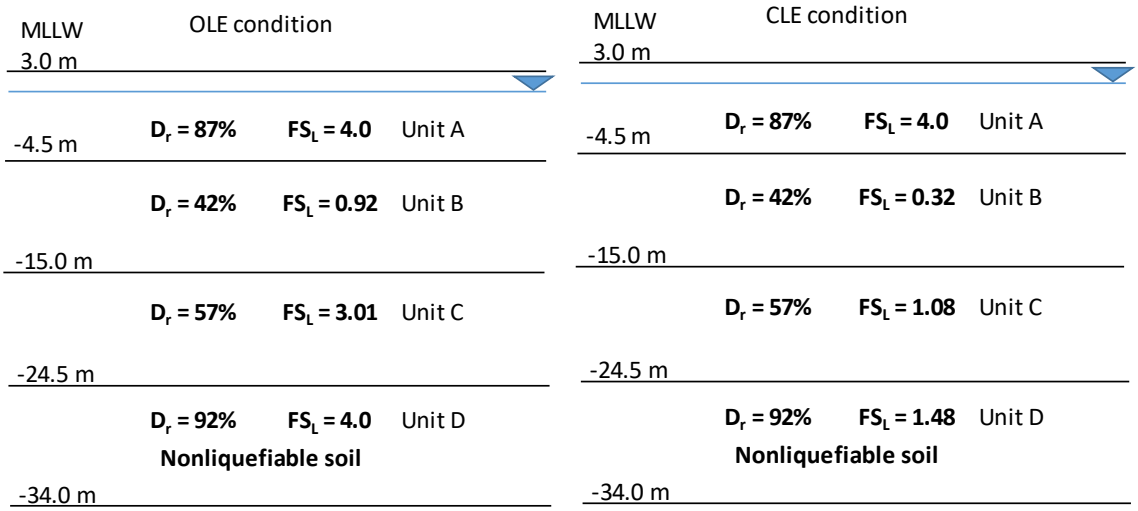

Fig. 44. Summarized soil profile and parameters to be input in LiquefyPro for the free-field settlement calculation under both OLE and CLE conditions.

Fig. 45 shows the calculated liquefaction-induced settlements with both methods under the OLE and CLE condition. Using the procedure suggested by Tokimatsu and Seed (1986), the calculated ground settlements using SPT data were about 24 cm for the OLE condition whereas for the CLE condition those were approximately 76 cm. On the other hand, the methodology developed by Ishihara and Yoshimine (1992) using also SPT data lead to the settlement values of 20 and 54 cm for the OLE and CLE conditions, respectively. It is hypothesized by the authors of this research that settlement calculations using the results of CPTs are more reliable than those obtained using SPTs. Hence, the maximum ground settlements computed based on CPT data using the Tokimatsu and Seed (1986) method were 2 and 22 cm for the OLE and CLE conditions, respectively. Settlements using Ishihara and Yoshimine (1992) approach were computed as 10 and 32 cm, respectively.

Those results evidence the potential for liquefaction-induced settlements by both earthquake levels. As expected, the computed settlements were larger for the CLE than the OLE condition, which is in agreement with the PGA values associated with each earthquake level. In general, larger maximum vertical deformations were obtained with the methodology proposed by Ishihara and Yoshimine (1992) than the approach by Tokimatsu and Seed (1986). It is interesting to note from those results the large discrepancies and scatter in the ground settlements obtained with those two

deterministic approaches. This problem of liquefaction-induced ground settlement, even under free-field conditions, is still a subject of numerous efforts in the geotechnical community and more research is needed to improve the predicting capabilities of simplified methods like those that can be readily used in current geotechnical earthquake engineering practice. It is important to mention that those methods take into account the reduction of the shear strength of the soil caused by liquefaction but cannot capture the process as failure occurs. Plasticity-based nonlinear dynamic methods, employed for site specific investigations using advanced finite element methods, could be a more effective way to determine liquefaction-induced settlements.

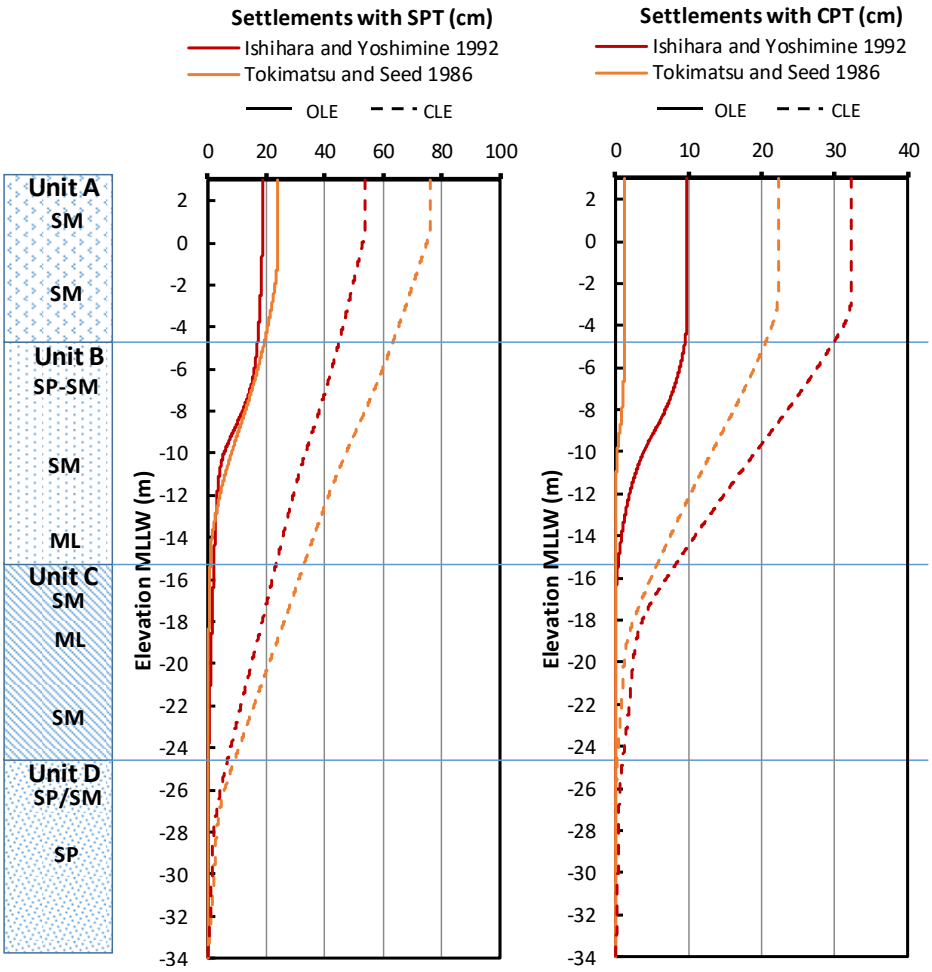

Fig. 45. Ground settlement evaluation for the OLE and CLE conditions with SPT and CPT data using classical approaches.

5. NUMERICAL EVALUATION OF THE PORT OF LONG BEACH

Earthquakes generate waves that propagate from the source at the bedrock level passing to the overlying soil layers causing ground surface shaking. In this propagation path, soils act as a filter to modify the characteristics of the ground motion from the source to the ground surface. These soil effects can be evaluated using three conventional approaches: attenuation relationship approaches, soil coefficient approaches and site response analyses. The first two approaches correspond to a simplification of the actual soil conditions and are typically performed by classifying the soils into one of the standard site conditions as indicated by current regulations and local codes or simply when soil coefficients are not available. The site specific response analyses to evaluate the seismic effects on soils and structures is part of the goals of this research for the soil stratigraphy of the Port of Long Beach (POLB), Pier S.

The modification of the seismic waves originated from the source and the abovementioned filtering effects are reflected in changes of the amplitude and frequency content of the ground motion at different depths along the soil profile. These characteristics can only be evaluated from site-specific ground response analyses. The input in these types of analyses consists of the soil stratigraphy, topography, soil stiffness, strength characteristics, groundwater considerations, and information of the earthquake excitation typically given in terms of acceleration or displacement time histories. The site-specific response should be ideally supported on a comprehensive site investigation extended to the rock or rock-like formation (firm ground). The determination of soil parameters must be performed for the different soil layers based on monotonic or cyclic loading under laboratory conditions (i.e., cyclic triaxial, cyclic direct shear, and resonant column tests) and a wide variety of field testing (i.e., cross-hole and down-hole *in situ* tests). In this project, the soil parameters were obtained from geotechnical field investigation reports performed at the project site. Unfortunately, advanced laboratory soil tests such as cyclic triaxial tests with bender element measurements, undrained and drained cyclic direct simple shear tests, or centrifuge tests were not

available. The geotechnical field exploration report provided conventional monotonic isotropically consolidated undrained triaxial compression (CIU-TXC) tests under four different confining pressures which will be used later in this chapter to evaluate the static monotonic response of these soils using the proposed constitutive soil parameters.

The numerical models used for liquefaction studies can be briefly classified in total and effective stress models. Total stress models, even though they are rather simple and few parameters are required, have the main disadvantage that the generation of excess pore water pressure is not captured, which is essential to understand soil behavior when subjected to cyclic loading and soil liquefaction. Soil models like the equivalent linear method that is typically a total stress model, are still widely used in practice but because they are based on an elastic framework, permanent deformations of the soil cannot be estimated (Finn et al. 1995). Therefore, the tendency in current numerical modeling is the use of effective stress models capable to include soil nonlinearly in the stress-strain formulation. In this family of effective stress models, the deformation of the soil is obtained with either partially or fully coupled models which link the solid and water phases in the overall soil behavior. In dynamic analyses, the effects of deformation of the soil skeleton coupled with water pressures are a main concern. Models like DYNAFLOW by Prevost (1981), DYNARD by Moriwaki et al. (1988), UBCSAND FLAC model by Byrne et al. (2011), DYSAC2 by Muraleetharan et al. (1988, 1991) and among others, are examples of those type of models (Marcuson W.F. et al. 2007).

For example, DYNAFLOW is a fully coupled numerical model based on nonlinear dynamic analyses with multi-yield surfaces capable to include anisotropic and isotropic analyses, and allows the dissipation and redistribution of pore water pressures during the application of the motion. DYNARD is a numerical model based on the finite difference method that incorporates the cyclic and nonlinear behavior of soils through a two-dimensional (2-D) bounding surface model allowing the study of soil behavior at large strains. The UBCSAND is a 2D model based on the plasticity theory with a hyperbolic hardening rule, especially accurate to predict the onset of liquefaction in sandy soils. DYSCAC2 is used for fully coupled nonlinear dynamic analyses of soils and is based on bounding surface plasticity. Some of those and other models are based on classical plasticity theory or more advanced developments have been performed with kinematic hardening, multi-yield surface or bounding surface plasticity. This advancement in the constitutive relationships have as a consequence the inclusion of a large number of constitutive parameters requiring numerous field or laboratory tests for their calibration. At times, advanced field or laboratory tests are not available

in some geotechnical projects or some parameters do not have physical meaning and are used mostly as factors calibrated to better match numerical simulations with laboratory tests.

In the numerical modeling of the liquefaction phenomenon, the constitutive model should ideally capture the most important features of soil behavior, that based on Kramer (2001) should include: i) nonlinearity in shear stress-strain response, ii) hysteretic response under cyclic loading, iii) dependence of low-strain shear modulus and shear strength on effective confinement, iv) dependence of shear strength on Lode angle, v) densification and consolidation of the soil skeleton and associated excess pore water pressure build-up due to shear loading, vi) dilation of soil skeleton and associated increase in effective confining pressure at large shear strain excursions, vii) attainment of critical void ratio state, viii) accumulation of cyclic shear strain under downslope shearing conditions, and ix) development of potentially large post-liquefaction volume reduction due to sedimentation. In dynamic numerical analyses, the definition of the soil model revolves between two opposing ideas. The use of a very simplistic soil model with few constitutive parameters easy to calibrate but rather limited in capturing soil behavior and limited controllability of the behavior by the user. Or the use of more advanced constitutive soil models that are more complex and offer the possibility to capture specific features of soil behavior but because of the large amount of parameters, very extensive field and laboratory testing are required as well as robust calibration and optimization procedures especially for those parameters that do not have a physical meaning.

In this research, the selection of the constitutive model to study the behavior of soils at the proposed site and comparison with other liquefaction triggering methods was based on the following considerations. First, the model used had to adequately capture key features of soil behavior regarding shear stress-strain behavior, stress dependency, generation of excess pore water pressure under monotonic and cyclic loading, and strain softening as the earthquake occurs. The constitutive soil model should accurately predict the onset of liquefaction. Second, the constitutive model had to be one of easy calibration mostly with field data, typically with Standard Penetration Tests (SPTs), Cone Penetration Tests (CPTs), or shear wave velocities (V_s), which constitute the main source of information at the POLB, Pier S. Third, the model must have a successful precedent on its use on the dynamic response of soils as obtained from advanced laboratory tests, including cyclic direct simple shear or cyclic triaxial tests. Finally, the constitutive model had to be well-documented and widely used to simulate performance of full-scale projects, specifically accurate enough to estimate liquefaction triggering and its mechanisms in loose soils. In this project,

advanced dynamic laboratory soil testing results are not available for the proposed site, therefore the "Class A" type predictions proposed herein are performed after the calibration of soil parameters with readily available field data. Thus, the selected constitutive soil model in this research is the UBC3D-PLM model with correlations and expressions of its constitutive parameters obtained mostly from the results of SPT tests. It has been shown in the past that the constitutive soil models UBC3D-PLM and Hardening Soil not only have shown to successfully capture soil behavior under dynamic loading but also have proven to be of easy calibration for those cases were limited subsurface and laboratory testing data are available for their calibration. For the reasons discussed before, the UBC3D-PLM is the model chosen in this project.

5.1 Description of the Numerical Model in PLAXIS 2D

The definition of the numerical model used to study liquefaction at the given site starts with an adequate definition of the geometry of the model in the finite element program PLAXIS 2D. The geometry was obtained from a detailed report of subsurface investigations performed at the POLB, Pier S. The information was complemented with the groundwater conditions of the site including the location of the groundwater table and information of any presence of groundwater flow at the target site. Thereafter, different soil models were evaluated in the preliminary phases from a list of potential models that constitute the state-of-the-art of liquefaction studies. For the reasons explained in the previous section, the model selected to perform the analyses was the UBC3D-PLM model. After the selection of the soil model and definition of the site geometry, the input ground motions were selected from site-specific studies of the local seismicity, major faults, probabilistic seismic hazard analyses, and availability of record motions from nearby seismic stations to the proposed site. The finite element mesh was defined based on minimum required finite element length criterion obtained from Kuhlemeyer and Lysmer (1973). They suggested to take an element size, at least, less or equal than one-eighth of the wavelength of the maximum frequency component f_{max} from the input wave. The average element size can be approximated as follows:

$$Avg.Elem.Size \leq \frac{\lambda}{8} = \frac{V_{s,min}}{8 f_{max}} \tag{36}$$

where $V_{s,min}$ is the lowest wave velocity of the soil. The port wide ground motion study at the POLB by Earth Mechanics Inc. (2006) had found that the minimum wave velocity is equal to 167 m/s and between the operating and contingency levels the highest frequency component is equal to

3 Hz, which leads to an average length of 7.0 m of each element of the mesh. From the program output, the maximum element size was 3.47 m.

The model boundary conditions for the groundwater and soils during the static stages were determined in the initial phase and a plastic nil-step was included to allow the generation of the initial stress field. Thereafter, the same definition was made for the dynamic calculation stages and the post-earthquake stages including the damped free-vibration and pore water pressure dissipation stages. Finally, the definition of the tolerance, time step, and other dynamic control parameters are defined in the dynamic calculation stage, which is modeled after the plastic nil step. In the dynamic phase, the displacements were reset and different models were run for several acceleration time histories corresponding to the Operating Level (OLE) and Contingency Level (CLE) earthquakes and applied at the base of the model. In these simulations, the Newmark time integration scheme was used. In this scheme the time step is constant and equal to the critical time step during the entire analysis allowing to solve the equilibrium equations of the system. The recommendation from PLAXIS 2D is to keep the defaults values for Alpha and Beta Newmark as 0.25 and 0.5, respectively.

Site specific response analyses of the POLB, Pier S subjected to an earthquake loading was performed assuming horizontally layered soil deposits subjected to vertically propagating shear waves. A one-dimensional (1D) wave propagation analysis was performed with the numerical model of the proposed site. This type of analysis is justified for those cases where the soil layers extend horizontally to infinity and the layers are relatively horizontal. The input seismic motion was composed by waves that propagate vertically which coincide with the actual shear waves propagating also in the vertical direction. In the numerical model, four soil layers were defined. Starting from the ground surface, the following subsurface conditions were specified in PLAXIS 2D: i) Unit A from +3 to -4.5 m Mean Lower Low Water elevation (MLLW) composed of compact fills mostly silty to clayey sands ; ii) Unit B from -4.5 to -15 m MLLW composed of mostly silty fine sands; iii) Unit C from -15 to -24 m MLLW composed of dense silty sand deposits; iv) Unit D from -24 to -37 m MLLW composed of very dense, medium to coarse grained sands; and v) at the bottom of the soil profile a rock-type layer was included from -37 to -39 m MLLW. The bottom rock layer is assumed to be the firm strata having the same characteristics of the outcropping rock where the earthquake signals were supposed to be recorded. The groundwater table, modeled using a hydrostatic head, was assumed to be located at -1.5 m under the ground surface corresponding to the approximate location found on the subsurface investigation report.

The type of drainage selected for the analyses corresponded to the "Undrained A" option in PLAXIS 2D. In this type of drainage condition, the undrained or short-term behavior of the material is characterized by stiffness and strength parameters based on effective stress properties. In this mode a large bulk modulus of water is automatically applied to make the soil incompressible and excess pore water pressures are computed. The entire soil deposit consists of mostly saturated alluvium deposits. In this type of analyses excess pore water pressures are generated but are not fully dissipated during the seismic motion because of the short duration of most earthquakes. For the static calculation phases default fixities were applied, which implies normally fixed vertical boundaries (i.e., roller supports) on the side and fully fixed conditions in both global directions applied at the base. The program includes several possibilities to simulate the boundary conditions for dynamic analyses that depend on the reflection or absorption nature of the seismic waves as the earthquake occurs. On the sides, tied degrees of freedom were applied as the boundary condition to tie the model nodes at the same elevation, assuming that they will have the same horizontal displacement resulting from the input earthquake motion (Galavi et al. 2013). Hence, for this calculation stage side boundaries of the tied degree of freedom type were applied and a compliant base was specified at the bottom of the model in which several earthquake time histories were applied as prescribed movements that occur at the bedrock level. **Table 11** provides a description of the modeling phases included in the numerical analyses using the stage construction interface in PLAXIS 2D.

Table 11. Calculation phases used in the numerical model with PLAXIS 2D.

Phase	Phase name	Phase description
1	Initial phase	Involves the calculation of the initial geometry and the initialization of the stress state. The initial soil stresses are obtained using a k_o-procedure.
2	Plastic nil-step	It is a plastic phase included to reset displacements, strains, and guarantee equilibrium in the computation of the initial stress field.
3	Dynamic analysis	Input earthquake motion at the base of the model to obtain the soil response and generation of excess pore water pressures.
4	Dissipation of excess pore water pressure	After the earthquake, high pore water pressures are developed. This stage is created to allow a drained response of the soil allowing excess pore water pressures to dissipate. This stage is not intended to simulate

		the resedimentaion process of the soil in the post-liquefaction stage, which is not included in the UBC3D-PLM constitutive model.

5.2 Definition of the Constitutive Model Parameters

In this project, the bottom rock layer was modeled with a linear elastic material and the alluvium and marine deposits of the remaining soil profile were modeled with the UBC3D-PLM model which is a tridimensional version of the UBCSAND model for liquefaction analyses originally proposed by Puebla, Byrne and Phillips (1997) and adapted to seismic evaluations by Beaty and Byrne (1998). The UBC3D-PLM constitutive model is implemented in the commercial finite element program PLAXIS 2D by Tsegaye (2010). Petalas and Galavi (2013) developed an improved version of the model in PLAXIS 2D.

Recent advances in soil plasticity have shown that more complicated models have emerged to understand the liquefaction behavior of soils. The main challenge has always been on how to apply those models in current practice to supersede the more conventional quasi-static or equivalent linear methods routinely used in geotechnical practice. The model used for this research stands out as a model that perfectly balances both, relatively small number parameters of easy calibration without sacrificing accuracy and capturing the main features of dynamic soil behavior. The UBC3D-PLM model used in this research project is available as a user-defined soil model through direct request to the PLAXIS sales department. The program uses dynamic undrained effective stress analyses that include the calculation of excess pore water pressures generated as the earthquake occurs along the numerical time steps. The program and constitutive soil model are capable to calculate the onset of liquefaction using the pore pressure ratio (r_u) as the main state variable. In this constitutive model, and in general in most models that are used to study the liquefaction potential of soils, the generation of excess pore water pressure and the computation of shear strains during seismic-induced cyclic loading is highly affected by the rotation of principal stresses which has been a major problem in the implementation of numerical models dealing with liquefaction. This feature is also rather limited in the UBC3D-PLM model.

This project is intended to study the application of the UBC3D-PLM model to study the liquefaction potential of the Port of Long Beach, Pier S. The soil model has its foundation in the UBCSAND model that was originally developed by Puebla et al. (1997) and Beaty and Byrne (1998). In spite of its rather complicated formulation, the UBC model in general is a constitutive model that have

shown great potential for current use in earthquake engineering practice because of the easy calibration with limited field or laboratory tests. Both the UBCSAND and the UBC3D-PLM models are effective stress models and use the classical plasticity framework decomposition of strains in elastic and plastic, defining the hardening rule in a hyperbolic manner. The main difference between both models is that the UBC3D-PLM uses a non-associative Drucker-Prager based plastic potential and a three dimensional Mohr-Coulomb yielding criterion. The UBC3D-PLM model has been recently improved to include a densification rule that improves the calculation of excess pore water pressures during cyclic loading. In the undrained effective stress analyses that are performed in PLAXIS, the soil stiffness and pore water pressures are not coupled. However, the results have shown to be satisfactory with respect to other programs based on finite differences like FLAC that can perform coupled effective stress analyses. Even though their initial and fundamental formulation is the same, both soil models mainly differ on their approach to degrade the stiffness of the secondary plastic shear modulus which controls the numbers of loading cycles to cause liquefaction (Tasiopoulou et al. 2015). Tasiapoulou et al. (2015) presented comparisons of the numerical model results using both models coded in PLAXIS 2D and FLAC in relation to the results of seismic centrifuge tests of a multi-block gravity quay-wall. The results of the dynamic analyses using both approaches resulted in similar horizontal and vertical deformations of the wall with respect to those observed in the centrifuge tests.

The parameters for the UBC3D-PLM model should be ideally calibrated from the results of cyclic direct simple shear tests or cyclic triaxial tests. Both tests can reproduce the stress paths that soils follow in the field during an earthquake. However, the availability of those tests for each soil layer in the field is rather limited in most geotechnical projects. Therefore, different authors have proposed simple correlations with traditional field tests that can be used for the calculation of soil parameters, which is one of the compelling reasons for the use of the UBC3D-PLM model for this research project. **Table 1** lists the 16 constitutive soil parameters needed for the UBC3D-PLM model.

In this research, an additional parameter is presented to correlate the relative density of each soil with the results of Standard Penetration Tests which are available for the current soil conditions. The relationship, originally proposed by Meyerhof (1957), can be shown as follows:

$$D_r = \sqrt{\frac{(N_1)_{60}}{C_d}} \tag{37}$$

where C_d corresponds to a calibration factor originally taken as 46. Recently, other researchers, for example Idriss and Boulanger (2008), have shown that this value depends on the type of sand, grain size distribution, stress history, and type of deposition. A more realistic range of variation is from 36 to 60 but the authors have suggested a value of 46 for liquefaction evaluation based on SPT or CPT data.

Beaty and Byrne (2011) proposed equations and correlations with corrected clean sand blow count values, $(N_1)_{60}$, obtained from SPTs. This was proposed to overcome potential lack of advanced laboratory testing for each representative type of soil and instead use the available results of SPTs, CPTs and measurement of V_s to calibrate the soil parameters. This way, the model parameters are very easy to determine with conventional geotechnical field tests and becomes attractive for its use in current geotechnical engineering practice. These correlations, originally proposed for the UBCSAND 904aR model have been revised and implemented on the UBC3D-PLM soil model by Makra (2013) and are adopted in this research as a practical way to determine the constitutive parameters. The proposed correlations with SPTs are expressed as follows:

$$\phi_p = \phi_{cv} + \frac{(N_1)_{60}}{10} + MAX\left(0\,, \frac{(N_1)_{60} - 15}{5}\right) \tag{38}$$

$$K_G^e = 21.7 \times 20(N_1)_{60}^{0.3333} \tag{39}$$

$$K_B^e = 0.7K_G^e \tag{40}$$

$$K_G^p = K_G^e(N_1)_{60}^2 \times 0.003 + 100 \tag{41}$$

$$R_f = 1.1(N_1)_{60}^{-0.15} \tag{42}$$

where ϕ_p represents the peak friction angle, ϕ_{cv} is the critical state friction angle which is the friction angle at constant volume, K_G^e and K_B^e are the elastic shear bulk moduli of the soil, K_G^p is the

plastic shear moduli of the soil and R_f is the failure ratio. The stress-dependency power values for the bulk and shear moduli denoted as m_e, n_e, and n_e can be assumed as default values 0.5, 0.5 and 0.4, respectively. These calibrations suggested default values for the hardening and post-liquefaction factors (i.e., fac_{hard} and fac_{post}, respectively) taken both as 1.0. However, other researchers like Makra (2013) suggested after calibrations with laboratory tests and field observations of the performance of the San Fernando Dam after 1971 San Fernando earthquake that those factors are 0.45 and 0.02, respectively. Those values were originally obtained from Fraser river sand. More detailed calibrations using numerical models of cyclic direct simple shear tests for the specific conditions of the POLB are presented in the following sections.

The friction angle at constant volume can be determined either with correlations with field tests or from the results of static drained triaxial compression tests (or undrained with pore pressure measurements). Using the theory of elasticity and manipulating Eq. (40), which represents a relation between elastic shear and bulk moduli, would lead to a Poisson ratio of 0.02 which is not a plausible value for static calculations. Hardin (1978) and Negussey (1984) presented the strain dependency of the Poisson's ratio in the range of small strains and concluded that the variation is between 0 and 0.2. However, in dynamic calculations the soil behavior at small strains is important and therefore such a low value of the Poisson's ratio could be justified. This also justifies the use of a different constitutive model for the initial static stress initialization of the numerical model. In this research the Hardening Soil model is used to initialize the static stress field and improve the UBC3D-PLM model deficiencies when dealing with the generation of the initial static shear stresses of the soil deposit. **Table 12** presents the parameters used in this research for each soil layer modeled with the UBC3D-PLM model.

Table 12. Constitutive soil parameters of each Soil layer modeled with UBC3D-PLM.

Parameter	Unit A	Unit B	Unit C	Unit D
ϕ_{cv} (°)	34	34	29.3	30
ϕ_p (°)	41.50	34.8	30	38.70
C (kPa)	0	0.00	0	0
K_G^e	1417.96	867.40	1069.37	1469.99
K_G^p	5311.01	266.54	821.82	6807.56
K_B^e	992.57	607.18	748.56	1028.99
n_e	0.50	0.50	0.50	0.50
m_e	0.50	0.50	0.50	0.50
n_p	0.40	0.40	0.40	0.40
R_f	0.65	0.81	0.73	0.63
Pa (kPa)	100.00	100.00	100.00	100.00
σ_t *(kPa)*	0.00	0.00	0.00	0.00
fac_{hard}	0.45	0.45	0.45	0.45
$(N_1)_{60}$	35	8	15	39
fac_{post}	0.02	0.02	0.02	0.02

As mentioned before, previous research in the use of the UBC3D-PLM model (Makra 2013; Petalas and Galavi 2013; Winde 2015) evidenced that the model does not calculate correctly the state initial state of stresses and therefore the static shear, which leads to inaccuracies in the results because of the dependency between static shear and liquefaction behavior of soils. Therefore, it was necessary in the numerical model to initialize the static state of stresses in the soil with a different material model capable to determine accurately the static state of stresses. The model selected to initialize the static stress field was the Hardening Soil (HS) model that not only has been used in numerous studies and case histories in the past, but also is commercially available and easy to calibrate with

few field and laboratory tests. The HS model has a failure criterion based on Mohr-Coulomb and a multi-yield surface with a cap surface for the development of volumetric plastic strains and a shear surface for plastic shear strains under the cap. This multi-yield surface model combines two type of flow rules: i) an associative flow rule for the cap surface, and ii) a non-associative for the shear surfaces, allowing the model to simulate the dilatancy of the soil during the loading phase (Schanz et al. 1999). **Table 13** presents the HS model soil parameters and a brief description of their physical meaning.

Table 13. Constitutive soil parameters used in HS model.

Parameter	Description
ν'_{ur}	Poisson's ratio
m	Power for stress-level dependency of stiffness
E_{50}^{ref}	Secant stiffness in standard drained triaxial test
E_{oed}^{ref}	Tangent stiffness for primary oedometer loading
E_{ur}^{ref}	Unloading/reloading stiffness
Φ'	Friction angle
ψ	Dilatancy angle
c'_{ref}	Cohesion intercept
R_f	Failure ratio
$Pref$	Reference pressure equal to the atmospheric pressure in kPa

In both models the total unsaturated and saturated unit weights for the Unit A were taken as 20.1 and 20.8 kN/m^3. For the Units B, C, and D both unit weights were taken as 18.1, 18.9 and 19.6 kN/m^3, respectively. The following assumptions were made for the calibration of the new set of constitutive parameters: i) the power coefficient m is usually taken as 0.5 for sandy soils, ii) $k_G^e \,.\, p_{ref}$ is close to the reference value of the initial shear stiffness G_0^{ref}, iii) the ratio G_0/G_{ur} is 3, iv) assuming a Poisson's ratio of 0.2, the parameters E_{ur}, E_{oed}, and E_{50} are easily calibrated and calculated as 1/3 of E_{ur}. **Table 14** presents the parameters used for the initial and static phases of the numerical model including also the K_0 values which were computed using the Jaky's formula (1944).

Table 14. Constitutive soil parameters used for the HS model in Phases 1 and 2 of the numerical simulations.

Parameter	Unit A	Unit B	Unit C	Unit D
ν'_{ur}	0.2	0.2	0.2	0.2
m	0.5	0.5	0.5	0.5
E_{50}^{ref} (kPa)	22687.38	13878.38	17109.92	23519.83
E_{oed}^{ref} (kPa)	22687.38	13878.38	17109.92	23519.83
E_{ur}^{ref} (kPa)	68062.14	41635.13	51329.77	70559.50
Φ' (°)	41.5	34.8	31.5	38.7
Ψ (°)	1	1	1	1
c'_{ref} (kPa)	0	0	0	0
K_0	0.44	0.44	0.50	0.50
R_f	0.9	0.9	0.9	0.9

The firm strata or rock formation at the bottom of the soil profile was modeled using a linear elastic material under drained conditions. The shear wave velocity at the bottom of the soil profile corresponding to the rock-type materials, was assumed to be approximately 1,200 m/s. Those values are only estimates because results of shear wave velocities at depths larger than 25 m were not available. This assumption is consistent with other studies like Petalas and Galavi (2013) in which shear wave velocities larger than 800 m/s are used as an indication of rock-like formations. **Table 15** lists the parameters used for the bottom rock formation.

Table 15. Linear elastic parameters used for the rock strata in the numerical model.

Parameter	Rock formation
ν'_{ur}	0.2
E (kPa)	7.756×10^6
Vs (m/s)	1200
γ_{unsat} (kN/m^3)	22
γ_{sat} (kN/m^3)	22

5.3 Soil Behavior during Cyclic Loading

An explanation of the soil behavior using the proposed constitutive model when an element of soil is subjected to cyclic loading is explained in this section. Previous research on the use of constitutive models to study the dynamic behavior of soils have shown that the calibration should be preferably performed with the results laboratory tests of soils under cyclic loading such as direct simple shear devices, cyclic triaxial or torsional shear (Beaty and Perlea 2012; Finn et al. 1995; Marcuson W.F. et al. 2007). These tests closely resemble the stress paths that the soil follow in the field and therefore the results will provide a better match with respect to measured field performance. The objective of this section is to determine the most appropriate soil parameters using the UBC3D-PLM model by performing numerical analyses of boundary value problems that would fit resistance curves of liquefaction obtained from the analyses of different case histories.

Soil stress-strain behavior is characterized by nonlinear behavior and stiffness have shown to be stress and strain dependent. Even in a uniform and homogeneous soil deposit, soil stiffness varies with depth and decays with the strain level induced by the applied loading. The maximum strain at which the soil behavior can be considered purely elastic is very small, approximately in the order of $1x10^{-6}$. Soil stiffness associated with this strain range is indicated as the initial stiffness and its value decays by increasing the strain amplitude according to different characteristic curves published for different type of soils displaying also known as modulus reduction.

Under dynamic loading, the soil is subjected to shearing cycles, showing not only a nonlinear decrease in the soil stiffness but also a dissipative behavior. The hysteretic behavior of soils generated during cyclic shear loading consists of a sequence of loading and unloading paths, characterized by increasing values of irrecoverable deformations. In general, it has been observed that earthquakes induce small strain levels in the soil, that exhibits a high shear stiffness G_0, and that stiffness decreases with increasing values of shear strains (γ) while the amount of dissipated energy by the soil increases. Several cyclic drained direct simple shear (DSS) tests were modeled in PLAXIS 2D by other researchers (e.g., Beaty and Byrne 1998; Makra 2013; Petalas and Galavi 2013; Puebla et al. 1997; Tsegaye 2010). Those results suggested that the UBC3D-PLM model over-damped the soil response compared to actual soil behavior because of the linear elastic unloading rule of the model with a constant shear modulus equal to G_{max}. These results lead to large areas computed inside the hysteretic loop response of the DSS tests.

In this section, the parameters for the UBC3D-PLM model were calibrated using boundary value element simulations. These parameters will be used in the following chapters for the numerical simulations of liquefaction of the Port of Long Beach. The parameters were mainly calibrated from existing correlations with SPT with the exception of the densification and post liquefaction factors that were obtained from the analyses of soil conditions of Unit B to reproduce published empirical cyclic strength curves. Using the proposed numerical parameters, it was demonstrated the practicality of using the proposed model and methods to study the onset of soil liquefaction of a given site. It is important to mention that even though the model is suitable for the development of shear strains arising from cyclic loading, the post-liquefaction behavior is still very limited. This is because the change in volumetric strains during post-liquefaction reconsolidation of sands are still difficult to model numerically. In typical plasticity based models, strains are separated into elastic and plastic components and the strains generated during post-liquefaction do not belong to any of those two types of strains. Thus, constitutive models tend to under predict those strains in comparison with laboratory experiments (Boulanger and Ziotopoulou 2015). This topic is still a main concern in current state of the practice of soil liquefaction. More recently, Boulanger and Ziotopoulou (2015) proposed the PM4Sand model that incorporates calculation of post-shaking reconsolidation strains by a pragmatic approach reducing the post-shaking elastic shear and bulk moduli which increases the resulting strains and in this way accounting for sedimentation strains arising in the post-liquefaction stage. These sedimentation strains represent changes in volume in the soil mass when the effective stresses in the soil are very close to zero and excess pore water pressure near its maximum possible.

Table 16 lists the parameters used for the numerical simulations of undrained cyclic DSS tests performed for Unit B. Those parameters were computed using the correlations proposed by Beaty and Byrne (2011) and include the densification factor (fac_{hard}) and post liquefaction factors (fac_{post}), that resulted to be the most appropriate parameters to calibrate the onset and strength of soils to liquefaction as tested under undrained DSS conditions. The undrained DSS tests were developed using the *Soil Test* numerical tool embedded in PLAXIS 2D. The soil test conditions were generated from the "general" option in the program and the test type was manually adjusted to simulate the boundary conditions appropriate for undrained DSS Tests. The results were obtained with stress-controlled numerical simulations by applying the same shear stress in each step. A maximum of 40 loading steps (i.e., 20 cycles) for the entire test were used in each simulation to

reach the post-liquefaction stage and conclude about the model capabilities to capture soil post-liquefaction.

Table 16. UBC3D-PLM model parameters used for the numerical simulations of undrained cyclic DSS tests.

Parameter	Unit B
ϕ_{cv} (°)	34
ϕ_p (°)	34.8
C (kPa)	0.00
K_G^e	867.40
K_G^p	266.54
K_B^e	607.18
n_e	0.50
m_e	0.50
n_p	0.40
R_f	0.81
Pa (kPa)	100.00
σ_t *(kPa)*	0.00
fac_{hard}	0.45
$(N_1)_{60}$	8
fac_{post}	0.02

In this research, the procedure used for the calibration of the constitutive soil parameters to be used in the numerical analyses was to find the most appropriate parameters to reproduce the cyclic strength curve of the liquefiable soil deposits as the proposed by Seed et al. (1985) (see **Fig. 8**). It has also been shown by Seed (1985) a relationship between number cycles necessary to induce liquefaction in the soil as a function of the cyclic stress ratio (CSR) and the earthquake magnitude. **Table 17** presents those results in which for a magnitude earthquake of 7.5, liquefaction is reached for a total of 15 uniform cycles. Liquefaction was quantified in that study with and excess pore water pressure ratio of 100% and shear strain levels of ± 5%. In the numerical simulations of the DSS tests presented herein, these values were used as target values necessary to obtain the combination of CSR normalized at 100 kPa and $(N_1)_{60}$ to reach liquefaction at approximately 15

loading cycles. In that case, the input CSR will correspond to the Cyclic Resistant Ratio (CRR) and if the parameters selected are appropriate, the results will match the curve presented in **Fig. 8**. Liquefaction in this section is defined as the CSR to generate a pore pressure ratio of 85% (Beaty and Byrne 2011), which has been observed to be a reasonable lower limit for r_u necessary to cause high generation of excess pore water pressures and consequently, significant reduction in the shear strength of soils.

Table 17. Scaling factors for effect of earthquake magnitude on CSR causing liquefaction (After Seed et al. 1985).

Earthquake magnitude, M	Number of representative cycles at 0.65 τ_{max}	Scaling factor for stress ratio
8-1/2	26	0.89
7-1/2	15	1.0
6-3/4	10	1.13
6	5-6	1.32
5-1/4	2-3	1.5

Fig. 46 and **Fig. 47**, present the results of pore water pressure ratios, stress-strain curves, and stress path responses for undrained cyclic direct simple shear tests for different values of CSR and relative densities calculated with Equation (37). **Table 16** shows the final calibrated soil parameters for the liquefiable soil deposit for Unit B that were determined as the result of several iterations to obtain a reasonable representation of the semi-empirical cyclic strength curves presented by Seed et al. (1985) and Idriss and Boulanger (2004). As an additional reference, the results obtained by Makra (2013) obtained for Fraser river sand are also presented in the figure. The results are presented for zero initial static shear stress ratios and K_0 values of 0.44, which is approximately the K_0 value estimated for the liquefiable Unit B in the site. A post-liquefaction factor of 0.02 and a densification factor of 0.45 were shown to match reasonably well with those proposed by Makra (2013) and are appropriate values to reach the conditions shown in the cyclic strength curve. The figures show that liquefaction, defined as pore water pressure ratios of 85% or more, is reached approximately at 15 cycles for all cases. **Fig. 46**c corresponding to a relative density of 74% (i.e., about medium-dense sandy soil) show that in order to reach liquefaction for those relatively small level of cycles (15), the soil needs to be subjected to higher levels of cyclic stress ratios which in that case correspond to a CSR of 0.25. Conversely, as expected for loose to medium sandy soils with a relative density

of about 42%, lower levels of cyclic stress ratios are needed to reach liquefaction at a total of 15 cycles.

It is important to note that previous research performed on the UBC3D-PLM model of soils subjected to cyclic loading (e.g., Petalas and Galavi (2013) and Makra (2013)) showed that for lower CSR values, characteristic of low values of relative density, the model underestimates pore water pressure ratios in relation to experimental test results. This is particularly valid for low values of loading cycles. It is observed from stress paths shown in **Fig. 46** that the soil starts to soften and through each loading and unloading cycle the spacing between cycles reduces because of the activation of the densification rule which was added in the latest version of the model (Petalas and Galavi 2013). This densification rule was validated with experimental tests of sands subjected to cyclic loading that evidenced some degree of densification before the onset of the liquefaction. This soil densification rule improves the accuracy in the predicted evolution of excess pore water pressures. From the figure, it is also evident the activation of the densification rule in the curves of pore water pressure ratios versus the number of cycles. Regardless of the CSR value, this rule is activated at approximately 5 cycles or less. A change of slope in the curves of pore water pressure ratios occurs for r_u values of about 0.5 or less. This change of slope along with the reduction of the space between cycles in the stress path figures for vertical effective stresses of 50 kPa or more, serves as an indication of the activation of the densification rule.

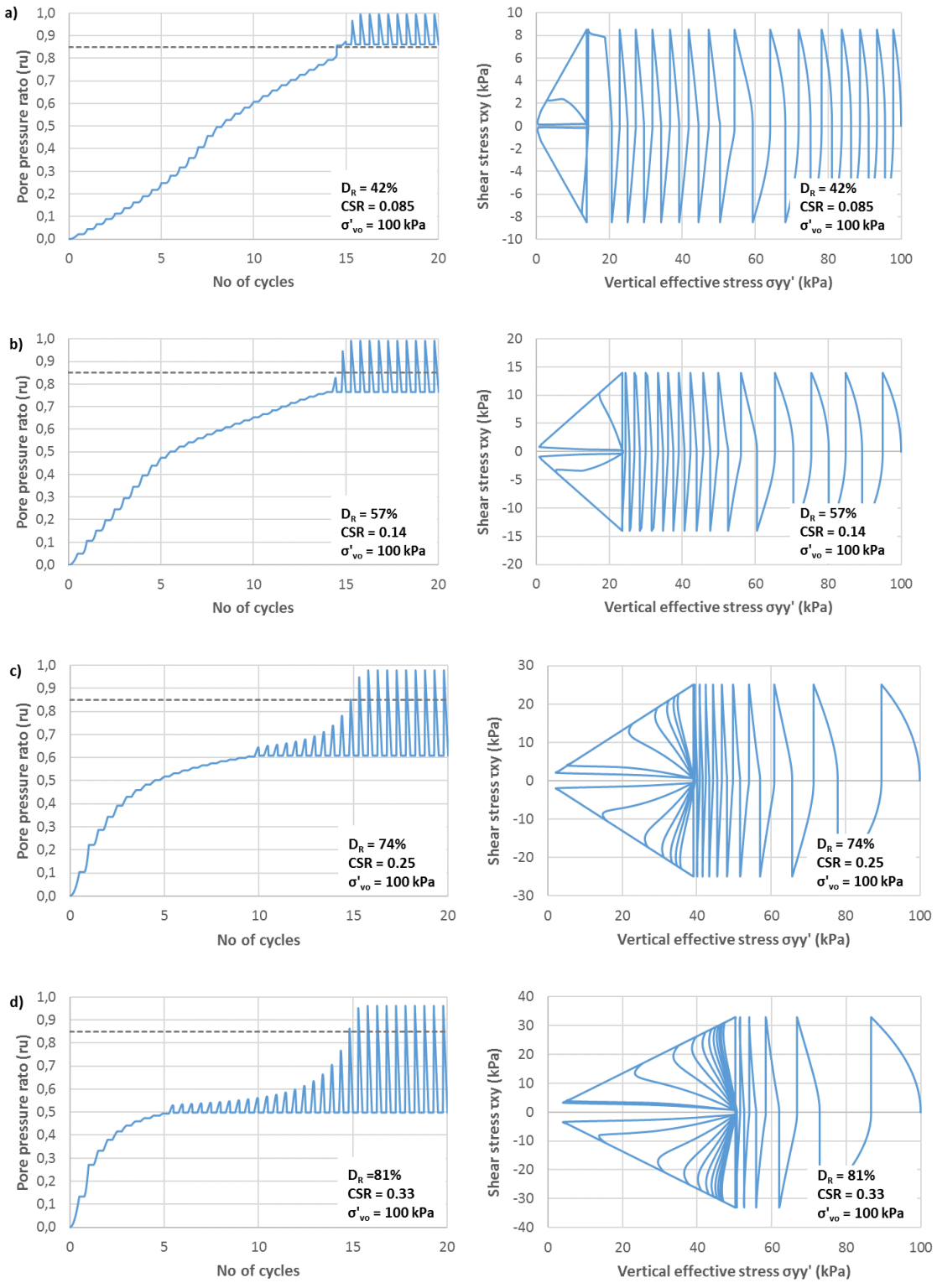

Fig. 46. Results of pore pressure ratios and stress paths computed from the numerical simulations of undrained cyclic direct simple shear tests obtained with the numerical model for different D_r values a) 42%, b) 57%, c) 74% and d) 81%.

The stress strain behavior curves for each relative density are isolated in **Fig. 47**. The figure shows the ability of the model to progressively increase the shear deformations as the loading cycles occur. In the first 15^{th} cycles, during the cyclic mobility stages, the model properly accounts for the degradation of the initial shear modulus evidenced by a decrease in the slope of the hysteretic loop. This feature generates large permanent plastic deformations in the soil mass. However, the model is rather limited once a pore pressure ratio high enough to induce liquefaction is reached because the model does not allow further degradation and softening of the soil and therefore cyclic mobility cannot be properly simulated with the UBC3D-PLM model. This is evidenced from **Fig. 47** a), b), c) and d) that shows that the soil repeats the same loop in the stress-strain curves and therefore the post-liquefaction behavior of the soil is very uncertain. One possible numerical strategy to avoid this issue is applying a very small value, in the order of 10^{-2}, to the post-liquefaction factor in the model parameters. Even under those limitations, the model is still valuable to predict the onset of liquefaction for the case of loose sands and dense sands for high CSR values. The results are more reliable for loose sands than for medium dense sands as quantified with the relative density because high pore water pressures are achieved before the model reaches the yield surface.

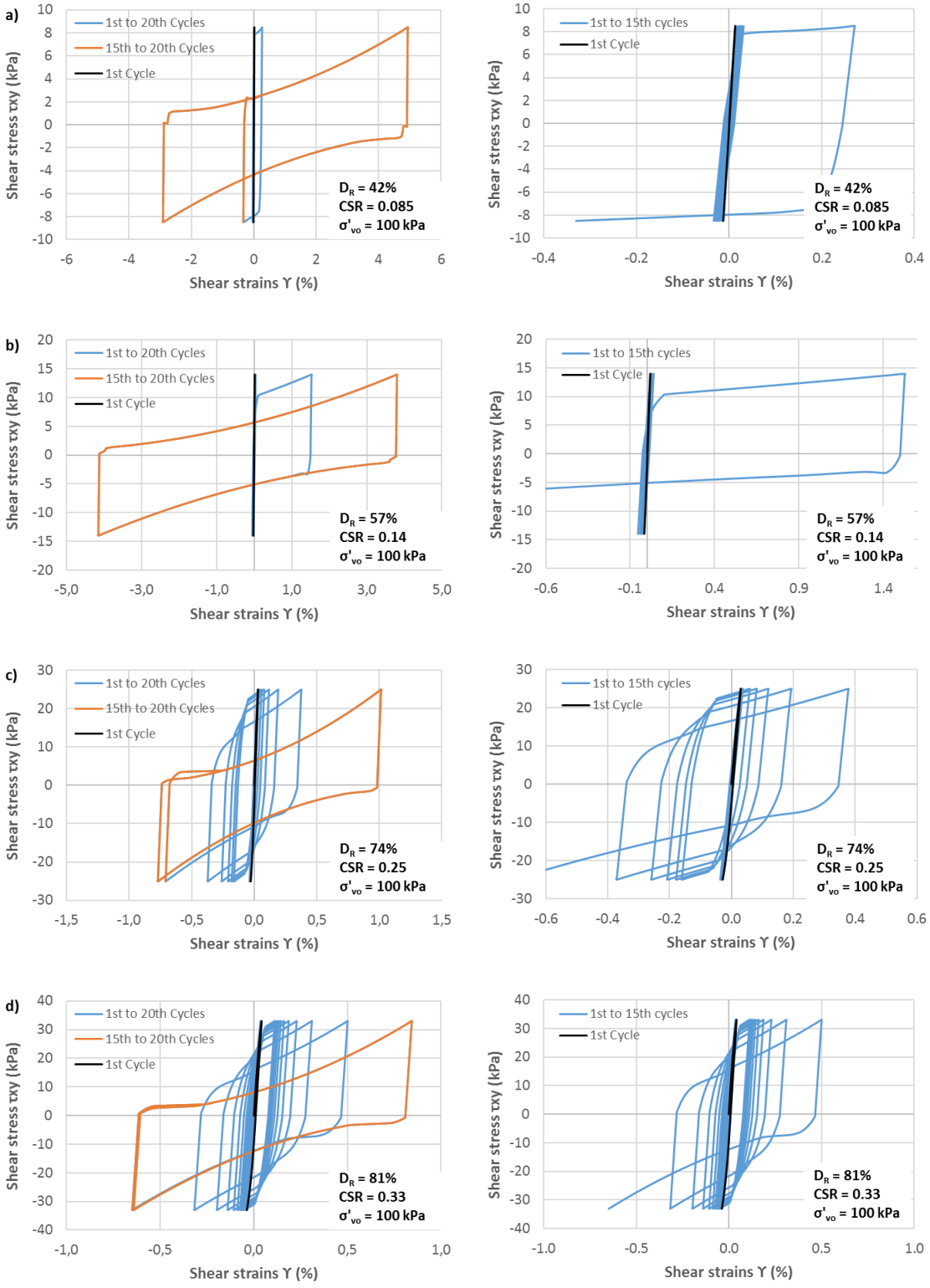

Fig. 47. Stress-strain behavior within 15 and 20 cycles of undrained direct simple shear tests obtained with the numerical model for CSR values of a) 0.085, b) 0.14, c) 0.25 and d) 0.33.

Table 18 presents a summary table of the undrained cyclic DSS numerical simulations varying CSR and $(N_1)_{60}$ to reach liquefaction at 15 cycles. Those results are plotted in **Fig. 48** in relation to other studies on cyclic strength curves including Seed et al. (1985), Idriss and Boulanger (2003), and Cetin et al. (2004). The figure shows that the results of undrained cyclic DSS numerical simulations for Unit B at the POLB, Pier S using the proposed parameters shown in **Table 16**, reasonably match the overall trend depicted by other studies, only being slightly under predicted for large values of SPTs. Unit B presents an average SPT value $(N_1)_{60}$ of approximately 8 (i.e., D_r= 42%), and if the CLE and OLE earthquake levels produce CSR values larger than 0.085, liquefaction is very plausible as shown in the cyclic strength curve reproduced with the numerical simulations. The approximate match between the computed and expected results from other published research for Unit B provides confidence that at least in the numerical simulations of boundary value problems, the onset of liquefaction can be studied with the UBC3D-PLM. The following chapters will deal with the site-specific application and extension of these results to the liquefaction effects in the POLB, Pier S.

Table 18. CSR to reach liquefaction for different values of the relative density.

$(N_1)_{60}$	D_r (%)	CSR
8	42	0.085
15	57	0.14
25	74	0.25
30	81	0.33

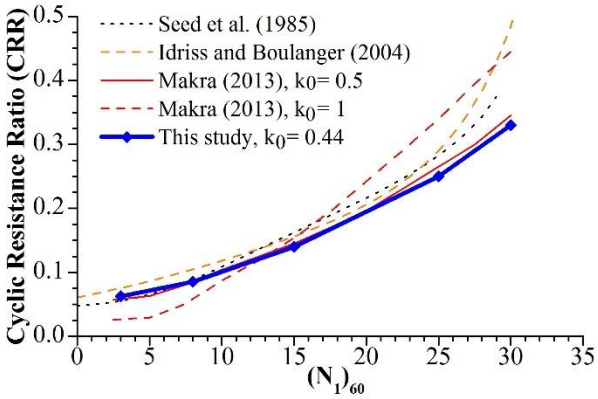

Fig. 48. Cyclic strength curve for Unit B compared with other semi-empirical procedures (Boulanger and Idriss 2004; Makra 2013; Seed et al. 1985).

5.4 Soil Behavior during Monotonic Loading

After the calibration of the soil behavior during cyclic loading using the UBC3D-PLM constitutive model, an evaluation of the same soil parameters to reproduce monotonic triaxial compression (TXC) tests is presented. Several monotonic isotropically consolidated undrained triaxial compression (CIU-TXC) tests with four different confining pressures were obtained from the geotechnical investigation reports of the project site. **Fig. 49** shows the deviatoric shear stress and excess pore water pressure versus axial strain for soil specimens extracted from Shelby tubes from the upper portion of Unit C at elevations between -15.6 and -17.7 m-MLLW. Shearing of the soil samples under triaxial loading were carried out under strain-controlled conditions at strain rates of about 0.01 cm/min. Four samples were tested with different consolidation effective stress (σ'_c or σ'_3) corresponding to 72, 143, 239, and 335 kPa. *In situ* vertical effective stress was computed as 185.5, 202.4, 203.8, and 205.2 kPa respectively.

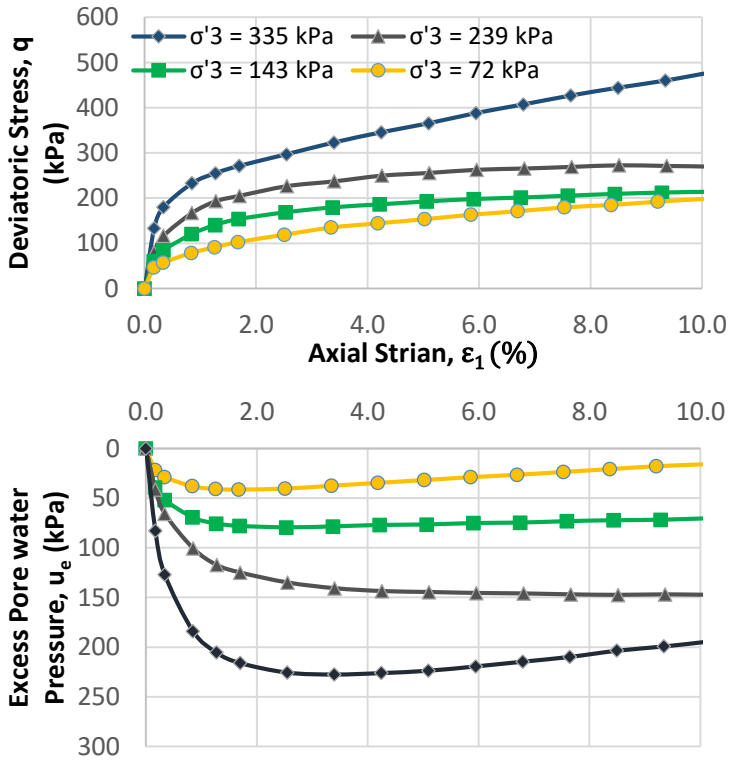

Fig. 49. CIU-TXC tests conducted by AP Engineering and Testing, Inc. at the project site.

The results of the monotonic CIU-TXC tests were also simulated using PLAXIS 2D and compared with the laboratory results presented before. **Table 19** shows the soil parameters used for these simulations that were obtained using Eqs. (38) to (42) for an approximate SPT $(N_1)_{60}$ value 11

corresponding to the location of the tested soil samples. The same densification and post-liquefaction factors were used as those previously used for the cyclic DSS tests, 0.45 and 0.02, respectively. From these laboratory tests, a peak friction angle of 30° was determined using a Mohr Coulomb failure envelope of the tests and that was the value proposed in these simulations. **Fig. 50** shows the results of the monotonic CIU-TXC test numerical simulations.

Table 19. UBC3D-PLM model parameters used for the numerical simulations of monotonic CIU- TXC tests for a sample taken at elevation between -15.6 and -17.7 m-MLLW.

Parameter	**Values for soil samples located between -15.6 and -17.7 m-MLLW with $(N_1)_{60}$= 11**
ϕ_{cv} (°)	29.3
ϕ_p (°)	30
C (kPa)	0.00
K_G^e	964.44
K_G^p	450.09
K_B^e	675.11
n_e	0.50
m_e	0.50
n_p	0.40
R_f	0.77
Pa (kPa)	100.00
σ_t *(kPa)*	0.00
fac_{hard}	0.45
$(N_1)_{60}$	11
fac_{post}	0.02

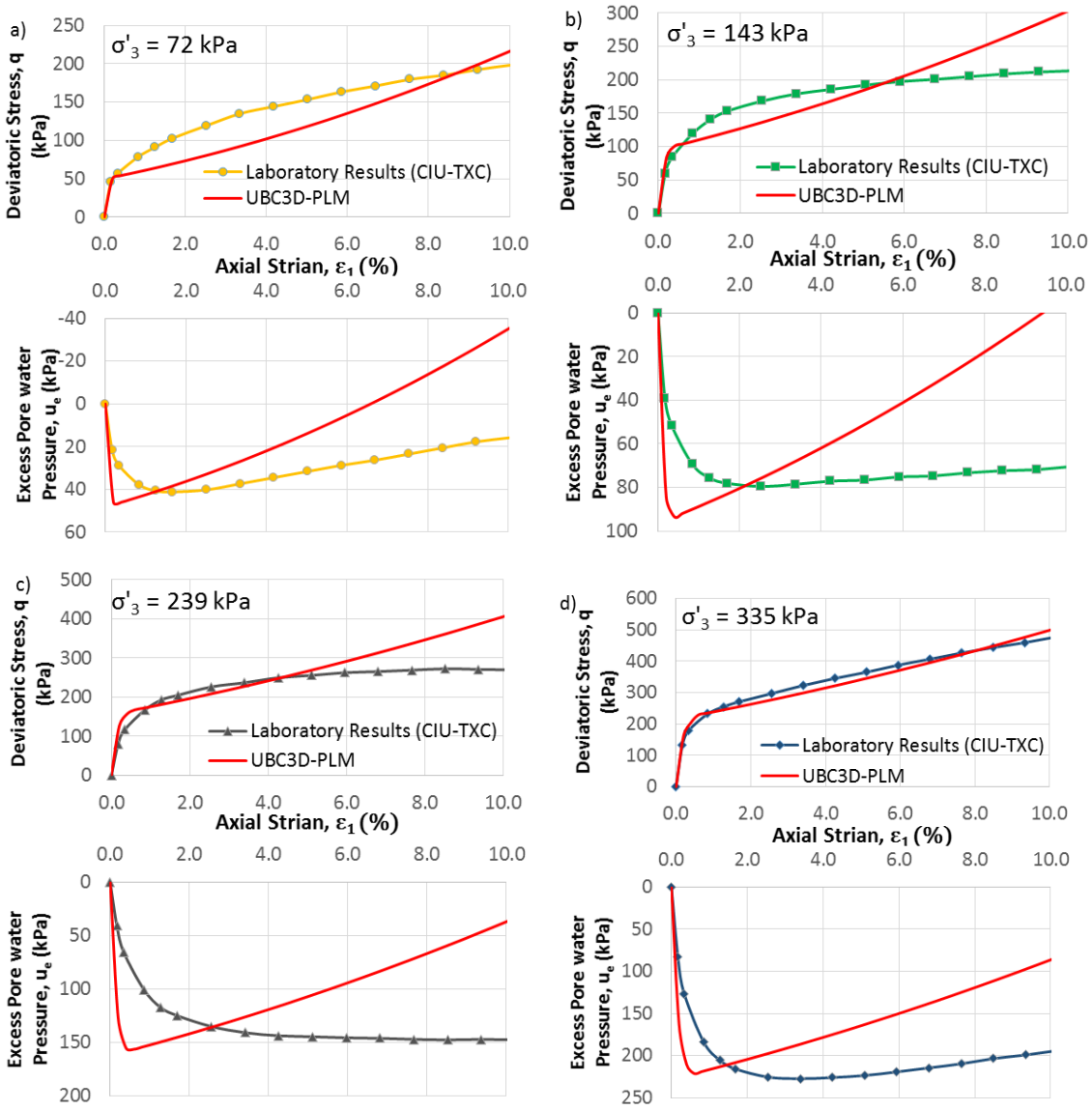

Fig. 50. Comparison of CIU-TXC test results and numerical simulations using UBC3D-PLM model in PLAXIS 2D for different confining pressures: a) σ'_c=72 kPa, b) σ'_c=143 kPa, c) σ'_c=239 kPa and d) σ'_c=335 kPa.

It is concluded from the figures that the soil response under monotonic triaxial stress probes as obtained from the PLAXIS 2D numerical simulations agree well with the laboratory results. For large confining pressures, the numerical simulations with the UBC3D-PLM model showed a better match with respect to the experimental values. Larger discrepancies were observed for low confining pressures. At the small strain levels (i.e., axial strains less than 1%), the model shows a stiffer response in undrained conditions. The soil parameters and the calibration as presented in this section will serve as the basis of the finite element simulations of the project site.

5.5 Input Seismic Motions in the Numerical Model

The selected time histories that were applied at the elevation of the firm strata (i.e., rock modeled at the bottom of the soil profile assumed to be similar to the properties of the outcropping rock in which the seismic motions were recorded) were scaled so that they match the Peak Ground Acceleration values reported in the Port of Long Beach Ground Motion report. Those peak ground accelerations corresponded approximately to 0.21g for the OLE and 0.50 g for the CLE earthquake levels and were characterized by magnitudes Mw of 6.5 and 7.0, respectively. The input time histories of each earthquake analyzed in this report are shown in **Fig. 51** for the OLE conditions and in **Fig. 52** for CLE condition.

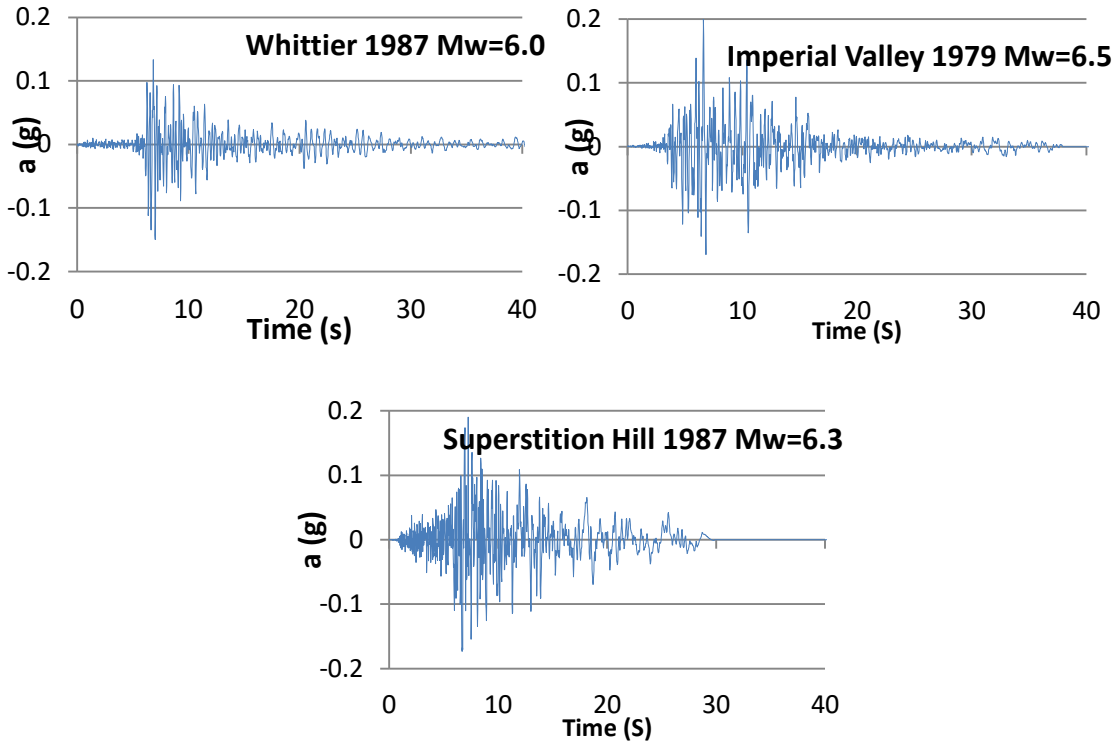

Fig. 51. Input acceleration time histories for the OLE condition (USGS 2016).

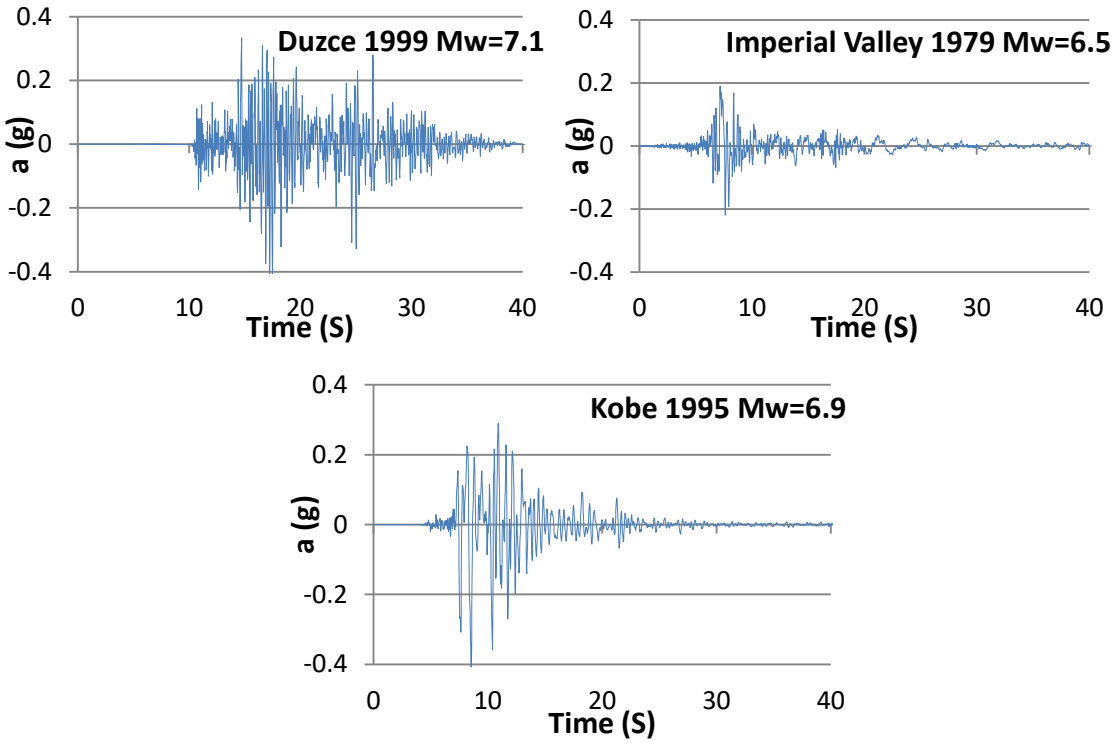

Fig. 52. Input acceleration time histories for the CLE condition (USGS 2016).

Fig. 53 and **Fig. 54** show the predominant frequency for each earthquake motion presented in this research that were computed in PLAXIS 2D and DEEPSOIL by applying the Fast Fourier Transform (FFT) of the input acceleration time history. The software DEEPSOIL is an equivalent linear and nonlinear seismic site response program to assess the seismic response of one-dimensional soil columns in time domain as well as in frequency domain. Those FFTs were performed for a point located at the bottom of the model and thus, represent the input predominant frequency of each earthquake motion that will be used in the numerical simulations. **Table 20** shows a summary of the predominant frequencies of the earthquakes for the OLE and CLE conditions. Both FFTs calculated with PLAXIS 2D and DEEPSOIL show similar predominant frequencies.

Table 20. Predominant frequencies of the earthquakes for OLE and CLE conditions calculated with PLAXIS 2D and DEEPSOIL.

Earthquake Input	Predominant frequency of the earthquake (Hz), PLAXIS 2D	Predominant frequency of the earthquake (Hz), DEEPSOIL
Whittier OLE	1.69	1.69
Imperial Valley OLE	2.09	2.09
Superstition Hill OLE	2.75	2.75
Duzce CLE	3.81	3.81
Imperial Valley CLE	0.65	0.65
Kobe CLE	1.46	1.46

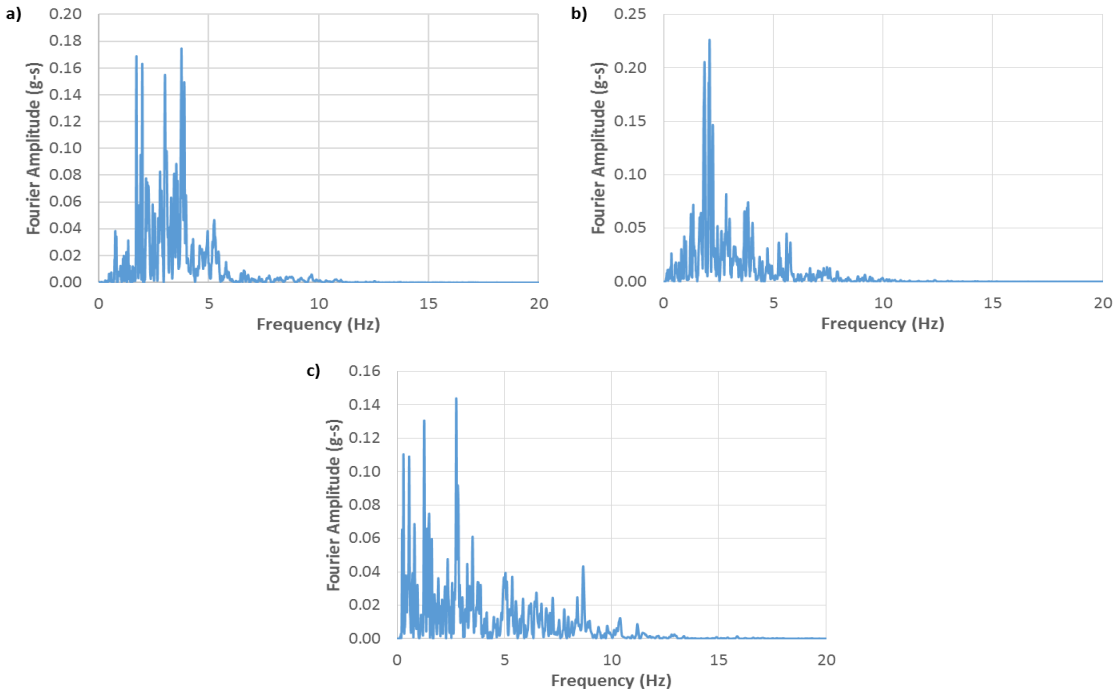

Fig. 53. Fast Fourier amplitude for a node at the bottom of the model in PLAXIS 2D for the OLE condition: a) Whittier, b) Imperial Valley, and c) Superstition Hill.

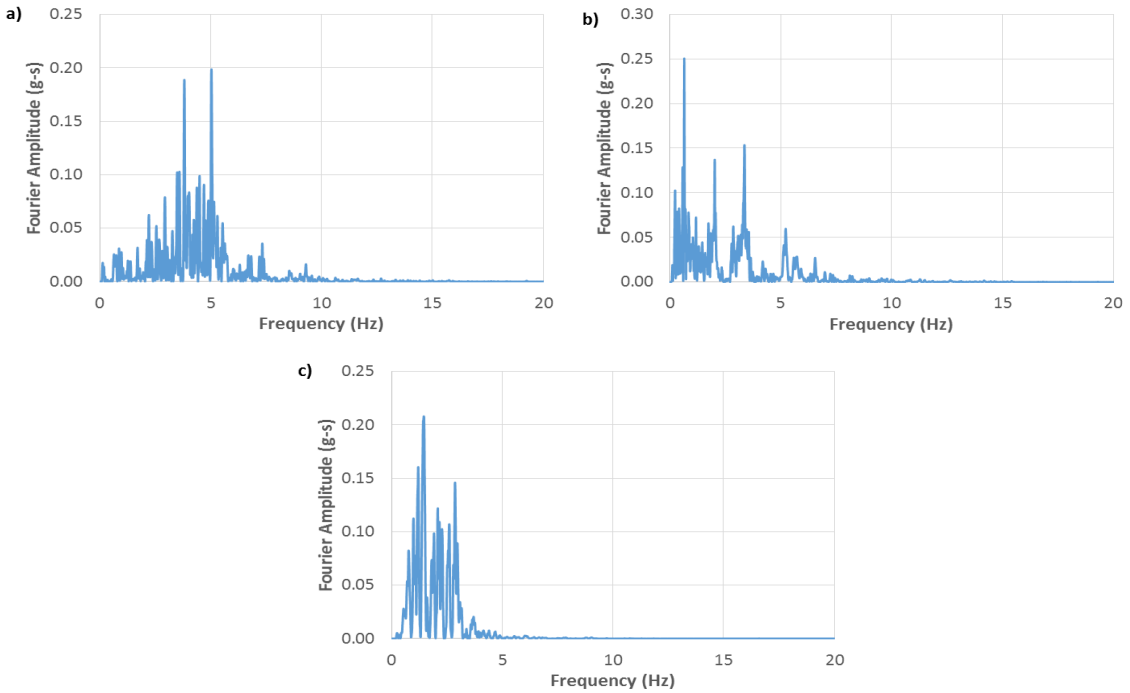

Fig. 54. Fast Fourier amplitude for a node at the bottom of the model in PLAXIS 2D for the CLE condition: a) Duzce, b) Imperial Valley, and c) Kobe.

The earthquake time histories, obtained at the outcrop of a nearby rock formation, were modeled applying a prescribed displacement at the bottom firm soil strata. It is assumed that the motion recorded at the outcrop contains waves of the same amplitude propagating upward and downward motions. The input signal is taken as half of the motion using a compliant base and from there the acceleration will propagate through the soil towards the ground surface. In order to apply a compliant base, an interface is applied at the bottom of the model, but it is not activated for all calculation phases. The strength and stiffness parameters of the interface are taken equal to those of the rock stratum. This base is included to absorb the incoming waves and create a node pair that is necessary to apply the input motion. In the bottom boundary, a value of 0.5 m assigned in the horizontal direction was the main input of the acceleration time history. In PLAXIS 2D, the dynamic load is given in terms of a dynamic multiplier by selecting the acceleration input given in units of m/s^2. To obtain this input motion, it was necessary to multiply the acceleration shown in the **Fig. 51** and **Fig. 52** by the acceleration of gravity. The files used for the input motion were obtained from the USGS and were converted to readable earthquake input files in PLAXIS. The drift correction option was selected in the program to correct potential drift in the displacement causing final non-null displacements in the signal after the earthquake finishes. This typically occurs as a consequence of the integration process of accelerations and velocities.

The peak ground acceleration of a given site can be calculated using different procedures. For those sites that have soils susceptible to liquefaction, it is preferable to perform site response analyses based on different time histories rather than simplified procedures based on site classes and soil coefficients. For the analyses presented in this research, the calculations were made based on 6 earthquakes time histories taken from the recommendations of the Port-Wide Ground Motion study for the Port of Long Beach.

5.6 Calculation of Damping Coefficients

In this project and using the computational tools and constitutive soil models, the Rayleigh damping coefficients associated to small damping ratios for the proposed soil layers are defined. The Rayleigh damping formulation is based on the definition of a damping matrix which is a function of the mass and stiffness matrices which are modified by the Rayleigh coefficients α and β. The hysteretic damping in the soil model used is able to capture damping associated with strains ranging from 10^{-4} to 10^{-2}%. The damping matrix form is defined as:

$$[C] = \alpha[M] + \beta[K] \tag{43}$$

The two coefficients α and β need to be calibrated with damping ratios and two sets of natural frequencies. The damping ratio for numerous applications is typically selected from 0.5 to 2% and is assumed to be equal for both target frequencies. These frequencies denoted in the PLAXIS input as Target 1 and 2 can be selected following the procedure by Hudson et al. (1994). The authors proposed that the first frequency Target 1 should be computed as the natural frequency of the entire soil layer while the second frequency Target 2 should correspond to the nearest odd integer from the ratio of the dominant frequency of the input motion at the bedrock or firm strata and the fundamental frequency of the entire soil layer. The natural frequency, used as Target 1 is given by the following expression:

$$f = \frac{V_S}{4H} \tag{44}$$

where V_S and H correspond to the shear wave velocity and thickness of the soil profile, respectively. In this project the shear wave velocity was selected as a weighted average value over the entire soil

profile. This shear wave velocity was computed based on the site-specific shear wave velocities from the subsurface investigation of the site. For an approximate thickness of 30 m and an average shear wave velocity of 208 m/s, the natural frequency was determined to be 1.73 Hz. The Fast Fourier Transform of the input motions was analyzed in this project and the results were presented in **Table 20**. The table presents the dominant frequency for each earthquake input as computed with PLAXIS 2D and DEEPSOIL. The average value of the dominant frequencies was in the order of 2 Hz. Therefore, the ratio of the average dominant frequency of the earthquake motions to the natural frequency of the soil profile was equal to 0.57 Hz. Thus, the frequency Target 2 was taken as 1 Hz. The physical meaning of these target frequencies is that for a frequency within that range, the resulting damping turns out to be less than the target damping ratio and outside of that range the input signal is overdamped. From the input values of the program as described before, the Rayleigh coefficients α and β were computed as 0.118 and 0.001, respectively.

5.7 Results of the Numerical Analyses

In this research, the first step is to present free-field site-specific numerical simulations of the liquefaction potential of the soils present at the POLB, Pier S. These results are further developed to include the response analyses of hypothetical infrastructure considering various buildings with several natural vibration frequencies. These analyses are presented in order to assess the detrimental settlement potential of structures when subjected to seismic forces that are capable to induce liquefaction in the subsurface soils. The main goal of these analyses is to issue recommendations related to the resulting permanent deformations and residual strength of soils which could compromise the resiliency of the port depending on the magnitude of the earthquake motion.

5.7.1 Numerical Simulations of Free-Field Conditions

As mentioned earlier in this report, the liquefaction potential of soils is often expressed using the excess pore water pressure ratio defined as r_u. This ratio at a given depth in the soil profile typically represents the development of excess pore water pressure in relation to the initial vertical effective stress. For the case of the constitutive model used in this research, the ratio r_u is given as follows:

$$r_u = 1 - \frac{\sigma'_v}{\sigma'_{v0}} \tag{45}$$

Where σ'_v and σ'_{v0} are the vertical effective stress at the end of the dynamic calculation and the initial vertical effective stress (i.e., prior to the seismic motion). A pore pressure ratio equal to one implies that liquefaction occurs which causes as a drastic reduction of the effective stresses of the soil. However, it is not necessary to reach pore pressure ratios of 1.0 to demonstrate that liquefaction occurs. Beaty and Perlea (2012) suggested that liquefaction is reached for pore pressure ratios larger than 85%. **Fig. 55** and **Fig. 56** show different pore pressure ratio contours for all the soil layers and given different time histories for both OLE and CLE contingency earthquakes from the free-field analyses presented herein. It is consistent from the results of these simulations that the second soil layer (i.e., Unit B from top to bottom corresponding to estuarine and marine deposits) is characterized by large excess pore water pressures when subjected to dynamic loading causing a drastic reduction of vertical effective stresses in the soil reaching values close to zero (i.e., liquefaction of the soil mass). This soil layer has an approximate relative density computed with Eq. (37) of 42%. Based on the cyclic strength curve shown in **Fig. 48**, a CRR value of 0.085 is needed to reach liquefaction in the soil. The OLE and CLE level earthquake conditions are capable to generate high demands of cyclic stress ratio which are above the cyclic resistance ratios. This demonstrates the liquefaction potential of these soils, especially Unit B, when subjected to the seismic demands studied in this report.

Fig. 55 shows the pore water pressure contours for the free-field simulations when subjected to the OLE conditions. The figure clearly shows r_u values larger than 85% at unit B generated due to the decrease of vertical effective stresses induced by the earthquake motions. Large values of CSR induced by the earthquakes are needed to reach liquefaction in Units A, C and D that have relative densities of 87, 57 and 92%, respectively. Even though Unit C is a medium sandy soil, other factors play an important role in the liquefaction resistance such as the overburden pressure which implies large initial vertical effective stresses making this layer less prone to liquefaction. Even for the CLE condition that produced larger CSR, the CRR of those soils due the high relative density inhibit the onset of the liquefaction. In the OLE condition shown in **Fig. 55** , the Imperial Valley and the Superstition Hill earthquakes induced larger pore water pressure ratios than the Whittier earthquake due the differences between their PGAs and frequency content. **Fig. 56** presents the same contours but for the CLE earthquake levels. In these earthquake conditions, the Kobe and Duzce earthquakes generated greater r_u values that the Imperial Valley earthquake. It is observed from the figure that

almost the entire Unit B reaches liquefaction because of the high levels of excess pore water pressures generated by the CLE earthquake demand.

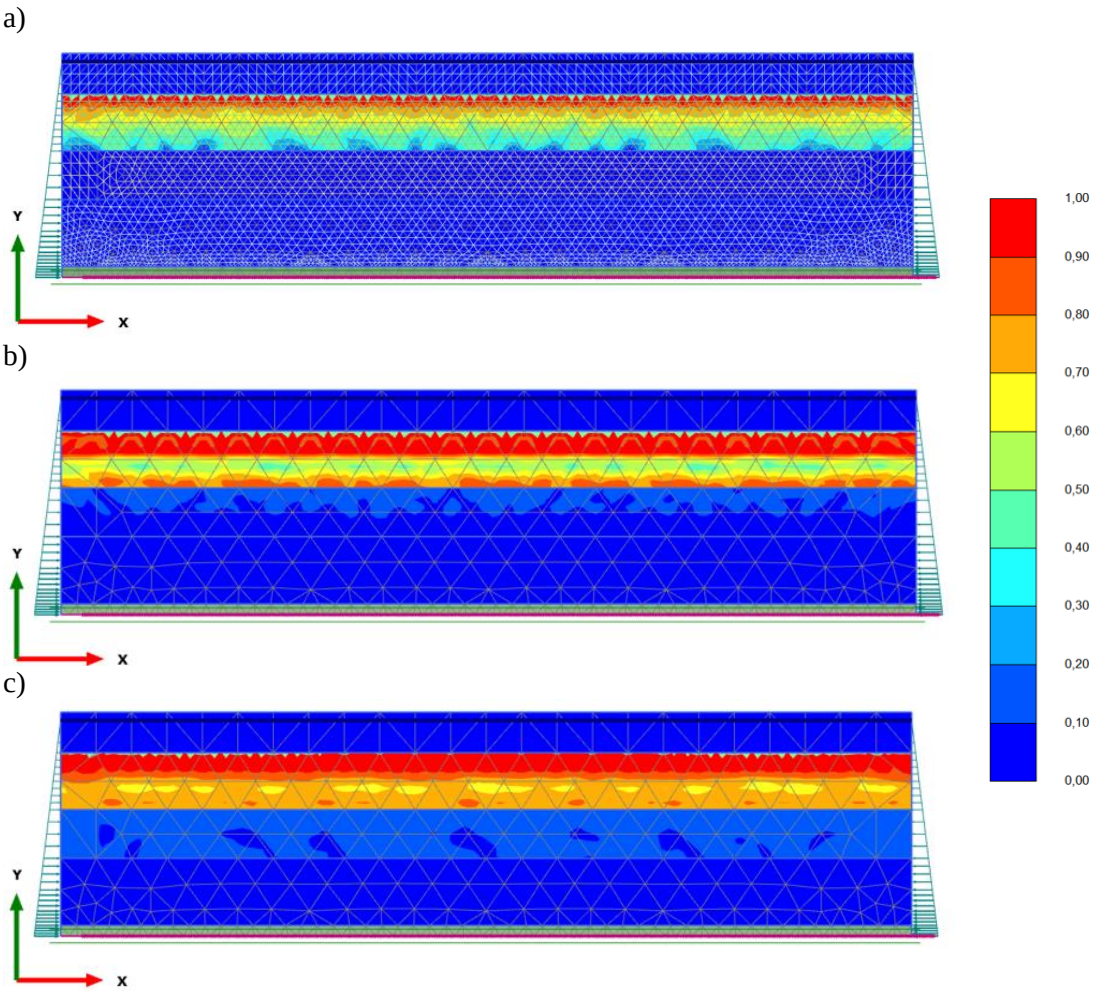

Fig. 55. Pore water pressure ratio (r_u) contours for the OLE condition a) Whittier 1987, b) Imperial Valley 1979, and c) Superstition Hill 1987.

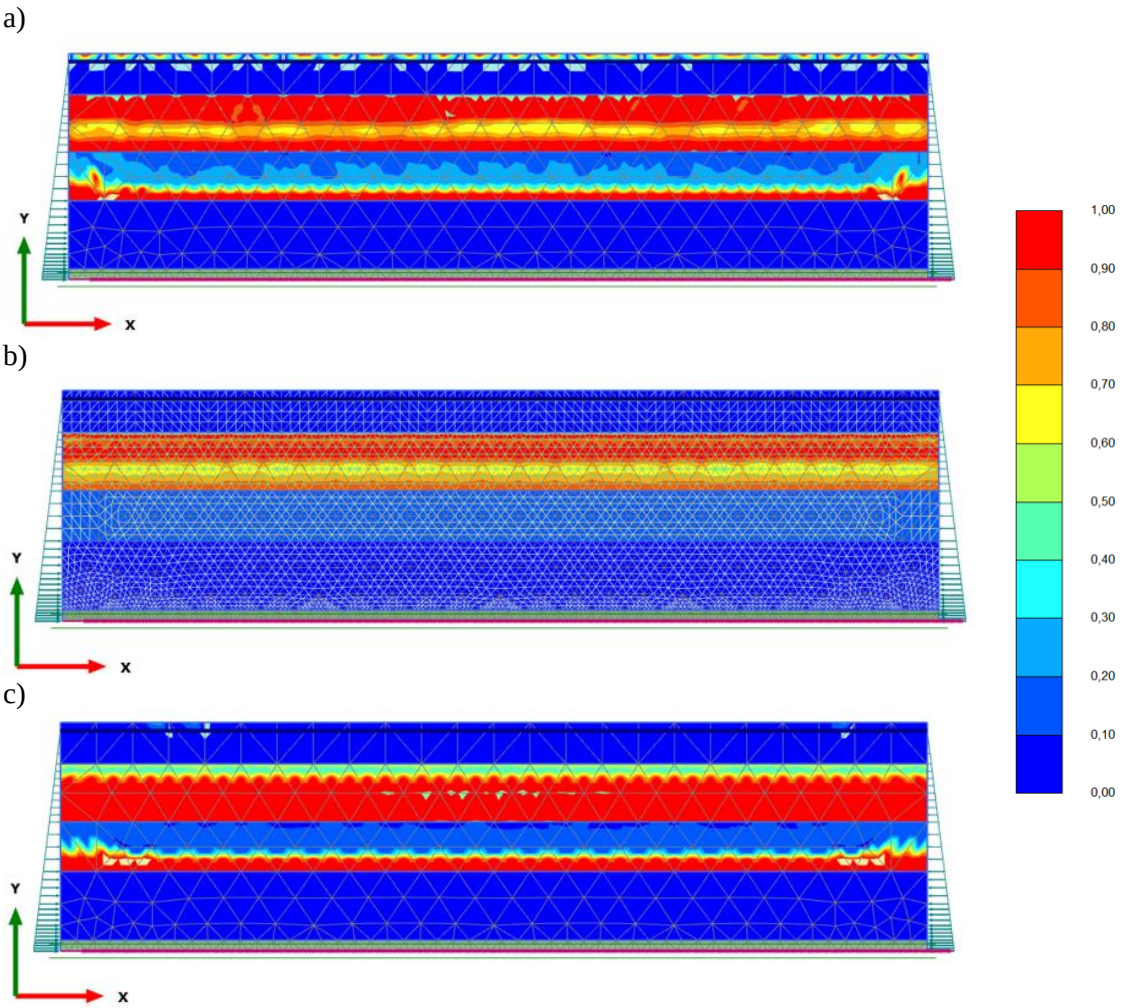

Fig. 56. Pore water pressure ratio (r_u) contours for the CLE condition a) Duzce 1999 b) Imperial Valley 1979 and c) Kobe 1995.

Fig. 57 and **Fig. 58** shows the variation of pore water pressure ratios versus time for a point taken in the middle of the liquefiable Unit B. The figure presents the results for six different earthquake time histories, three for the OLE and three for the CLE earthquake levels. It is observed that r_u values of 85% or above are developed for both conditions at that particular depth in the soil profile. These results of r_u versus dynamic time show how the pore water pressure ratios necessary to induce liquefaction are specific to the input motion. It is shown in the figure that for all the OLE earthquake levels, Whittier 1987, Imperial Valley 1979 and Superstition Hill 1987, the pore water pressure ratios reach a value higher than 85% at 30, 7 and 20 seconds after the earthquake begins, respectively. A similar result is evidenced for the CLE earthquake levels, Duzce 1999, Imperial Valley 1979 and Kobe 1995, in which r_u values larger than 85% occurs 18, 19 and 9 seconds, respectively. The initial liquefaction is reached for both conditions at a minimum of 7 seconds,

however there is no general trend on the time that liquefaction is initially induced in the soil mass depending on the earthquake. This time is specific of the input earthquake motion at the base of the model which justifies the site specific evaluation presented in this research.

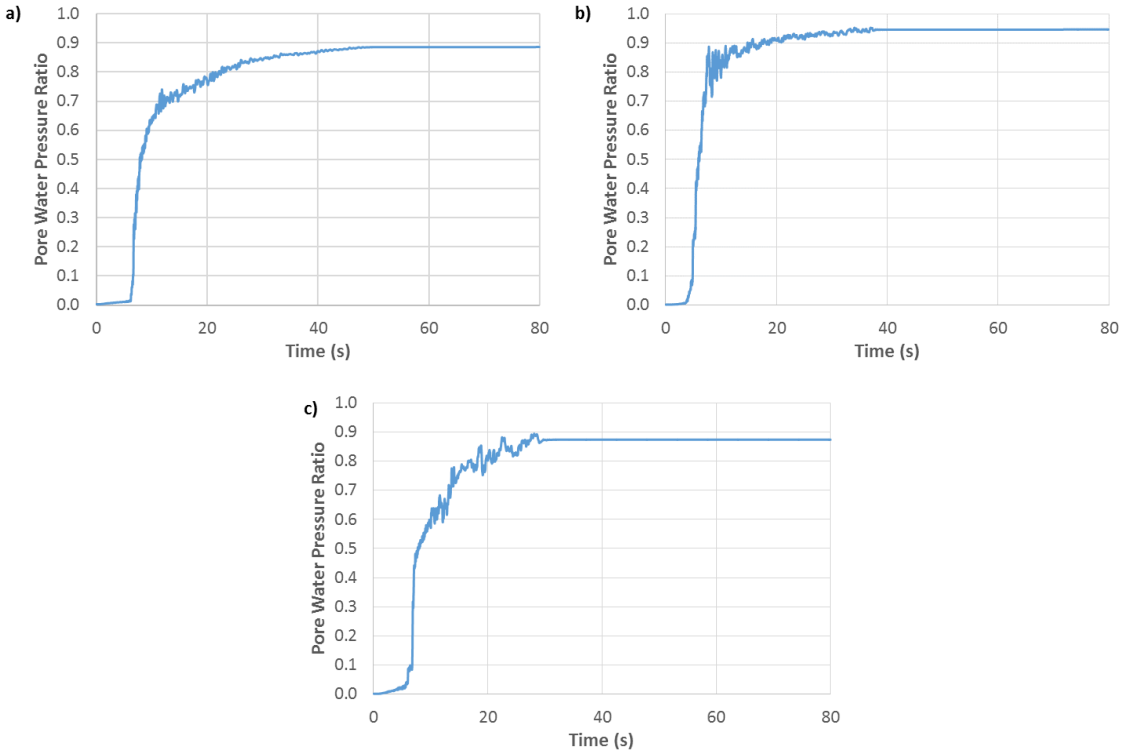

Fig. 57. Pore pressure ratio (r_u) through the dynamic time for the Unit B for the OLE conditions a) Whittier 1987, b) Imperial Valley 1979, and c) Superstition Hill 1987.

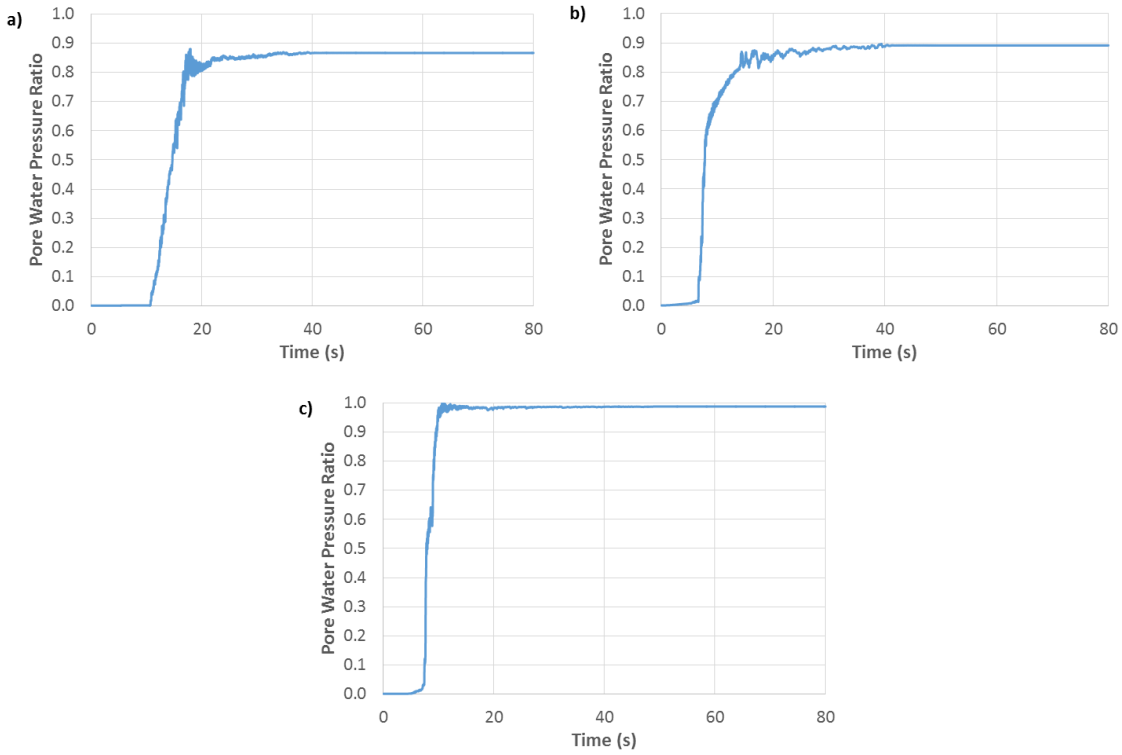

Fig. 58. Pore pressure ratio (r_u) through the dynamic time for the Unit B for the CLE conditions a) Duzce 1999, b) Imperial Valley 1979 and c) Kobe 1995.

To assess the soil behavior on a free-field condition, it is important to identify how the pore water pressure ratios develop with time for the entire model. **Fig. 59** shows the variation of the r_u through the Kobe CLE earthquake time. This earthquake was selected because it was found to be the one that induced the larger settlements between both OLE and CLE earthquake levels. These results show that at 5 seconds after the earthquake started, the vertical effective stress was reduced 50%. In addition, the figure confirms that liquefaction can be reached at a short time of 10 seconds after this particular earthquake begins.

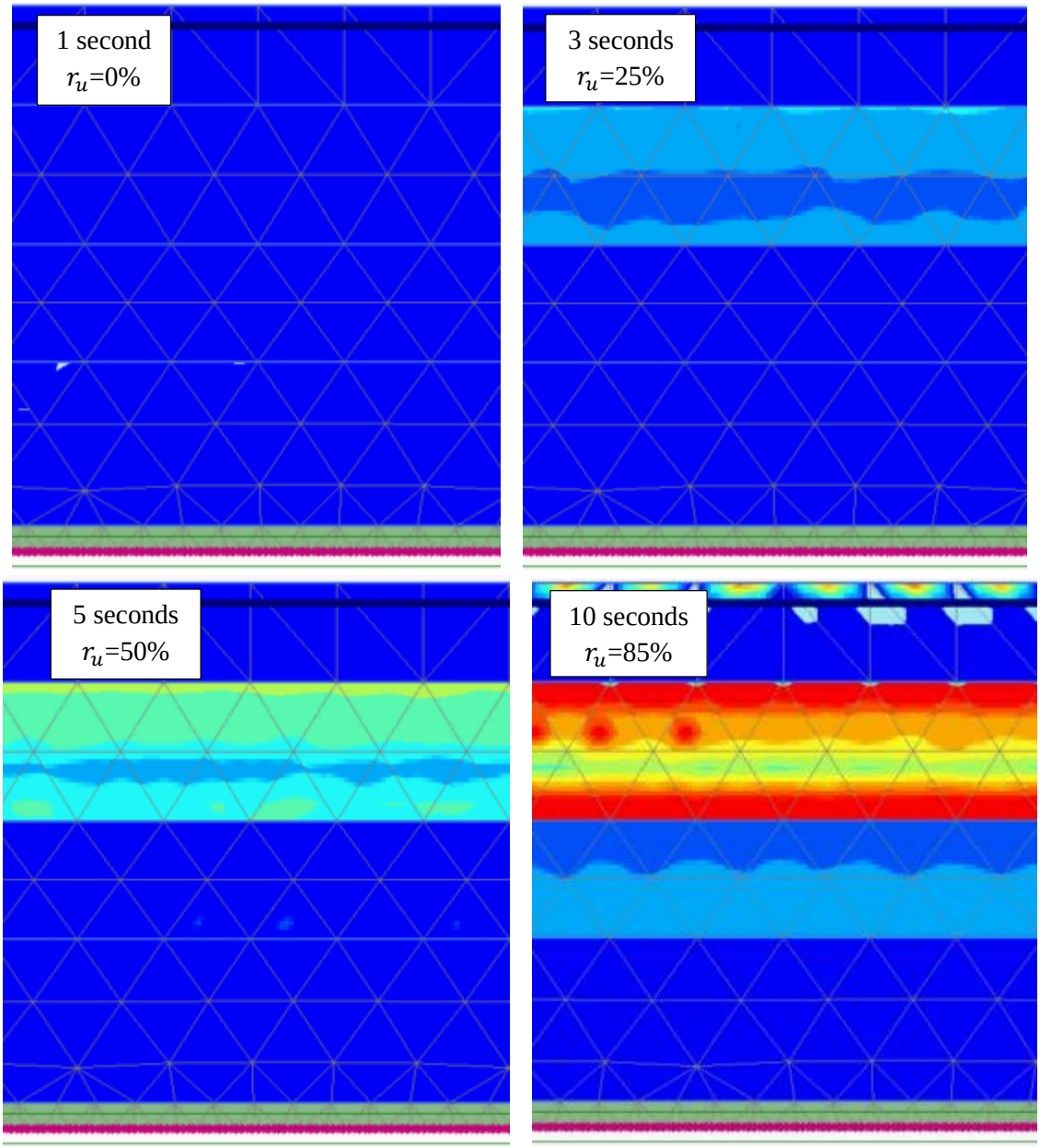

Fig. 59. Development of the pore water pressure ratio (r_u) through the Kobe CLE earthquake time.

It is important to emphasize that the numerical simulations presented in this research are performed using undrained effective stress parameters. Because of the zero change in volume assumption of undrained analyses, the program was able to only accumulate the values of pore pressure rations r_u until the end of the shaking motion with negligible vertical deformations arising from the ground motion. A final phase of pore water pressure dissipation using a consolidation stage was included in the numerical model to account for the potential settlements resulting from liquefaction, at least those corresponding to the dissipation of excess pore water pressures resulting from the earthquake.

It is important to note that those settlements are not intended to capture the post-liquefaction behavior of the soil and settlement caused by resedimentation of soil particles post-liquefaction. These results are intended to provide an estimate of the permanent deformations at the ground surface after the earthquake ends.

The maximum vertical deformation obtained from the free-field analyses for the OLE and CLE conditions are presented to show the magnitude of those settlements induced during post-liquefaction in the Unit B. The results obtained from the simulations with the OLE conditions (see **Fig. 60**) showed a maximum settlement of 18, 27 and 28 mm for the Whittier, Imperial Valley and Superstition Hill earthquakes, respectively. This complete dissipation of excess pore water pressures generated during the cyclic loading produced by the earthquake was reached after approximately 10 hours after the earthquake event. This result is expected given the large hydraulic conductivity characteristic of these alluvium deposits. The results for the CLE conditions (see **Fig. 61**) showed maximum settlements of the free-field simulations of 43, 29 and 45 mm for the Duzce, Imperial Valley and Kobe earthquakes, respectively. The variation of maximum settlements arising from the dissipation of excess pore water pressures in the post event situation are combined in **Fig. 62** for the free-field analyses. These results evidence the settlement potential induced by both earthquake levels after liquefaction is induced in the soil mass. The figure shows larger consolidation-induced settlements for the CLE than the OLE condition, which is in agreement with the PGAs induced from each condition.

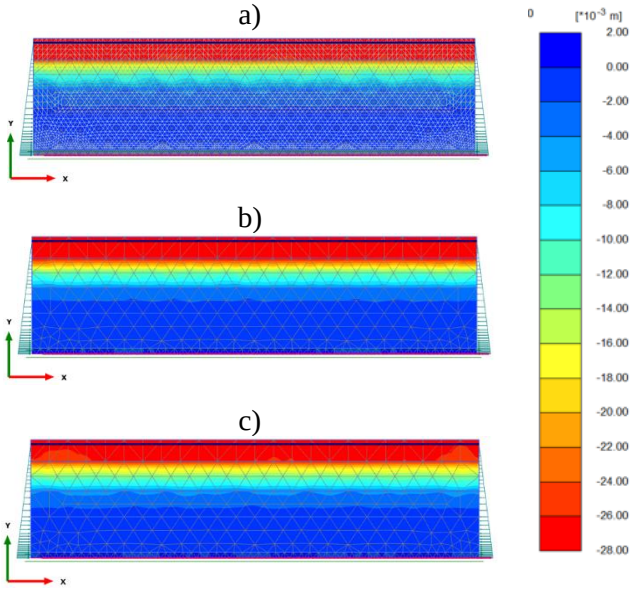

Fig. 60. Maximum vertical deformation contours for the OLE condition after the pore water pressure dissipation a) Whittier 1987, b) Imperial Valley 1979, and c) Superstition Hill 1987.

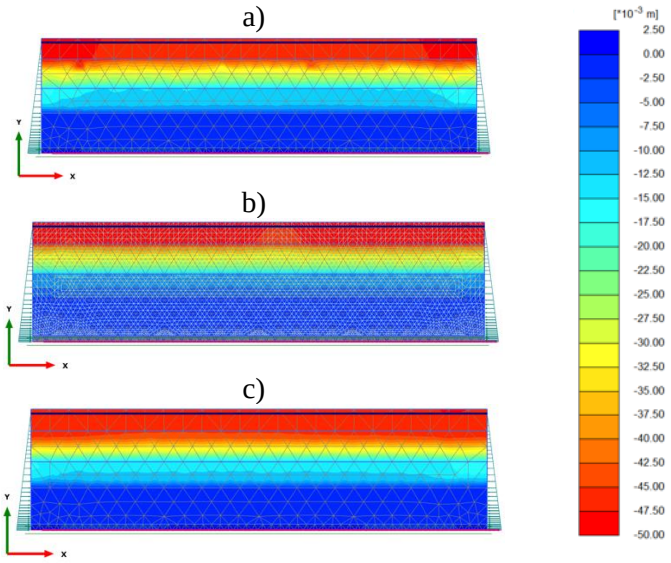

Fig. 61. Maximum vertical deformation contours for the CLE condition after the pore pressure dissipation a) Duzce 1999 b) Imperial Valley 1979 and c) Kobe 1995.

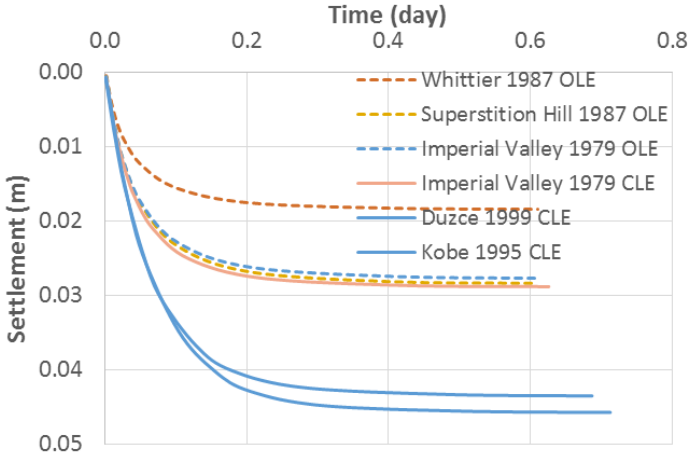

Fig. 62. Ground surface settlements arising from dissipation of excess pore water pressures after liquefaction is induced for the OLE and CLE conditions.

The results of the dynamic stress path shear-vertical effective stress are presented in **Fig. 63** and **Fig. 64** for a point in the middle of the Unit B. The figure presents for the free-field condition a stress path that resembles the stress path of a cyclic direct simple shear test. This evidences that the way the parameters were studied at the elemental scale with numerical simulations of undrained

DSS are representative of the actual stress conditions that the soils will experience in the free field. From the figure, an approximate cyclic stress ratio induced by the earthquake is about 0.21 for the OLE and 0.31 for the CLE which evidences the potential of liquefaction of that soil layer.

As discussed in section 5.3, but now using the stress path of a point in the soil mass located within Unit B, the dynamic loading in the soil tends to soften the soil response until generation of pore water pressures decreases the vertical effective stress which leads to reductions in the soil stiffness. Then, the densification rule of the model is activated, showing a slightly stiffer response before the onset of liquefaction. Computed pore pressure ratios do not reach 1.0 as shown by vertical effective stresses moving toward the left but not reaching a limiting value of zero.

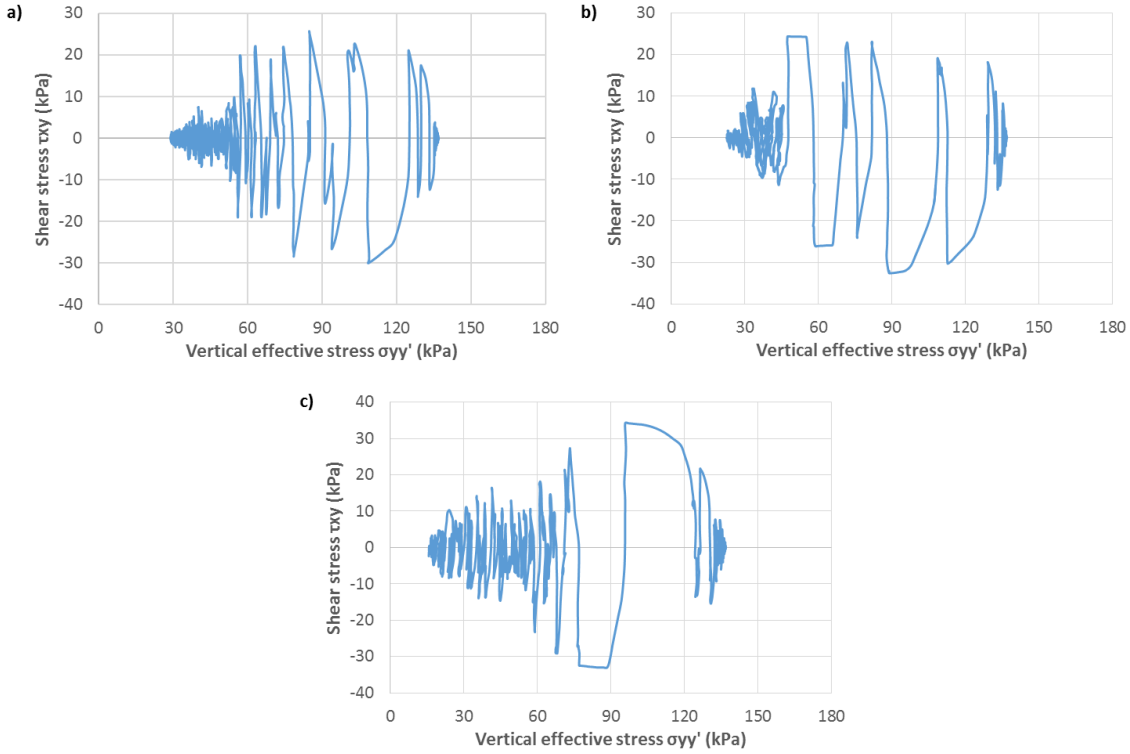

Fig. 63. Stress path for a point in the middle of Unit B for the OLE condition: a) Whittier 1987, b) Imperial Valley 1979, and c) Superstition Hill 1987.

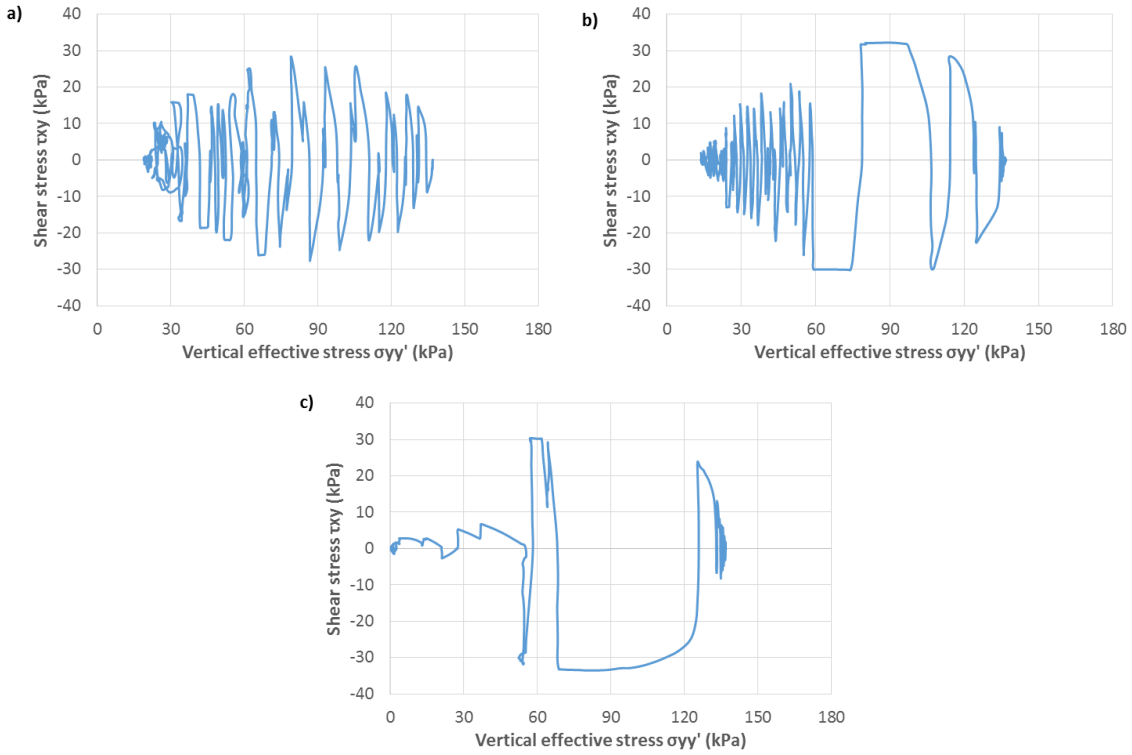

Fig. 64. Stress path for a point in the middle of Unit B for the CLE condition: a) Duzce 1999 b) Imperial Valley 1979 and c) Kobe 1995.

The mobilized shear strength before and after the earthquake can also be used to quantify the detrimental effects that liquefaction has in these soils. PLAXIS 2D computes the relative shear stresses of the soil, as follows:

$$\tau_{relative} = \frac{\tau_{mobilized}}{\tau_{maximum}} \tag{46}$$

where $\tau_{relative}$ represents the relative shear stress ratio that adopts values between 0 and 1. When $\tau_{relative}$ is equal to one, the soil reached failure based on the Mohr-Coulomb failure criterion adopted in the model, which implies that the shear strength of the soil has been fully mobilized. The maximum shear stress is defined as:

$$\tau_{maximum} = c' + \sigma'_0 \tan \phi' \tag{47}$$

Thus, for Unit B and for two different earthquake input motions, **Fig. 65** shows for the free-field analyses using OLE and CLE conditions that high values of shear strength mobilized in the order

of 70% of the shear strength from a Mohr-Coulomb standpoint. This is shown for most of the soil profile. Also, Unit B presents larger values close to one indicating that the CLE conditions in these analyses are capable to fully mobilize almost the entire shear strength of the soil within that unit.

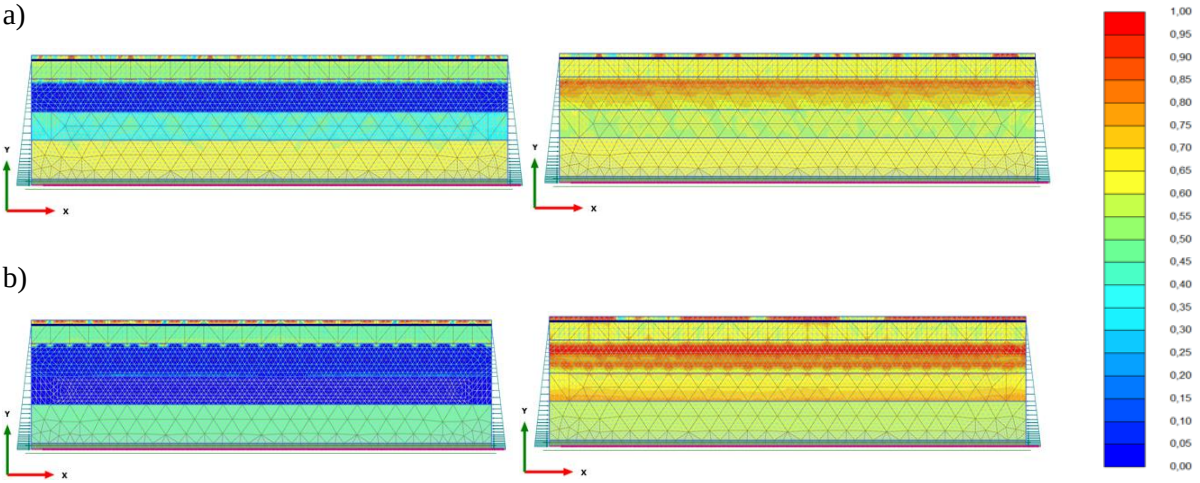

Fig. 65. Relative shear stress ($\tau_{relative}$) contours due to the earthquake motions after pore water pressures dissipation stages: a) Whittier 1987 (OLE) and b) Imperial Valley 1979 (CLE).

Fig. 66 and **Fig. 67** shows the predominant frequency for each earthquake motion computed with PLAXIS 2D and DEEPSOIL applying an FFT of the acceleration time history output for a point located close to the ground surface. From these figures, it is possible to conclude about the possible frequency content of the output signal at the top of the ground surface which could be harmful to future structures on shallow foundations and utilities. A summary of predominant frequencies for earthquakes at the OLE and CLE levels are shown in **Table 21** and comparisons between the results obtained with PLAXIS 2D and DEEPSOIL are presented.

Table 21. Predominant frequencies of the earthquakes for OLE and CLE conditions for points close to the ground surface.

Earthquake	EQ Freq. (Hz) PLAXIS	EQ Freq. (Hz) DEEPSOIL
Whittier OLE	1.69	1.69
Imperial Valley OLE	1.8	1.8
Superstition Hill OLE	1.46	1.47
Duzce CLE	1.64	1.61
Imperial Valley CLE	1.46	1.27
Kobe CLE	1.14	1.17

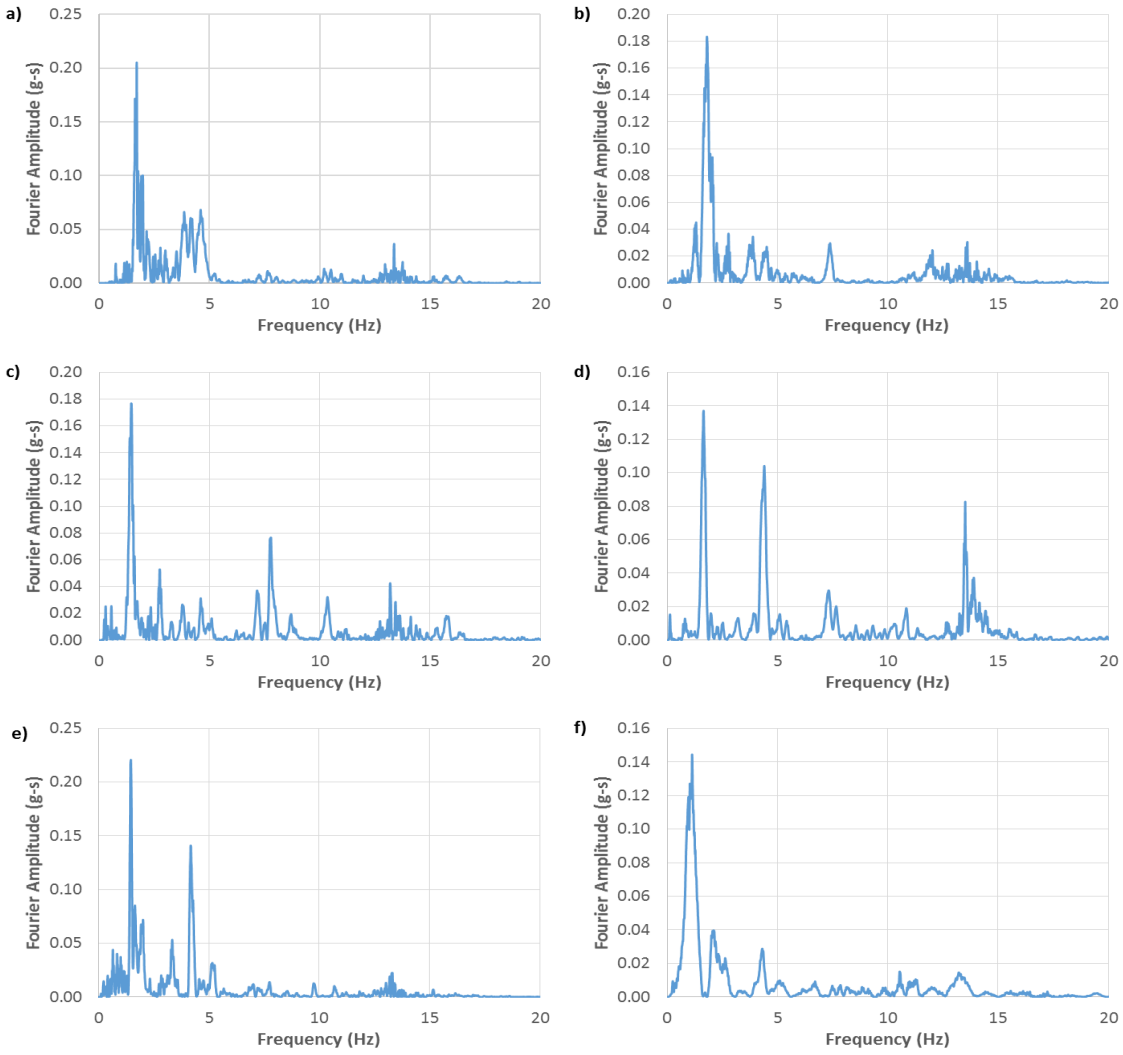

Fig. 66. Fast Fourier amplitude at the top ground surface with PLAXIS 2D for the OLE condition a) Whittier 1987, b) Imperial Valley 1979, c) Superstition Hill 1987 and CLE condition d) Duzce 1999 e) Imperial Valley 1979 and f) Kobe 1995.

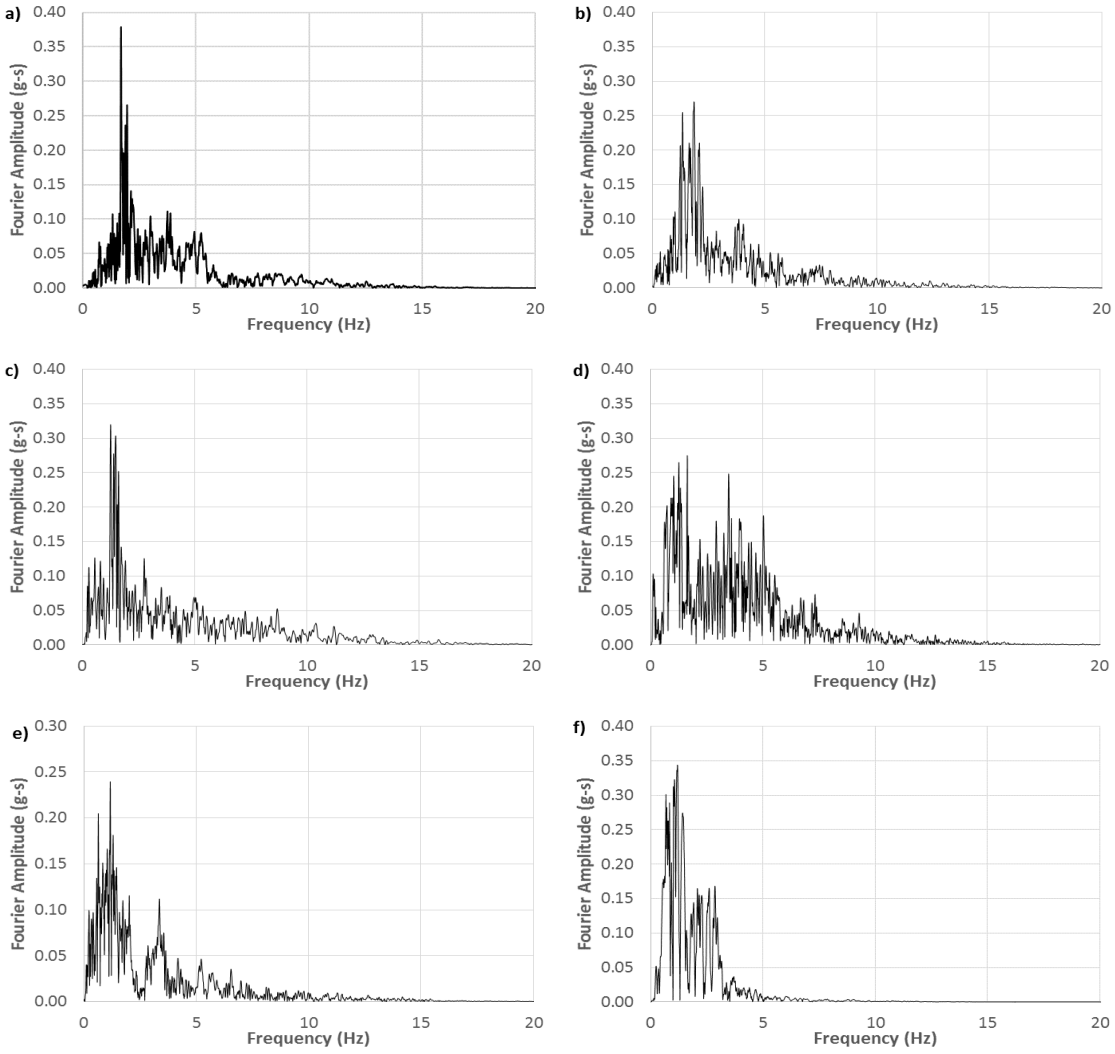

Fig. 67. Fast Fourier amplitude at the top ground surface with DEEPSOIL for the OLE condition a) Whittier 1987, b) Imperial Valley 1979, c) Superstition Hill 1987 and CLE condition d) Duzce 1999 e) Imperial Valley 1979 and f) Kobe 1995.

In these analyses, slight differences between the calculated predominant frequencies with PLAXIS 2D and DEEPSOIL were observed. It is shown that the results of both programs reasonably match even considering their differences in the way soil damping and stiffness degradation are accounted for in both programs.

The acceleration response spectra at the top of the ground surface for both earthquake conditions levels is presented in **Fig. 68**. The figure shows the comparison between the acceleration response spectra obtained with PLAXIS 2D and the suggested by the POLB ground motion report. It is observed that the acceleration response spectra for the both earthquake level conditions

recommended by the Port Wide Ground Motion study POLB by Earth Mechanics Inc (2006) are reasonable envelopes for the input histories selected in this research. It was found that the PGA for all earthquakes are bounded between the OLE and CLE spectra proposed by the Port Wide Ground Motion study. The PGA values of the OLE and CLE conditions were determined from the Port Wide Ground Motion study POLB (2006) taking into account several plausible earthquakes around the POLB.

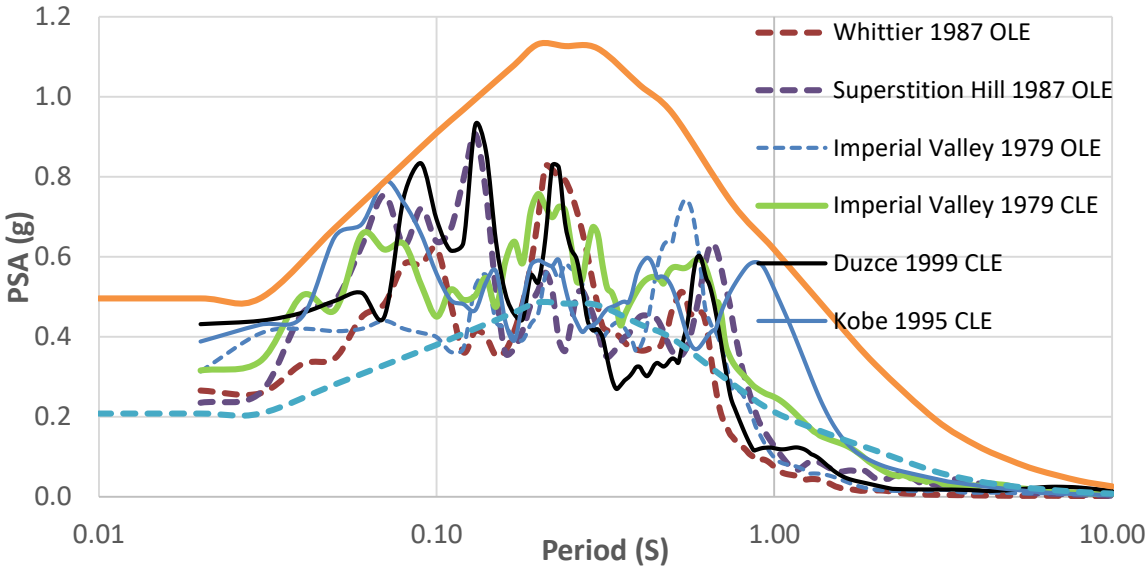

Fig. 68. Acceleration response spectra at the top of the ground surface with PLAXIS 2D for the OLE and CLE conditions.

To verify the results computed with PLAXIS 2D, acceleration response spectra were also calculated with the software DEEPSOIL close to the ground surface. **Fig. 69** shows the comparison between the acceleration response spectra obtained with DEEPSOIL and the suggested by the POLB ground motion report. Again, it is observed that the acceleration response spectra recommended by the Port Wide Ground motion study of the POLB by Earth Mechanics Inc. (2006) represent minimum and maximum boundaries for the OLE and CLE conditions, respectively. Even with slight differences in the computed PSA, the response spectra obtained with DEEPSOIL reasonably match those computed with PLAXIS 2D.

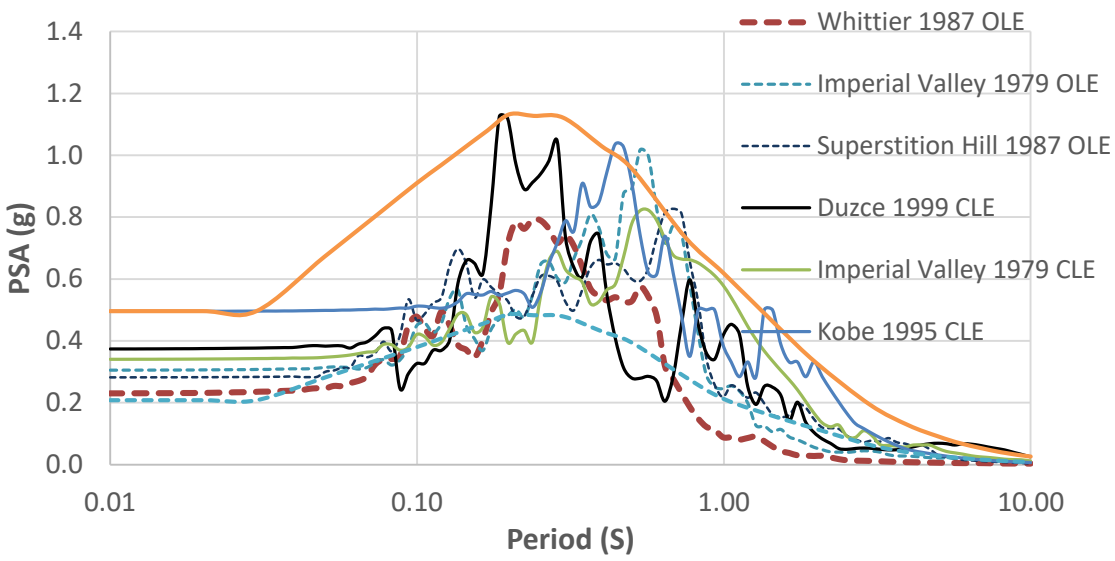

Fig. 69. Acceleration response spectra at the top of the ground surface with DEEPSOIL for the OLE and CLE conditions.

5.7.2 Numerical Simulations of Hypothetical Structures

One of the objectives of this research is to assess the detrimental effects that the combination of these level earthquakes and soil conditions would have in the functionally of the POLB, Pier S. To achieve this goal, it is proposed to numerically simulate the potential post-liquefaction effects in the overall response of various types of hypothetical structures when an earthquake induces liquefaction in the soil deposit, using the computational finite element package PLAXIS 2D. At this point, it has been shown that the onset of liquefaction of Unit B is not only captured by the numerical model and verified with semi-empirical approaches, but also plausible if earthquake levels like the ones presented herein occur. **Fig. 70** shows the computed vibration modes of a hypothetical two-bay two-story structure placed on a shallow foundation. At least, 3 different vibration modes of the structure can be identified but the natural and principal dominant frequency of the building is 1.8 Hz. The building is an 8-m tall structure consisting of two stories and one basement level. In the seismic response analyses presented herein, the building was modeled with a basement level to avoid unnecessary and unrealistic over predictions of the resulting total settlements under the structure when placed directly on top of the ground surface. The structure has a footprint of 8 m wide in one direction and a very large magnitude in the perpendicular direction as the structure is modeled in plane strain conditions. It was assumed a value of 5 kN/m^2 for the weight of the floors and walls. The structure is assumed to be founded on shallow foundations. This condition was chosen for the hypothetical structure because this is the worst-case scenario for the

settlements induced by an earthquake. Therefore, any lateral spreading effects or any other mechanism inherent to deep foundations are not included in this study. This hypothetical structure type, size, and configuration was selected to approximately match a dominant frequency of about 1.72 Hz calculated for the soil profile with Eq. (35) using a shear wave velocity approximately equal to 208 m/s.

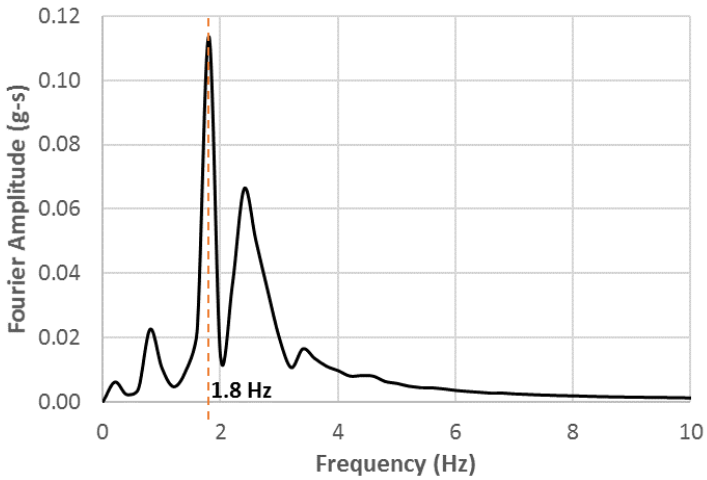

Fig. 70. Fast Fourier amplitude for the 2-story structure with a basement level using PLAXIS 2D.

Liquefaction-induced settlements caused by the development of excess pore water pressures may affect structures founded over saturated granular soil deposits, causing partial or total collapse, especially if there is significant differential settlement between adjacent structural elements. **Table 22** summarizes the maximum vertical deformations obtained for the 2-story hypothetical structure subjected to the OLE and CLE earthquake levels. The liquefaction-induced deformations and those arising from the dissipation of excess pore water pressures after the earthquake are presented for the six earthquakes presented in this research. The results obtained from the numerical simulations with the OLE conditions showed a maximum total settlement varying from 10 to 15 cm for the Whittier and Imperial Valley (OLE) earthquakes, respectively. The results for the CLE conditions showed maximum total settlements varying from 14 to 18 cm for the Duzce and Imperial Valley (CLE) earthquakes, respectively. **Fig. 71** and **Fig. 72** show the variation of vertical deformation at the ground surface versus time as the earthquake is induced and during the pore water pressure dissipation phase for both earthquake level conditions. Based on typical hydraulic conductivities of the alluvium deposits characteristics of this site, it is only 3 hours after the earthquake that the soil fully dissipates the pore water pressures and settlements are caused on the ground surface.

The cases histories proposed by Yoshimi and Tokimatsu (1977); Arulmoli et al. (1992); Liu and Dobry (1997); and Hausler (2002) of buildings with 2 to 4 stories founded on shallow foundations on saturated granular soils suggested that most of the total liquefaction-induced settlements were caused during the earthquake motion with minor contribution arising from dissipation of the excess pore water pressure generated during the cyclic loading. This observation from numerous case histories is confirmed in this research as summarized in **Table 22**. The largest values of settlements for this two-story structure occurred during the dynamic phase and not necessarily during the post-earthquake consolidation of soils. This consolidation is highly influenced by soil resedimentation, which is not captured by the constitutive model used in this research, and in fact is a general limitation of most plasticity-based models currently used for soil liquefaction. More and better numerical models to solve these inconsistencies are being proposed in the technical literature with very promising results to improve the predicting capabilities in geotechnical engineering when dealing with liquefiable soils.

Table 22. Summary of settlements for each phase in the numerical simulations of a 2-story structure with a basement level when subjected to the OLE and CLE levels.

Type of analysis	**Earthquake**	**Dynamic Phase (1) (m)**	**Dissipation of PWP Phase (2) (m)**	**Total (1) + (2), (m)**
2-story Building	Whittier OLE	0.069	0.031	0.100
	Imperial Valley OLE	0.110	0.038	0.151
	Superstition Hill OLE	0.079	0.035	0.114
	Duzce CLE	0.091	0.050	0.141
	Imperial Valley CLE	0.143	0.041	0.184
	Kobe CLE	0.118	0.048	0.166

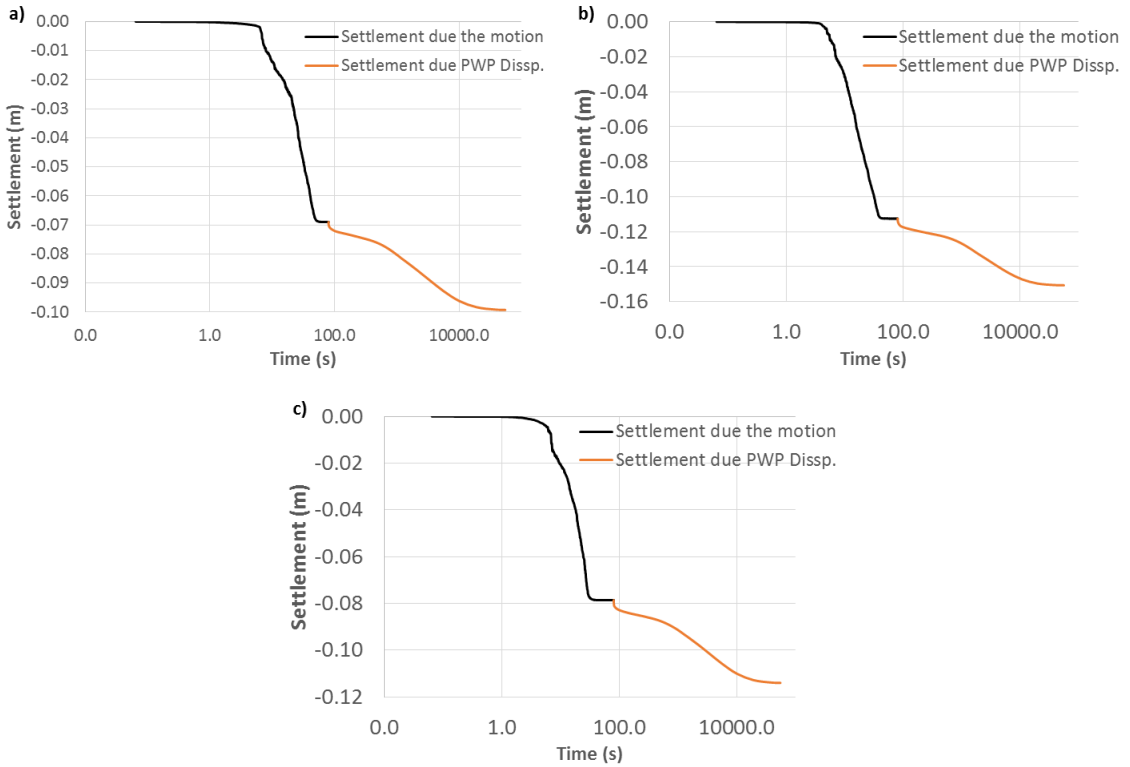

Fig. 71. Development of ground surface settlements versus time as induced during the earthquake and during the pore water pressure dissipation phase for OLE condition: a) Whittier 1987, b) Imperial Valley 1979, and c) Superstition Hill 1987.

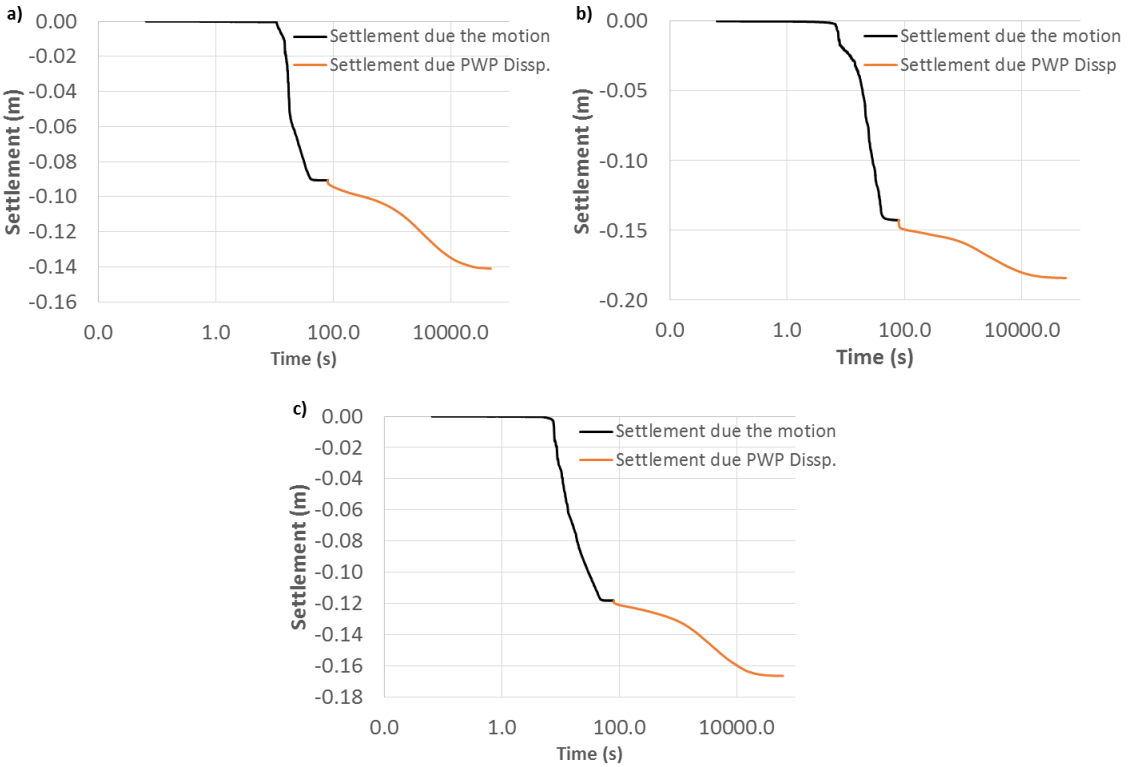

Fig. 72. Development of ground surface settlements versus time as induced during the earthquake and during the pore water pressure dissipation phase for CLE condition: a) Duzce 1999 b) Imperial Valley 1979, and c) Kobe 1995.

Fig. 73 and **Fig. 74** present the pore water pressure ratio contours at the end of the earthquake for the CLE and OLE conditions. These results evidence that almost the entire Unit B reaches $r_u$values of 85% or more for both earthquake levels. The input motions in these analyses are the same as the ones used for the free-field simulations, and even though the mechanisms that lead to liquefaction of the soil profile are similar, the effects are manifested in a different manner here causing large settlements to hypothetical structures. In these analyses, larger excess pore water pressures were generated under the structure with respect to those developed for the free-field cases. The presence of a structure with these characteristics increases the vertical ground deformations as the weight of the structure mobilizes part of the soil shear strength before the earthquake strikes.

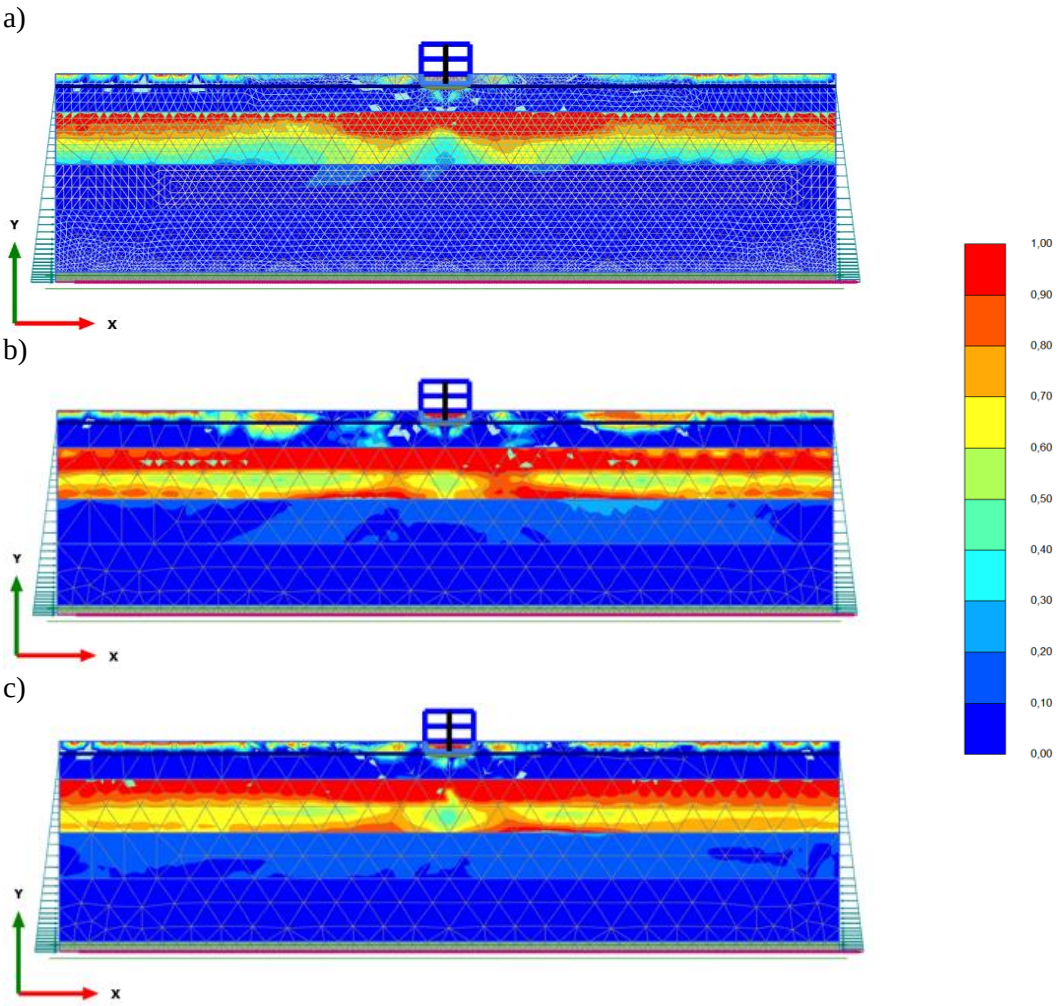

Fig. 73. Pore water pressure ratio (r_u) contours for a site supporting a 2-story hypothetical structure when subjected to the OLE conditions: a) Whittier 1987, b) Imperial Valley 1979, and c) Superstition Hill 1987.

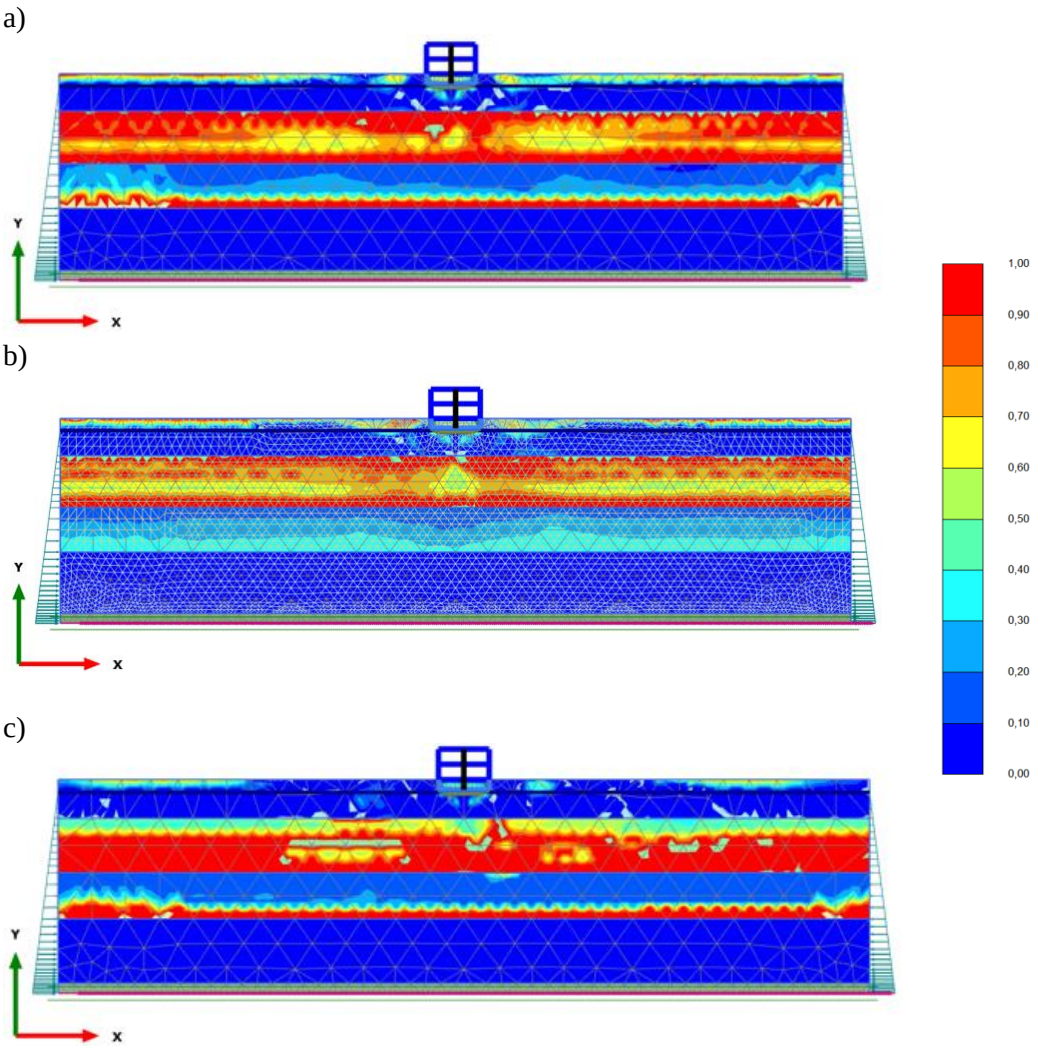

Fig. 74. Pore water pressure ratio (r_u) contours for a site supporting a 2-story hypothetical structure when subjected to the CLE conditions: a) Duzce 1999 b) Imperial Valley 1979, and c) Kobe 1995.

Fig. 75 and **Fig. 76** present the relative shear stress contours mobilized by both earthquake levels. The figures show that for Unit B, the high development of earthquake-induced shear stresses fully mobilized the soil shear strength, particularly in the zones located below the structure. This is evidenced with the high relative shear stress values close to or equal to one. Even though Unit A also presents high shear stress values, those stresses are not strictly related to soil liquefaction now that the pore water pressure ratios, as shown in **Fig. 73** and **Fig. 74**, are not large enough to induce liquefaction. It is noted that because of the relatively small vertical effective and confining stresses of that surficial soil layer, larger relative shear stresses of the soil are expected. It also noted that

the Imperial Valley and Superstition Hill (OLE) earthquakes have larger relative shear stress zones equal or close to 1 with respect to those developed for the Whittier earthquake, which matches the free-field settlement results presented in this section in which the Imperial Valley (OLE) induced more settlements than the other two OLE earthquakes.

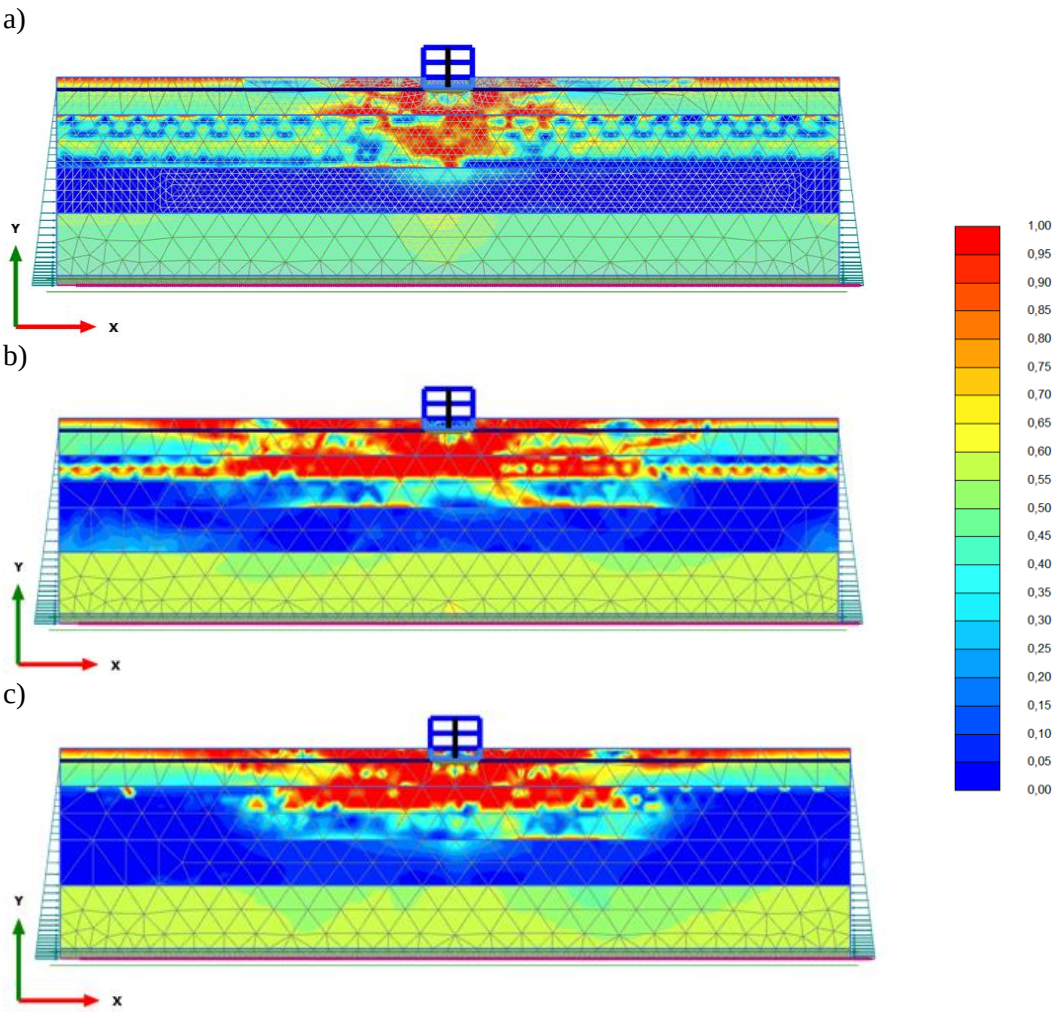

Fig. 75. Relative shear stress ($\tau_{relative}$) contours for a site supporting a 2-story hypothetical structure when subjected to the OLE conditions: a) Whittier 1987, b) Imperial Valley 1979, and c) Superstition Hill 1987.

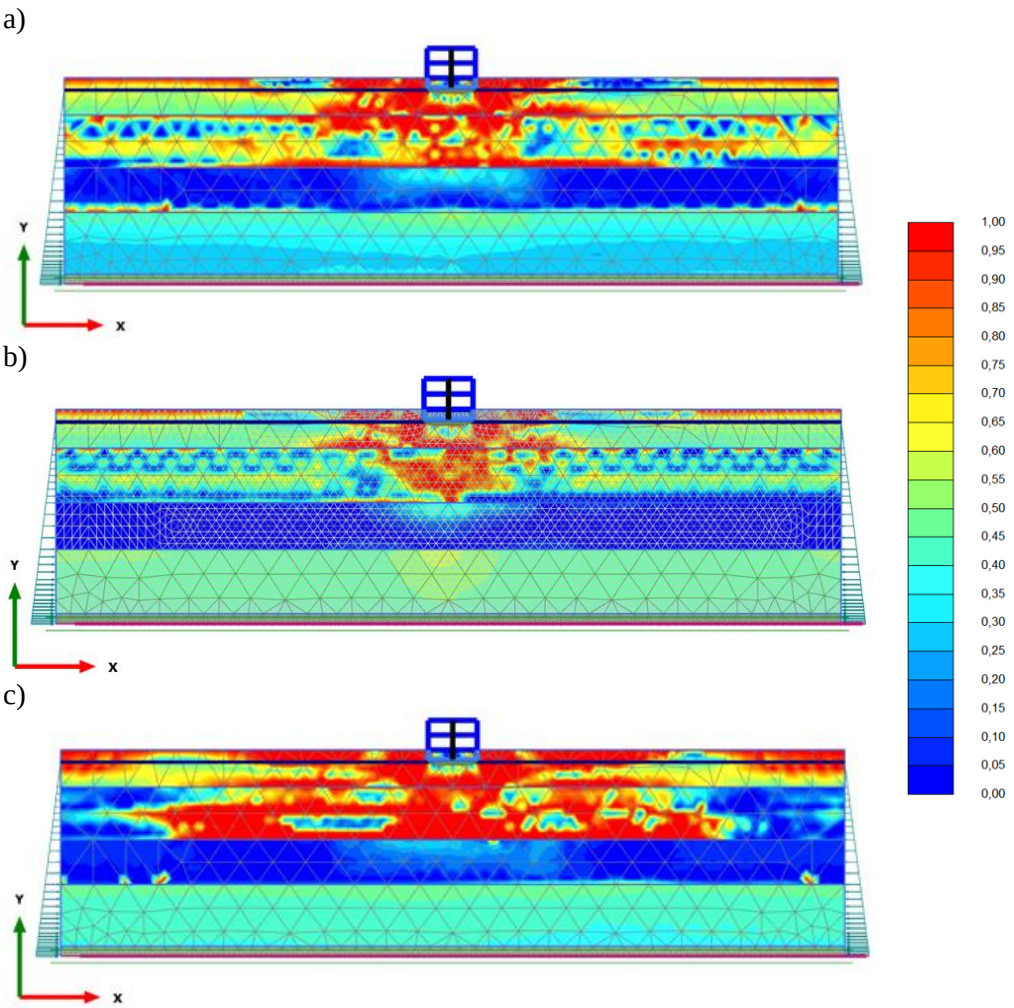

Fig. 76. Relative shear stress ($\tau_{relative}$) contours for a site supporting a 2-story hypothetical structure when subjected to the CLE conditions: a) Duzce 1999 b) Imperial Valley 1979, and c) Kobe 1995.

Fig. 77 shows the total volumetric strain contours for the both earthquake levels. The figures show that the largest earthquake-induced volumetric strains occur in Unit B. However, those magnitudes, which are in the order of 0.1% are considered small quantities. This trend was found in all the earthquakes analyzed. The liquefaction induced-settlements below the hypothetical structures do not correspond to a purely volumetric strain mechanism but contribute to the total deformations.

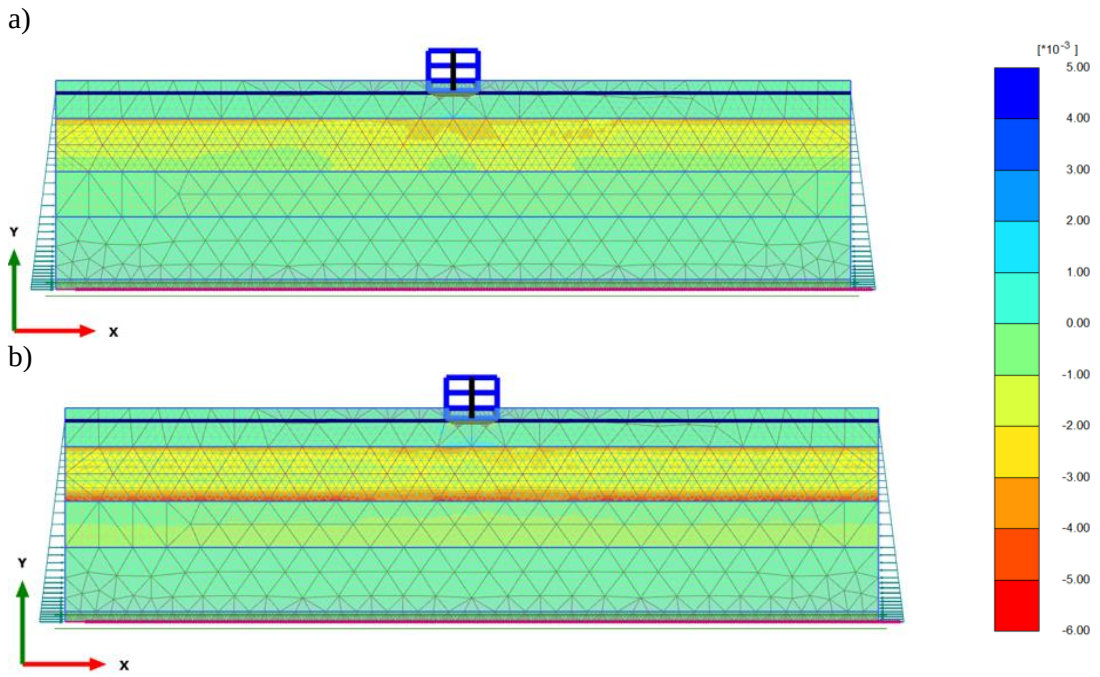

Fig. 77. Contours of volumetric strains (ε_v) for the project site supporting a 2-story hypothetical structure and subjected to: a) Whittier 1987 (OLE) and b) Imperial Valley 1979 (CLE).

To analyze the settlement mechanisms of the proposed hypothetical structures in shallow foundations, different structural configurations were analyzed by varying the amount of stories. The analyses were developed for hypothetical buildings with 1, 2, and 3 stories with one basement level, with the objective to assess the effect that the proximity of the predominant frequency of the structure to the dominant frequency of the earthquake will have in the resulting liquefaction-induced settlements. Even though, the mechanisms computed herein are not intended to quantify distortions or differential settlements, these large earthquake demands are capable of generating large settlements that could potentially lead to the partial or total collapse of these hypothetical structures. Three main mechanisms have been identified in the deformation of structures in shallow foundations on liquefiable soils (Dashti and Bray 2013): i) the volumetric strains caused by the water flow in response to transient gradients, ii) partial bearing capacity failure as a result of soil softening, and iii) settlement-induced building ratcheting during earthquake loading.

The deformed mesh corresponding to the Imperial Valley CLE earthquake is presented in the **Fig. 78**. These results are presented for 1, 2, and 3 story hypothetical structures including one basement level. This earthquake is the only one presented because it induced the largest amount settlements. The successful performance of the building is quantified in terms of liquefaction induced-

settlements, being the 3-story structure the one that developed the highest values of ground settlement. The author of this research observed cautiously videos (available upon request) of the deformations of the buildings as the earthquakes occurred and confirmed that they first experienced soil-structure interaction deviatoric ratcheting followed by a bearing capacity failure of the foundation. These mechanisms occurred mainly because of soil softening and are similar to the primary liquefaction-induced displacement mechanisms shown in **Fig. 15**.

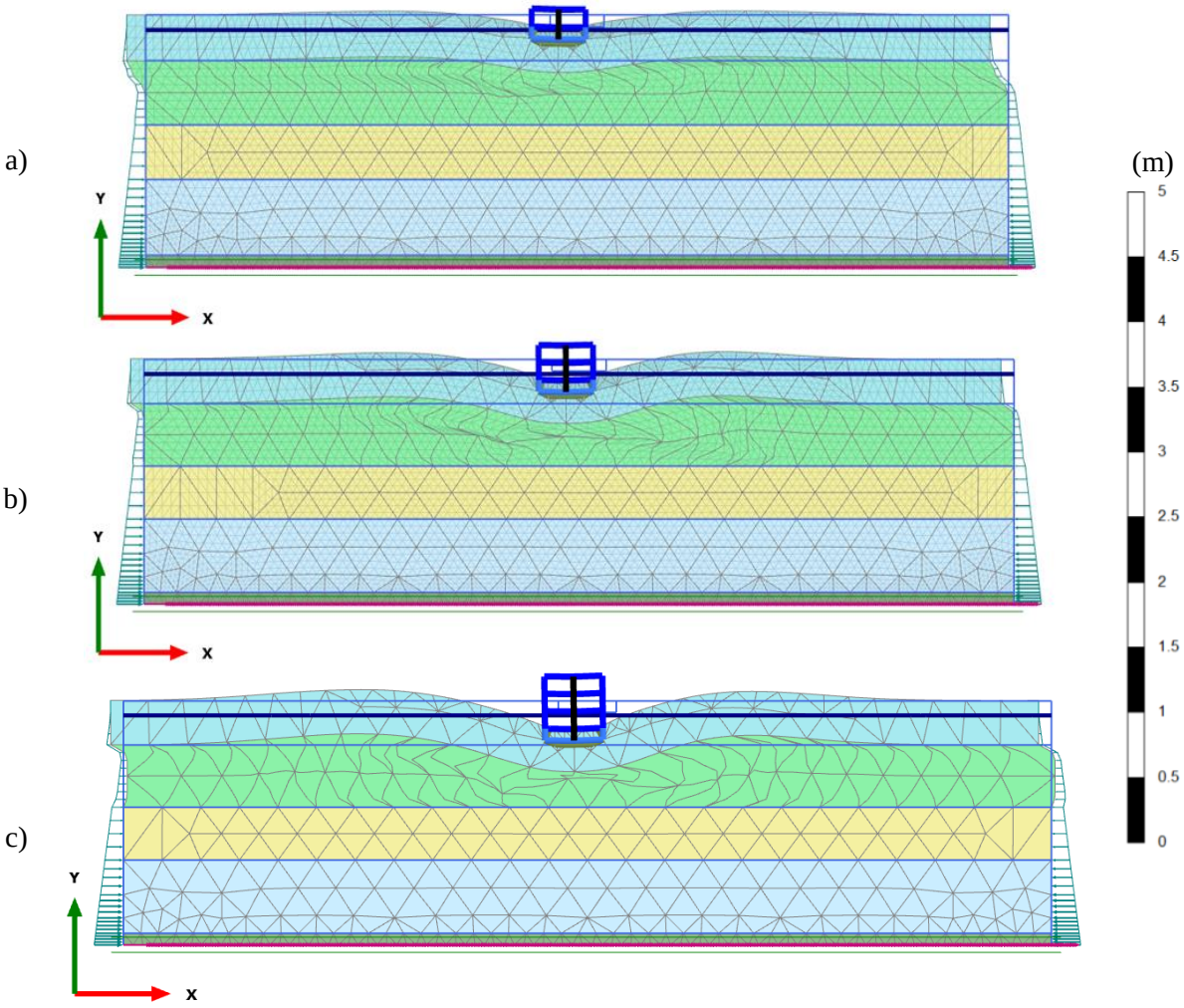

Fig. 78. Deformation contours for different hypothetical structure types including one basement level when subjected to the Imperial Valley CLE earthquake: a) 1-story structure, b) 2-story structure, and c) 3-story structure.

Fig. 79 shows the deformation contours through the dynamic time for the Imperial Valley CLE earthquake only for the hypothetical 3-story structure with one basement level. This figure confirms that the principal settlement mechanism of the building is manifested as a building ratcheting

followed by a bearing capacity failure. The application of the Imperial Valley CLE earthquake at the base of the model, results in loss of strength of Unit B and causes large settlements of the structure 20 seconds after the earthquake started. Before this punching-type failure mechanism, soil-structure interaction-induced deviatoric building ratcheting occurred. This ratcheting causes some zones underneath the structure to variable cycles of compression and tension. Unit A is a layer with relatively large initial relative density that exhibits some resistance to develop seismically-induced excess pore water pressures which might cause soil stiffness degradation. Hence, settlements are mostly due to loss of strength of soils present at Unit B.

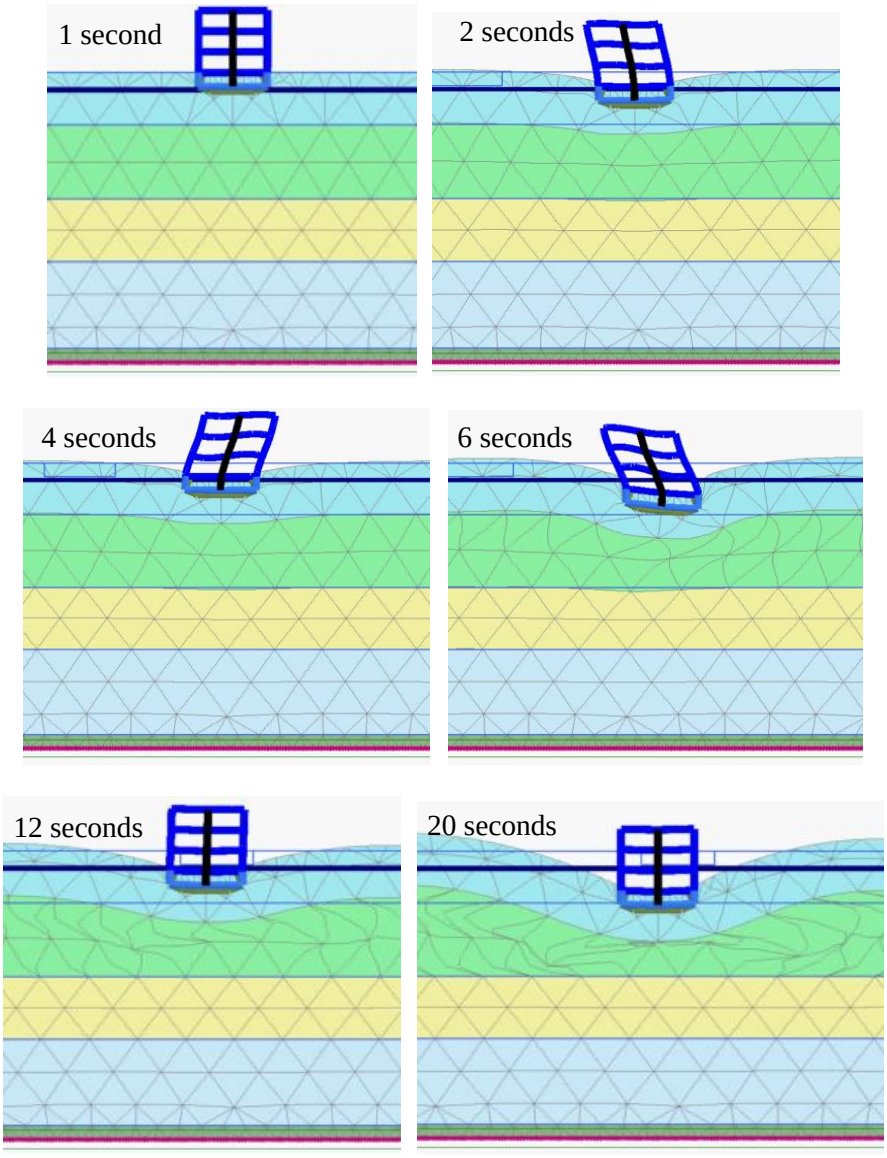

Fig. 79. Deformation contours of hypothetical 3-story structure for different times during the Imperial Valley CLE earthquake.

Fig. 80 summarizes the total maximum post-liquefaction settlements computed for different earthquakes and varying the number of stories. A progressive increase of settlements was observed as the number of stories increased. The results show that the earthquakes that induced the largest settlements for a 1-story structure was the Kobe (CLE), for a 2-story structure was the Imperial Valley (CLE) and for a 3-story structure was the Imperial Valley (OLE) earthquakes, which is consistent with the previous analyses reported for the free-field conditions. Conversely, the earthquake that produced the lowest settlements regardless of the number of stories was the Whittier (OLE) earthquake. Even though the majority of the results reasonably match the expected behavior of larger settlements for taller structures, the problem is dependent on numerous other factors such as the frequency content of the input motion, amplification of the seismic waves as they propagate upward through the soil profile, and strength and stiffness reduction (softening) of the soil as the earthquake occurs. Research on structural damage caused by soil liquefaction is still subject of numerous efforts and more research is needed about those effects on structural and non-structural components of buildings. This complexity is reflected also in the large scatter in the computation of settlements using the classical approaches as presented in Section 4.5.

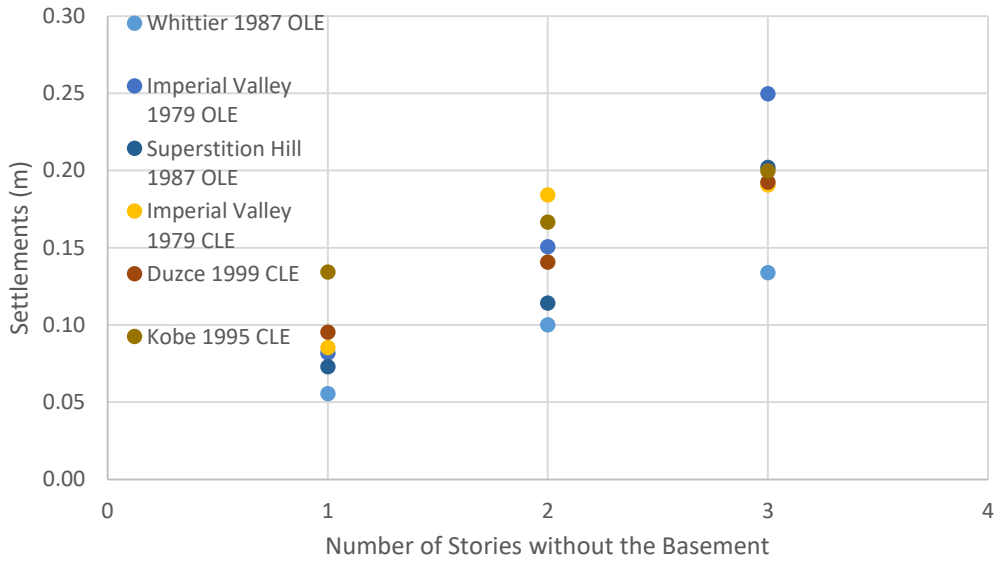

Fig. 80. Total settlements of different hypothetical structure types when subjected to the OLE and CLE conditions.

6. CONCLUSIONS AND RECOMMENDATIONS

6.1 Summary

The applicability of the UBC3D-PLM constitutive soil model to predict the onset of liquefaction and the post-liquefaction behavior at the Port of Long Beach (POLB), Pier S was presented. A characterization of the soils present at the site was completed with the information provided by the POLB. The subsurface investigation program mainly consisted of Standard Penetration Tests (SPTs) and Cone Penetration Tests (CPTs) up to a depth below the ground surface of about 38 m. Four layers of soil, labeled as "Units" in this research, were identified from the field tests as Units A, B, C, and D. The seismicity of the project site and in general for the southern California area was also summarized from a comprehensive report (Earth Mechanics Inc. 2006) provided by the POLB.

The liquefaction potential was assessed with different deterministic triggering semi-empirical methods to identify those soil layers susceptible to liquefaction. One of the main objectives of this research was to provide recommendations regarding the permanent ground deformations of soils that could compromise the normal operations of the port facility and compromise its resiliency needed after an earthquake event. To accomplish that research objective, in addition to simulate liquefaction-induced settlements with the UBC3D-PLM model, ground settlements were also computed with readily available semi-empirical methods for free-field conditions. These classical approaches consisted of an estimation of shear stresses and strains induced by the earthquake necessary to calculate post-liquefaction-induced volumetric strains, which after integrating over the entire depth, would provide estimates of the liquefaction-induced settlements of the site.

The soil parameters for the UBC3D-PLM constitutive soil model were determined with numerical analyses of boundary value problems that would reproduce other published liquefaction cyclic resistance curves such as the one proposed by Seed et al. (1985). This calibration was developed modeling undrained Direct Simple Shear (DSS) tests using the parameters obtained from published correlations based on corrected SPT blowcounts, $(N_1)_{60}$. The ability of the constitutive soil model

to capture monotonic isotropically consolidated undrained triaxial compression (CIU-TXC) test responses with the proposed parameters was also evaluated. Rayleigh damping coefficients were computed based on the natural frequencies of the soil deposit. A total of six different earthquake input motions taken from the Port Wide Ground Motion Study of POLB were used in the numerical simulations. The frequency content of each input motion was calculated using PLAXIS 2D and DEEPSOIL.

Pore water pressure ratios were calculated for the free-field conditions to identify potentially liquefiable soils. The onset of liquefaction was determined when pore water pressure ratios exceeded 85%. Thereafter, ground settlements were computed for the free-field conditions as excess pore water pressures were dissipated in the post-earthquake phase. From the free-field simulations using PLAXIS 2D and DEEPSOIL, Fast Fourier transforms of the outcropping signals were performed to conclude about the frequency content of the earthquake motions. Acceleration response spectra were computed for those signals at the top of the model with both programs and the results were compared with the acceleration response spectra presented in the Port Wide Ground Motion Study of POLB.

Parametric studies were performed on different hypothetical structures with one basement level to compute the settlements and liquefaction-induced damage mechanisms of these structures after an earthquake in light of other published research. To obtain post-shaking liquefaction-induced settlements, 1, 2 and 3-story buildings with a one basement level were evaluated under both earthquake levels. These analyses provided insight on the different soil and structural failure mechanisms when earthquakes like the ones considered in this research occur at the project site. These mechanisms were quantified with the development of pore water pressure ratios and with the calculation of relative shear stresses throughout the soil profile.

6.2 Conclusions

Based on the seismicity of the POLB, Pier S site, the following conclusions can be drawn:

- The POLB is located in a zone of very active faults indicating the potential for future seismic activity in the area. The Palos Verdes and Newport-Inglewood Structural Zone faults are the most important geological structures for the port and are capable to generate earthquake magnitudes varying from 6.8 to 7.4 and 6.3 to 7.0, respectively. Other active

faults slightly farther from the port can generate earthquake magnitudes up to 7.5, but with low recurrence periods.

- At least 189 earthquakes of magnitudes larger than 5 were registered in the last 200 years within a radius of 300 km around the POLB. This seismic hazard was grouped in two earthquake levels defined as the OLE and CLE with 72 and 475-year return periods, respectively. The POLB wide ground motion report recommends a peak ground acceleration (PGA) for geotechnical evaluations for the OLE of 0.21g with a dominant source corresponding to an earthquake magnitude of 6.5 at a distance of 20 km. The PGA for the CLE earthquake is 0.5g with an earthquake magnitude of 7.0 at a distance of 4 km.

Based on the definition of the subsurface conditions developed at the POLB, Piers S, the following conclusions can be drawn:

- The marine-estuarine sediments present in Unit B have a thickness of about 10.5 m. Tip resistances measured with CPT probes varied between 1 and 10 MPa and SPT N-values ranged from 1 to 12 blows/feet. These are typical variations of highly compressible cohesionless soils (Kulhawy and Mayne 1990). Relative densities averaged about 40% which is a typical value for loose sands. Natural water contents varied from 30 to 50% indicating that this is a normally consolidated soil deposit. Hence, these characteristics make this layer susceptible to liquefaction.
- From the information provided in the geotechnical investigation reports, it was found that Unit A is composed of man-made fills of silty to clayey sands with large variations of relative densities. Weak thin layers of fills are present within recent compacted fills. For this topmost soil layer, natural water contents varied from 10 to 30%, CPT tip resistances from 2 to 40 MPa, and SPT N-values from 4 to 50 blows/feet, indicating that this topmost man-made fill is composed of a great variety of soils. Unit C is a dense lower marine-estuarine deposit composed mostly of dense silty sands. Unit D is known as the Gaspur formation and is composed of very dense coarse sands with gravels. These last two layers are present below an elevation of -15 m MLLW and their natural water contents decrease with depth. These layers have average relative densities of 57 and 80%, respectively and are not susceptible to liquefaction as shown by large blowcounts and cone tip resistances measured in the field. The large overburden pressures of Units C and D and associated large confining stresses, ruled out the possibility of liquefaction of these units.

Based on the semi-empirical evaluation of liquefaction triggering and settlements of the POLB, Pier S, the following conclusions can be drawn:

- After the assessment of liquefaction susceptibility based on semi-empirical methods using SPTs, CPTs and V_s, it was found that Unit B is the only liquefiable layer under both earthquake levels (OLE and CLE). For Unit B, the factors of safety against liquefaction for the OLE and CLE conditions were computed as 0.89 and 0.28, respectively. These values represent a high likelihood of liquefaction to be induced in this soil layer if an earthquake of such magnitude strikes the area. Only the lower portion of Unit A and upper portion of Unit C are liquefiable under CLE conditions. SPTs, CPTs and V_s semi-empirical triggering methods are commonly used to predict only liquefaction onset of soils and are not intended to provide insight about post-liquefaction effects on soil or structures.
- Liquefaction-induced settlements using state-of-the-practice classical approaches were evaluated for free-field conditions. Using the results of SPTs, settlements of about 24 and 76 cm were computed for the OLE and CLE conditions, respectively. Using the CPTs, settlements of about 10 and 32 cm were computed for the OLE and CLE conditions, respectively. These computations evidence the potential settlements by both earthquake levels as a result of soil liquefaction. As expected, based on the PGA of each earthquake level, larger settlements were computed for the CLE than the OLE condition.
- The results obtained evidenced large discrepancies and scatter in the calculation of liquefaction-induced ground settlements using classical semi-empirical approaches. These methods can take into account the reduction of soil shear strength, but ignore the mechanisms that induce shear and volumetric strains. This complicated problem, even under free-field conditions, is still a subject of numerous efforts in the geotechnical community and requires more research to improve the predicting capabilities of simplified methods like those that can be readily used in current geotechnical earthquake engineering practice. Instead, probabilistic methods are advised.

Based on the calibration of constitutive soil parameters under monotonic and cyclic loading, the following conclusions can be drawn:

- The parameters for the UBC3D-PLM constitutive model were obtained using published correlations with SPTs. This practical way to determine constitutive soil parameters can be used in current geotechnical earthquake engineering practice. The constitutive parameters were calibrated for Unit B simulating undrained cyclic DSS tests to reach liquefaction at 15 uniform cycles. The most important parameters to determine the liquefaction onset and cyclic strength of soils were the densification (fac_{hard}) and post liquefaction factors (fac_{post}). A post-liquefaction factor of 0.02 and a densification factor of 0.45 were shown to reasonably match the overall trend of other published cyclic strength curves. Larger differences were computed for large values of SPTs. These simulations provided confidence that under undrained DSS conditions, the liquefaction onset can be studied with the UBC3D-PLM constitutive soil model.
- From the simulation of undrained DSS tests, it can be concluded that the results are more reliable for loose sands than for medium dense sands because larger pore water pressures are achieved for medium dense sands before the model reaches the yield surface. It was also observed from the results of undrained DSS stress paths that soil softens at the beginning of the cyclic loading and the cycles become narrower as the number of cycles increases. This behavior is attributed to the densification rule coded in the constitutive soil model which is typically activated in less than 5 cycles. This result was consistent for any cyclic stress ratio. The simulations also showed that the model adequately degrades the initial shear modulus which is reflected in a decreasing slope of the hysteretic loops. When the soil reaches liquefaction, the model does not allow further degradation and softening of the soil, and therefore cyclic mobility cannot be accurately simulated with the UBC3D-PLM model. Regardless of those limitations, it is concluded that the UBC3D-PLM model can be used to accurately determine the liquefaction onset of soils.
- Under monotonic loading, the results of numerical simulations reasonably matched laboratory test results, particularly for large confining pressures. Larger discrepancies were observed for low confining pressures. At the small strain levels (i.e., axial strains less than 1%), the model showed a stiff response in undrained conditions with respect to the experimental values.

Based on the numerical simulations developed with PLAXIS 2D for the POLB, Pier S, the following conclusions can be drawn:

- Six input time histories were selected according to the recommendations of the Port Wide Ground Motion study of the POLB (2006). Fast Fourier Transforms (FFT) were computed with PLAXIS 2D and DEEPSOIL using the acceleration time histories at the bottom of the numerical model. Predominant earthquake frequencies of about 3.8 Hz or less were computed and the results of both programs reasonably matched. FFTs calculated with PLAXIS 2D and DEEPSOIL for acceleration time-histories at the top of the model showed slight discrepancies between the six earthquakes analyzed in this research.
- The acceleration response spectra recommended by the Port Wide Ground Motion study POLB (2006) for the CLE condition is an envelope of the response spectra computed with the earthquake motions selected in this research. The acceleration response spectra obtained from both programs (DEEPSOIL and PLAXIS) are similar for the OLE and CLE earthquake conditions.
- The numerical simulations showed that Unit B for all earthquake motions developed pore water pressure ratios larger than 85%, which caused significant reductions of the vertical effective stresses. Relative shear stresses computed for Unit B indicated that the OLE conditions are capable to mobilize about 70% of the soil shear strength. The CLE earthquakes mobilized almost the entire soil shear strength of Unit B. Liquefaction mobilizes large amounts of shear strength and causes local failures in the soil mass. Low values of pore water pressure ratios were computed for Units A, C, and D. Thus, liquefaction was not reached in those layers.
- A limitation observed in the UBC3D-PLM is that under an undrained effective stress framework as coded in PLAXIS 2D, the soil is only capable to develop pore water pressures until the end of the shaking motion causing negligible vertical deformations (settlements) for free-field conditions. Also, resedimentation of soils in the post-shaking phases are not accurately captured with this constitutive model. In this research, a final phase of pore water pressure dissipation (consolidation) was included to provide an estimate of post-liquefaction deformations.
- Analyses of liquefaction-induced settlements for free-field conditions under OLE and CLE earthquake levels showed maximum settlements of 28 and 45 mm, respectively, after dissipation of excess pore water pressure generated during the cyclic loading. The results showed that complete dissipation of excess pore water pressures was reached in approximately 10 hours after the earthquake, which is a reasonable number for these soils with large hydraulic conductivities.

- Numerical simulations of 1, 2, and 3-story hypothetical structures founded on shallow footings on saturated granular soils suggested that most of the total liquefaction-induced settlements were caused during the earthquake motion with minor contribution arising from dissipation of the excess pore water pressure generated during the cyclic loading. These settlements were reached approximately 3 hours after the earthquake. Larger excess pore water pressures were generated under the structure than those developed for the free-field conditions. For Unit B, the numerical simulations showed large values of earthquake-induced shear stresses that fully mobilized the soil shear strength especially in the zones located below the hypothetical structures.
- As expected, these hypothetical structures increased the resulting vertical ground deformations, mobilized large values of soil shear strength, and increased the likelihood of liquefaction-induced damage proportionally to the number of stories. The results of these simulations showed that the earthquakes inducing the largest settlements were, for a 1-story structure the Kobe (CLE), for a 2-story structure the Imperial Valley (CLE) and for a 3-story structure the Imperial Valley (OLE) earthquakes. Values of about 13, 18 and 25 cm for 1, 2, and 3-story hypothetical buildings were reached, respectively. Conversely, the lowest settlements were obtained after the Whittier (OLE) earthquake with values of about 6, 10 and 13 cm for 1, 2 and 3-story structures, respectively.
- From the simulations of hypothetical structures located at the project location, it was found that settlements of structures with shallow foundations on liquefiable soils were controlled by a combination of failure mechanisms. Large shear strains were accumulated after ratcheting and bearing capacity failure was produced as result of soil softening as the earthquake occurs. Large settlements occurred during the first 20 seconds of each earthquake. Volumetric strains developed during the dissipation of excess pore water pressure stage have a minor contribution to the total computed settlements.

6.3 Recommendations

- Although the calibration performed in this research is valid for the soil conditions presented here, the parameters were not obtained and calibrated from advanced laboratory soil testing performed for the particular soil conditions of the POLB, Pier S. It is recommended in future projects on this site to perform advanced geotechnical laboratory testing (e.g., cyclic

triaxial with bender element measurements and cyclic direct simple shear tests) to improve the accuracy of the constitutive soil parameters proposed herein for the POLB, Pier S.

- The foundation system of any type of structure at the POLB, Pier S needs to be evaluated from a soil-structure interaction perspective. Shallow foundations can lead to large ground settlements and distortions unless a ground improvement program is implemented, like the ones the port is currently developing to mitigate liquefaction. Ground improvement of topmost 15 m would mitigate this problem. A technically feasible option is any type of deep foundation passing through the liquefiable soil reaching Unit C. However, any type of damage arising from lateral spreading is outside the scope of this report and needs to be analyzed.
- Site-specific response analyses during the design stages of any type of structure is recommended. The port developed a comprehensive database of acceleration time histories under two different earthquake level conditions, which can be readily used in the design stages of any structure type. These analyses can contribute to understand the soil-foundation-structure response to an earthquake event.
- Classical semi-empirical methods are currently used for the determination of the factor of safety against liquefaction and liquefaction-induced settlements. These methods, even though they are easy to implement, do not provide insight of the soil-structure interaction behavior of civil infrastructure under seismic loading. More advanced numerical models can provide more information of soil behavior like development of excess pore water pressures, soil stress strain behavior, *in situ* stress paths, and soil-foundation-structure interaction failure mechanisms that cannot be readily computed with simplified approaches. Regardless of the large computational effort required, the use of advanced numerical models like the ones presented in this research are advised, especially for sensitive geotechnical projects that involve loose soils subjected to dynamic loading. If predictions regarding liquefaction triggering, post-liquefaction behavior, and permanent deformations need to be issued, advanced methods are advised.
- The advantages of the UBC3D-PLM constitutive soil model to study soil liquefaction are that its model parameters can be reasonably estimated based on SPT values, $(N_1)_{60,}$ using readily available correlations. The model parameters can be calibrated with results of monotonic and cyclic laboratory soil testing. Further research is advised to find correlations between those constitutive parameters and the results of CPT soundings. This research concluded that this model is rather limited to predict the post-liquefaction behavior of soils

and that PLAXIS dynamic calculations under undrained effective stress parameters can be significantly improved with the use of fully-coupled effective stress models. It is suggested the application of more constitutive soil models like PM4SAND and Hypoplasticity to the site proposed in this research. The PM4SAND model incorporates calculation of post-shaking reconsolidation strains by reducing the post-shaking elastic shear and bulk moduli which increases the resulting strains and the geometric arrangement of the particles. Published research on PM4SAND states that resedimentation strains generated in the post-liquefaction stage are captured.

IMPLEMENTATION

It was developed in this research a site specific analysis of the liquefaction potential of soils at the Port of Long Beach (POLB), Pier S, which is located within a few miles of the Newport-Inglewood and the Palos Verdes faults. The soil parameters used herein can be used as the base for similar sites within the southern California area in which soil conditions are similar to the ones presented in this study. The soil parameters and use of the constitutive model can be used for other sites in which expansion was completed by placing hydraulic fills. The parameters, methodology, and models presented in this research (all of them available upon request) can serve as the base model for future analyses of liquefaction triggering and liquefaction-induced ground settlements.

At the end of this research, the use of advanced constitutive soil models like the UBC3D-PLM to predict the dynamic soil behavior is advised for projects in which further understanding of the liquefaction soil behavior are required. These advanced soil models, like the one used in this research, can be used to provide recommendations regarding to the permanent deformation of soils which could compromise the resiliency of civil infrastructure. The results and parameters presented herein can be used to determine the onset of liquefaction and estimate ground-induced settlements based on post-liquefaction excess pore pressure dissipation for different sites in southern California area when liquefiable soils are present in the subsurface conditions. Such implementation of the results presented herein and the proposed methodology if used in everyday geotechnical earthquake engineering practice, would improve the predicting capabilities in civil engineering, contribute to close the gap between research and practice, and provide further understanding of the mechanisms that trigger liquefaction in saturated loose sandy soil deposits subjected to rapid loading as the one induced by earthquakes.

Although our results are encouraging, further research and development is required to analyze other emerging soil models (like the PM4Sand model implemented in FLAC, just to cite one) that potentially can overcome the limitations found by the authors on some of the features presented in this research. This calibration of soil parameters is proposed to be tested in future projects in light of the results of advanced laboratory soil testing like cyclic triaxial or dynamic direct simple shear.

REFERENCES

Andrus, R. D., and Stokoe, K. H. I. (1997). "Liquefaction resistance based on shear wave velocity." *Proc., NCEER Workshop on Evaluation of Liquefaction Resistance of Soils*, N. C. for E. R. Engrg., ed., Nat. Ctr. for Earthquake Engrg. Res., State Univ. of New York at Buffalo, 89–128.

Andrus, R. D., and Stokoe II, K. H. (2000). "Liquefaction Resistance of Soils from Shear-Wave Velocity." *Journal of Geotechnical and Geoenvironmental Engineering*, 126(11), 1015–1025.

Arulmoli, K., Muraleetharan, K. K., Hossain, M. M., and Fruth, L. S. (1992). *VELACS: Verification of liquefaction analyses by centrifuge studies, Laboratory Testing Program. Soil Data Rep. Project No. 90-0562, The Earth Technology Corporation, Irvine, CA*, Irvine, CA.

Beaty, M. H., and Byrne, P. (1998). "An Effective Stress for Predicting Liquefaction Behaviour of Sand." *Geotechnical Earthquake Eng. and Soil Dynamics III, Geotechnical Sp. Pub.*, 1, 766–777.

Beaty, M. H., and Byrne, P. M. (2011). *UBCSAND Constitutive Model, Version 904aR*. *Itasca UDM Web Site*.

Beaty, M., and Perlea, V. (2012). "Effect on ground motion characteristics on Liquefying sand Dams." *GeoCongress*, (503), 2108–2117.

Bonilla, M. G. (1973). "Trench exposures across surface fault ruptures associated with the San Fernando earthquake." *San Fernando, California, earthquake of February 9, 1971, Vol. 3: Geological and Geophysical Studies - Murphy L.M., ed., Washington, D.C., National Oceanic and Atmospheric Administration*, 173–182.

Boulanger, R., and Idriss, I. (2004). *Evaluating the potential for liquefaction or cyclic failure of silts and clays. Center for Geotechnical Modeling*, UC Davis, Davis, CA.

Boulanger, R. W., and Idriss, I. M. (2012). "Probabilistic Standard Penetration Test – Based Liquefaction – Triggering Procedure." *J. Geotech. Geoenviron. Eng.*, 138(10), 1185–1195.

Boulanger, R. W., and Idriss, I. M. (2014). *CPT and SPT Based Liquefaction Triggering Procedures*. *Center for Geotechnical Modeling*, UC Davis, Davis, CA.

Boulanger, R. W., and Ziotopoulou, K. (2015). *PM4SAND (Version 3): A Sand Plasticity Model for Earthquake Engineering Applications*.

Bray, J. D., Rourke, T. D. O., Cubrinovski, M., Zupan, J. D., Taylor, M., Toprak, S., Hughes, M., and Ballegooy, S. Van. (2013). *Liquefaction Impact on Critical Infrastructure in Christchurch*.

Bryant, W. A. (1985). *California Division of Mines and Geology Fault Evaluation Report FER-173 Northern Newport-Inglewood Fault Zone, Los Angeles County, California*.

Byrne, P. M., Park, S. S., Beaty, M. H., Sharp, M., Gonzalez, L., and Abdoun, T. (2004). "Numerical modeling of liquefaction and comparison with centrifuge tests." *Can. Geotech. J.*, 41(2), 193–211.

California Department of Conservation. (1999). *Seismic Hazard Zones Map - Long Beach Quadrangle*. Long Beach, California.

California Geological Survey. (2003). "The revised 2002 California probabilistic seismic hazard maps." *California Geological Survey website by Cao, T., Bryant, W.A., Rowshandel, B., Branum, D., and Wills, C.J.*

Casagrande, A. (1936). "Characteristic of cohesionless soils affecting the stability of slopes and earth fills." *Journal of the Boston Society of Civil Engineers*, 1, 257–276.

Castro, G., Keller, T. O., and Boynton, S. S. (1989). "Re-evaluation of the lower San Fernando Dam." *Contract Report GL-89-2 Volume 1, US Army Corps of Engineers*.

Cetin, K. O., Seed, R. B., Der Kiureghian, A., Tokimatsu, K., Harder, L. F., Kayen, R. E., and Moss, R. E. S. (2004). "Standard Penetration Test-Based Probabilistic and Deterministic Assessment of Seismic Soil Liquefaction Potential." *J. Geotech. Geoenviron. Eng.*, 130(12), 1314–1340.

Chang, M., Kuo, C. ping, Shau, S. hui, and Hsu, R. eeh. (2011). "Comparison of SPT-N-based analysis methods in evaluation of liquefaction potential during the 1999 Chi-

chi earthquake in Taiwan." *Computers and Geotechnics*, Elsevier Ltd, 38(3), 393–406.

Clarke, S. H., Greene, H. G., Kennedy, M. P., and Vedder, J. G. (1987). "Geological map of the inner-southern continental margin, California Continental Margin Geologic Map series: California." *California Division of Mines and Geology*.

Dashti, S. (2009). "Toward Developing an Engineering Procedure for Evaluating Building Performance on Softened Ground." U. of California, Berkeley.

Dashti, S., and Bray, J. D. (2012). "Numerical Insights Into Liquefaction-Induced Building Settlement." *Earthquake*, 1660–1669.

Dashti, S., and Bray, J. D. (2013). "Numerical Simulation of Building Response on Liquefiable Sand." *Journal of Geotechnical and Geoenvironmental Engineering*, 139(8), 1235–1249.

Dashti, S., Bray, J., Pestana, J., Riemer, M., and Wilson, D. (2010a). "Mechanisms of Seismically Induced Settlement of Buildings with Shallow Foundations on Liquefiable Soil." *Journal of Geotechnical and Geoenvironmental Engineering*, JOUR, American Society of Civil Engineers, 136(1), 151–164.

Dashti, S., Bray, J., Pestana, J., Riemer, M., and Wilson, D. (2010b). "Centrifuge Testing to Evaluate and Mitigate Liquefaction-Induced Building Settlement Mechanisms." *Journal of Geotechnical and Geoenvironmental Engineering*, JOUR, American Society of Civil Engineers, 136(7), 918–929.

Dibblee, T. W. J. (1999). "Geologic Map of the Palos Verdes Peninsula and Vicinity, Redondo Beach, Torrance and San Pedro quadrangles." *Dibblee Geological Foundation Map DF 70*.

Dolan, J. F., Sieh, K., Rockwell, T. K., Yeats, R. S., Shaw, J., Suppe, J., Huftile, G. J., and Gath, E. M. (1995). "Prospect for larger or more frequent earthquakes in the Los Angeles metropolitan region, California." *Science*, 267, 1595–1616.

Earth Mechanics Inc. (1993). "Probabilistic seismic-hazard assessment and free-field site Response, Port of Los Angeles, Pier 400." *Report for Pier 400 Design Consultants, Carson, CA, EMI project No. 92-204*.

Earth Mechanics Inc. (1995). "Interim design response spectrum, Vincent Thomas bridge

retrofit." *Report for Moffatt & Nichol and Caltrans Translab, EMI project No. 95-126, August 14.*

Earth Mechanics Inc. (2001). "Final ground motion and fault study report, West Basin, Port of Los Angeles, San Pedro, California." *Report for Port of Los Angeles, San Pedro, CA, EMI project No. 00-115-8, April 27.*

Earth Mechanics Inc. (2006). "Port-Wide Ground Motion Study Port of Long Beach , California." *EMI Project No. 01-143*, (1).

Edwards, B. D., Catchings, R. D., Hildebrand, T. G., Miller, M. S., Ponti, D. J., and Wolfe, S. C. (2001). "Quaternary sedimentary structure of the southwestern Los Angeles basin region." *Geological Society of America Abstracts with Program*, 33, A-41.

Edwards, B. D., Ehmann, K. D., Ponti, D. J., Tinsley, J. C. I., and Reicherdt, E. G. (2003). "Offshore stratigraphic controls on saltwater intrusion in Los Angeles area coastal aquifers." *LA Basin 2003, Original Urban Oil Field Legends, Conference Program and Abstracts - American Association of Petroleum Geologists, Pacific Section and Western Region Society of Petroleum Engineers, Abstract*, 62.

Edwards, B. D., Ponti, D. J., Ehmann, K. D., Tinsley, J. C. I., and Reicherdt, E. G. (2002). "Offshore stratigraphic controls on saltwater intrusion in Los Angeles area coastal aquifers." *American Geophysical Union Fall Meeting, San Francisco, CA, EOS*, 83, F567.

Finn, W. D., Ledbetter, R. H., and Marcuson, W. F. (1995). "Modern practice in the seismic response analysis of embankment Dams." *Scientia Iranica*, 2(2), 145–164.

Fischer, M. A., Normark, W. R., Langenheim, V. E., and Calvert, A. J. (2004). "The offshore Palos Verdes Fault zone near San Pedro, Southern California." *Bulletin of the Seismological Society of America*, 94, 506–530.

Fischer, M. A., Rudat, J. H., Patterson, R. H., and Simila, G. (1987). "The Palos Verdes fault zone: onshore and offshore." *Geology of the Palos Verdes Peninsula and San Pedro Bay, Society of Economic Paleontologists and Mineralogists, Pacific Coast Section, Guidebook*, 91–133.

Freeman, S. T., Heath, E. G., and Guptill, P. D. (1992). "Seismic hazard assessment,

Newport-Inglewood Fault Zone." *Engineering geology practice in Southern California, Association of Engineering Geologists, Southern California Section, Special Publication 4*, 4, 211–231.

Galavi, V., Petalas, A., and Brinkgreve, R. B. J. (2013). "Finite element modelling of seismic liquefaction in soils." *Geotechnical Engineering*, 44(3), 55–64.

Geotechnical Professionals Inc. (2003). *Geotechnical Studies for Pier S Wharf Port of Long Beach*. Long Beach, California.

Grant, L. B., Waggoner, J. T., Rockwell, T. K., and Von Stein, C. (1997). "Paleoseismicity of the north branch of the Newport-Inglewood fault zone in Huntington Beach, California, from cone penetrometer test data." *Bulletin of the Seismological Society of America*, 87, 277–293.

Gu, Q. (2008). "Finite Element Response Sensitivity and Reliability Analysis of Soil-Foundation-Structure-Interaction (SFSI) Systems." University of California , San Diego.

Hardin, B. O. (1978). "The nature of stress-strain behaviour of soils, Earthquake Engineering and Soil Dynamics." *Proceedings of the ASCE Geotechnical Engineering Division Specialty Conference, June 19-21, 1978*, 1, 3–90.

Hauksson, E. (1987). "Seismotectonics of the Newport-Inglewood fault zone in the Los Angeles Basin, southern California." *Bulletin of the Seismological Society of America*, 77, 539–561.

Hauksson, E. (1990). "Earthquakes, faulting, and stress in the Los Angeles basin." *Journal of Geophysical Research*, 95, 15365–15394.

Hausler, E. A. (2002). "Influence of ground improvement on settlement and liquefaction: A study based on field case history evidence and dynamic geotechnical centrifuge tests." University of California, Berkeley.

Hudson, M., Idriss, I. M., and Beirkae, M. (1994). "QUAD4M User's Manual."

Idriss, I. (1990). "Response of Soft Soil Sites during Earthquakes." *Proc. H. Bolton Seed Memorial Symposium*, 273–289.

Idriss, I. (1991). "Earthquake ground motions at soft soil sites." *Second International Conference on Recent Advance in Geotechnical Earthquake Engineering and Soil*

Dynamics, St. Louis, Missouri.

Idriss, I. M., and Boulanger, R. W. (2003). "Estimating Ka for Use in Evaluating Cyclic Resistance of Sloping Ground." *Proceedings from the Fourth Japan - U.S Workshop on Earthquake Resistant Design of Lifeline Facilities and Countermeasures for Soil Liquefaction*, 449.

Idriss, I. M., and Boulanger, R. W. (2008). "Soil Liquefaction During Earthquakes." *Earthquake Engineering Research Institute*, 136(6), 755.

Idriss, I. M., and Boulanger, R. W. (2010). *SPT-Based Liquefaction Triggering Procedures*.

Ishihara, K., and Yoshimine, M. (1992). "Evaluation of Settlements in Sand Deposits Following Liquefaction During Earthquakes." *Soils and Foundations*, 32(1), 173–188.

Jaky, J. (1944). "The coefficient of earth pressure at rest. In Hungarian (A nyugalmi nyomas tenyezoje)." *J. Soc. Hung. Eng. Arch. (Magyar Mernok es Epitesz-Egylet Kozlonye)*, 355–358.

Jefferies, M., and Been, K. (2016). *Soil liquefaction: A critical state approach*. *Taylor & Francis*.

Kayen, R. E., Mitchell, J. K., Seed, R. B., Lodge, A., Nishio, S., and Coutinho, R. (1992). "Evaluation of SPT-, CPT-, and shear wave-based methods for liquefaction potential assessment using Loma Prieta data." *Proc., 4th Japan-U.S. Workshop on Earthquake-Resistant Des. of Lifeline Fac. and Countermeasures for Soil Liquefaction*, 177–204.

Kramer, S. (1996). *Geotechnical Earthquake Engineering*. Prentice-Hall, NJ.

Kramer, S., and Elgamal, A. (2001). *Modeling soil liquefaction hazards for performance based earthquake engineering. Report 2001/13, Pacific Earthquake Engineering Research Center. University of California, Berkeley*.

Kuhlemeyer, R. ., and Lysmer, J. (1973). "Finite element method accuracy for wave propagation problems." *Journal of soil mechanics and foundation*, 99(5), 421–427.

Kulhawy, F. H., and Mayne, P. W. (1990). "Manual on Estimating Soil Properties for Foundation Design." *Ostigov*.

Lee, K. L., and Albaisa, A. (1974). “Earthquake-induced settlements in saturated sands.” *J. Soil Mech. Found. Div., ASCE*, 100(4), 387–400.

Liao, S. S. C., and Whitmanm, R. V. (1986). “Overburden correction factors for SPT in sand.” *J. Geotech. Engrg., ASCE*, 3(112), 373–377.

Liu, L., and Dobry, R. (1997). “Seismic Response of Shallow Foundation on Liquefiable Sand.” *Journal of Geotechnical and Geoenvironmental Engineering*, 123(6), 557–567.

Lopez-Caballero, F., and Modaressi Farahmand-Razavi, A. (2008). “Numerical simulation of liquefaction effects on seismic SSI.” *Soil Dyn. Earthquake Eng.*, 28(2), 85–98.

Los Angeles County Seismic Safety Element. (1990). “Technical appendix to the safety element of the Los Angeles County general plan, hazard reduction in Los Angeles County.” *Prepared for Department of Regional Planning by Leighton and Associates and Sedway Cooke Associates.*

Lu, J., Elgamal, A., Yan, L., Law, K. H., and Conte, J. P. (2011). “Large-Scale Numerical Modeling in Geotechnical Earthquake Engineering.” *International Journal of Geomechanics*, 11(6), 490–503.

Madabhushi, G., Knappett, J., and Haigh, S. (2010). “Design of Pile Foundations in Liquefiable Soils.” *Imperial College Press*, 33.

Makra, A. (2013). “Evaluation of the UBC3D-PLM Constitutive Model for Prediction of Earthquake Induced Liquefaction on Embankment Dams.” Delft University of Technology.

Marcuson W.F., I. I. I., Hynes, M. E., and Franklin, A. G. (2007). “Seismic Design and Analysis of Embankment Dams: The State of Practice.” *The Donald M. Burmister Lecture, Department of Civil engineering Mechanics, Columbia University*, (NOVEMBER 2007).

Martin, G. R., Tsai, C.-F., and Arulmoli, K. (1991). “A Practical Assessment of Liquefaction Effects and Remediation Needs.” *Proceedings, 2nd International Conference on Recent Advances in Geotechnical Earthquake Engineering and Soil Dynamics*, St. Louis, Missouri, 11–15.

McNeilan, T. W., Rockwell, T. K., and Resnick, G. S. (1996). “Style and rate of Holocene slip, Palos Verdes fault, Southern California.” *Journal of Geophysical Research,* 101, 8317–8334.

Meyerhof, G. G. (1957). “Discussion on Research on determining the density of sands by penetration testing.” *Proc. 4th International Conference on Soil Mechanics and Foundation Engineering,* 1, 110.

Moriwaki, Y., Beikae, M., and Idriss, I. M. (1988). “Nonlinear Seismic Analysis of the Upper San Fernando Dam Under the 1971 San Fernando Earthquake.” *Proceedings, 9th World Conference on Earthquake Engineering, Tokyo and Kyoto, Japan*, VIII, 237–241.

Muraleetharan, K. K., Mish, K. D., Yogachandran, C., and Arulanandan, K. (1988). “DYSAC2: Dynamic Soil Analysis Code for 2- dimensional Problems, Computer Code.” Department of Civil Engineering, University of California, Davis, CA.

Muraleetharan, K. K., Mish, K. D., Yogachandran, C., and Arulanandan, K. (1991). *User’s Manual for DYSAC2: Dynamic Analysis Code for 2-Dimensional Problems*. Davis, CA.

Naeim, F. (2001). *The Seismic Design Handbook.* (Springer, ed.).

Nardin, T. R., and Henyey, T. L. (1978). “Pliocene-Pleistocene diastrophism of Santa Monica and San Pedro shelves, California continental borderland.” *American Association of Petroleum Geologists Bulletin*, 62, 247–272.

NCEER. (1997). *Proceedings of the NCEER Workshop on Evaluation of Liquefaction Resistance of Soil - Salt Lake City, Utah: Technical Report NCEER-97-002*.

Negussey, D. (1984). “An Experimental Study of the Small Strain Response of Sand.” *Statewide Agricultural Land Use Baseline 2015,* The University of British Columbia.

Olson, S. M., and Starkm, T. D. (2001). “Liquefaction analysis of Duncan Dam using strength ratios.” *Canadian Geotechnical Journal*, 43(5), 484–499.

Oskin, M., Sieh, K., Rockwell, T., Miller, G., Guiptill, P., M., C., McArdle, S., and Elliot, P. (2000). “Active parasitic folds on the Elysian Park anticline: implications for seismic hazard in central Los Angeles, California.” *Geological Society of America*

Bulletin, 113, 693–707.

Petalas, A., and Galavi, V. (2013). *Plaxis Liquefaction Model UBC3D-PLM*.

Plaxis. (2015). "Site response analysis and liquefaction evaluation."

Ponti, D. J. (2004). "Principal Investigator for Coastal Groundwater Investigation, personal communication." *U.S. Geolgical Survey*.

Prevost, J. H. (1981). "DYNAFLOW: A Nonlinear Transient Finite Element Analysis Program." Princeton University, Department of Civil Engineering, Princeton, NJ.

Puebla, H., Byrne, P. M., and Phillips, R. (1997). "Analysis of CANLEX liquefaction embankments: prototype and centrifuge models." *Can. Geotech J.*, 34(5), 641–657.

Robertson, P. K. (2015). *Guide to Cone Penetration Testing*.

Robertson, P. K., Woeller, D. J., and Finn, W. D. (1992). "Seismic cone penetration test for evaluating liquefaction potential under cyclic loading." *Can. Geotech. J., Ottawa*, 29, 686–695.

Robertson, P. K., and Wride, C. (Fear). (1998). "Evaluating cyclic liquefaction potential using the cone penetration test." *C. Geotech. J.*, 35(3), 442–459.

ROSRINE. (2001). "Resolution of site response from the Northridge Earthquake." <http://geoinfo.usc.edu/rosrine/>.

Rubin, C. M., Lindvall, S. C., and Rockwell, T. K. (1998). "Evidence for large earthquakes in metropolitan Los Angeles." *Science*, 281, 398–402.

Schanz, T., Vermeer, A., and Bonnier, P. (1999). "The hardening soil model: formulation and verification." *Beyond 2000 Comput. Geotech. 10 years PLAXIS Int. Proc. Int. Symp. beyond 2000 Comput. Geotech. Amsterdam Netherlands 1820 March 1999*, 281.

Schell, B. A. (1991). "Seismotectonic zonation and seismic hazard analyses in Southern California." *Fourth International Conference on Seismic Zonation, Proceedings*, 2, 19–26.

Seed, H. B. (1983). "Earthquake-resistant design of earth dams." *Proc., Symp. Seismic Des. of Earth Dams and Caverns, ASCE, New York*, ASCE, New York, 41–64.

Seed, H. B., and Idriss, I. M. (1971). "Simplified procedure for evaluating soil liquefaction potential." *J. of the Soil Mechanics and Foundation*, 107(SM9), 1249–

1274.

Seed, H. B., and Idriss, I. M. (1982). *Ground motions and soil liquefaction during earthquakes*. *Earthquake Engineering Research Institute Monograph, Ocacland, California*.

Seed, H. B., Lee, K. L., and Idriss, I. M. (1973). "Analysis of the slides in the San Fernando Dams during the earthquake of Feb. 9, 1971." *Earthquake Engineering Research Center*, 73(2).

Seed, H. B., Leps, T. M., Duncan, J. M., and Bieber, R. E. (1976). "Hydraulic fracturing and its possible role in the Teton Dam failure." *Hydraulic fracturing and its possible role in the Teton Dam failure of Teton Dam. Denver: U. S. Bureau of Reclamation*.

Seed, H. B., Seed, R. B., Harder, L. F., and Jong, H. L. (1988). "Re-evaluation of the slide in the lower San Fernando dam in the earthquake of February 9, 1971." *Report UCB/EERC-88/04, Earthquake Engineering Research Centre, University of California at Berkeley, Berkeley, CA*.

Seed, H. B., Tokimatsu, K., Harder, L. F., Chung, M., and Riley, M. (1985). "Influence of SPT Procedures in Soil Liquefaction Resistance Evaluations." *J. Geotech. Engrg., ASCE*, I(12), 1425–1445.

Seed, R. B., Dickenson, S. E., Rau, G. A., White, R. K., and Mok, C. M. (1994). "Site effects on strong shaking and seismic risk: Recent developments and their impact on seismic design codes and practice." *Proc., Struct. Congr. II. ASCE*, ASCE, 573–578.

Shaw, J. H., and Shearer, P. M. (1999). "An elusive blind-thrust fault beneath metropolitan Los Angeles." *Science*, 283, 1516.

Shaw, J. H., and Suppe, J. (1996). "Earthquake hazards of active blind thrust faults under the central Los Angeles basin, California." *Journal of Geophysical Research*, 101, 8623–8642.

Shlemon, R. J., Elliott, P., and Franzen, S. (1995). "Holocene displacement history of the Newport-Inglewood, North Branch fault splays, Santa Ana River floodplain, Huntington Beach, California." *Geological Society of America, Abstracts with Programs*, 27, A-375.

Sykora, D. W. (1987). *Creation of a data base of seismic shear wave velocities for*

correlation analysis. Geotech. Lab. Misc. Paper GL-87- 26.

Tasiopoulou, P., Gerolymos, N., and Gazetas, G. (2015). "Class a Prediction for Seismic Centrifuge Modeling of Multi-Block Quay-Wall : Undrained (Plaxis) Versus Coupled (Flac) Effective Stress Analysis." (June).

Tokimatsu, K., and Seed, B. (1986). "Evaluation of Settlements in Sands due to Earthquale Shaking." *J. Geotech. Engrg., ASCE,* 113(8), 861–878.

Truex, J. N. (1974). "Structural evolution of Wilmington, California anticline." *American Association of Petroleum Geologists Bulletin*, 58, 2398–2410.

Tsegaye, A. B. (2010). *Liquefaction Model (UBC3D)*.

Vasquez-Herrera, A., and Dobry, R. (1988). "The Behavior of Undrained Contractive Sand and Its Effect on Seismic Liquefaction Flow Failures of Earth Structures." *Troy, NY: Rensselaer Polytechnic Institute*.

Vedder, J. G., Greene, H. G., Clarke, S. H., and Kennedy, M. P. (1986). "Geologic map of the mid- Southern California continental margin." *California Division of Mines and Geology, California Continental Margin Geologic Map Series, Map No. 2A*.

Wang, W. (1979). *Some findings in soil liquefaction*. Beijing, China.

Ward, S. N., and Valensise, G. (1994). "The Palos Verdes terraces, California: bathtub rings from a buried reverse fault." *Journal of Geophysical Research*, 99, 4485–4494.

Wells, D., and Coppersmith, K. (1994). "Updated empirical relationships among magnitude, rupture length, rupture area, and surface displacement." *Bull Seism. Soc. Am.,* 84, 974–1002.

Winde, H. P. (2015). "Finite Element Modelling for Earthquake Loads on Dykes." Delft Univrsity of Technology.

Woodring, W. P., Bramlette, M. N., and Kew, W. S. W. (1946). "Geology and Paleontology of Palos Verdes Hills, California." *U.S. Geological Survey, Professional Paper,* 207.

Wright, T. L. (1991). "Structural geology and tectonic evolution of the Los Angeles Basin, California." *Active basin margins - Biddle, K.T., ed., American Association of Petroleum Geologists Memoir 52*.

Yoshimi, Y., Kuwabara, F., and Tokimatsu, K. (1975). "One-dimensional volume change

characteristics of sands under very low confining stresses." *Soil and Foundations*, 15(3), 51–60.

Yoshimi, Y., and Tokimatsu, K. (1977). "Settlement of Buildings on Saturated sand during earthquakes." *In Proceedings from the ninth world conference on earthquake engineering, Tokyo-Kyoto, Japan*, 17(1), 95–100.

Youd et al. (2001). "Liquefaction Resistance of Soils: Summary Report from the 1996 NCEER and 1998 NCEER/NSF Workshops on Evaluation." *J. Geotech. Geoenviron. Eng.*, 127(10), 817–833.

Zeibauer, E. J., Kues, H. A., Burnham, W. L., and Keene, A. G. (1962). "Dominguez Gap Barrier Project Geologic Investigation." *Los Angeles County Flood Control District, March 1962*.